3D optical metrology by digital moiré:
Pixel-wise calibration refinement, grid removal,
and temporal phase unwrapping

by

Fatemeh Mohammadi

A thesis
presented to the University of Waterloo
in fulfilment of the
thesis requirement for the degree of
Doctor of Philosophy
in
Systems Design Engineering

Waterloo, Ontario, Canada, 2017
© Fatemeh Mohammadi 2017

Examining Committee Membership

The following served on the Examining Committee for this thesis. The decision of the Examining Committee is by majority vote.

External Examiner   Song Zhang
Associate Professor

Supervisor   Jonathan Kofman
Associate Professor

Internal Member   Hamid Tizhoosh
Professor

Internal Member   Eihab Abdel-Rahman
Associate Professor

Internal-external Member   Zhou Wang
Professor

Author's Declaration

This thesis consists of material all of which I authored or co-authored: see Statement of Contributions included in the thesis. This is a true copy of the thesis, including any required final revisions, as accepted by my examiners. I understand that my thesis may be made electronically available to the public.

Statement of Contributions

Based on detailed literature review by Fatemeh Mohammadi, and through discussions of existing 3D optical metrology techniques, research directions, and experimental techniques with supervisor Dr. Jonathan Kofman, Fatemeh Mohammadi determined the specific research directions and developed the new techniques with contribution and guidance of Dr. Jonathan Kofman. Fatemeh Mohammadi carried out all experiments and data analysis. Dr. Jonathan Kofman edited published work derived from this research as well as this thesis following first drafts written by Fatemeh Mohammadi.

Abstract

Fast, accurate three dimensional (3D) optical metrology has diverse applications in object and environment modelling. Structured-lighting techniques allow non-contacting 3D surface-shape measurement by projecting patterns of light onto an object surface, capturing images of the deformed patterns, and computing the 3D surface geometry from the captured 2D images. However, motion artifacts can still be a problem with high-speed surface-motion especially with increasing demand for higher measurement resolution and accuracy.

To avoid motion artifacts, fast 2D image acquisition of projected patterns is required. Fast multi-pattern projection and minimization of the number of projected patterns are two approaches for dynamic object measurement. To achieve a higher rate of switching frames, fast multi-pattern projection techniques require costly projector hardware modification or new designs of projection systems to increase the projection rate beyond the capabilities of off-the-shelf projectors. Even if these disadvantages were acceptable (higher cost, complex hardware), and even if the rate of acquisition achievable with current systems were fast enough to avoid errors, minimization of the number of captured frames required will still contribute to reduce further the effect of object motion on measurement accuracy and to enable capture of higher object dynamics. Development of an optical 3D metrology method that minimizes the number of projected patterns while maintaining accurate 3D surface-shape measurement of objects with continuous and discontinuous surface geometry has remained a challenge.

Capture of a single image-frame instead of multiple frames would be advantageous for measuring moving or deforming objects. Since accurate measurement generally requires multiple phase-shifted images, imbedding multiple patterns into a single projected composite pattern is one approach to achieve accurate single-frame 3D surface-shape measurement. The main limitations of existing single-frame methods based on composite patterns are poor resolution, small range of gray-level intensity due to collection of multiple patterns in one image, and degradation of the extracted patterns because of modulation and demodulation processes on the captured composite pattern image.

To benefit from the advantages of multi-pattern projection of phase-shifted fringes and single-frame techniques, without combining phase-shifted patterns into one frame, digital moiré was used. Moiré patterns are generated by projecting a grid pattern onto the object, capturing a single frame, and in a post-process, superimposing a synthetic grid of the same frequency as in

the captured image. Phase-shifting is carried out as a post-process by digitally shifting the synthetic grid across the captured image. The useful moiré patterns, which contain object shape information, are contaminated with a high-frequency grid lines that must be removed. After performing grid removal, computation of a phase map, and phase-to-height mapping, 3D object shape can be computed. The advantage of digital moiré provides an opportunity to decrease the number of projected patterns. However, in previous attempts to apply digital phase-shifting moiré to perform 3D surface-shape measurement, there have been significant limitations.

To address the limitation of previous system-calibration techniques based on direct measurement of optical-setup parameters, a moiré-wavelength based phase-to-height mapping system-calibration method was developed. The moiré-wavelength refinement performs pixel-wise computation of the moiré wavelength based on the measured height (depth). In measurement of a flat plate at different depths, the range of root-mean-square (RMS) error was reduced from 0.334 to 0.828 mm using a single global wavelength across all pixels, to 0.204 to 0.261 mm using the new pixel-wise moiré-wavelength refinement.

To address the limitations of previous grid removal techniques (precise mechanical grid translation, multiple-frame capture, moiré-pattern blurring, and measurement artifacts), a new grid removal technique was developed for single-frame digital moiré using combined stationary wavelet and Fourier transforms (SWT-FFT). This approach removes high frequency grid both straight and curved lines, without moiré-pattern artifacts, blurring, and degradation, and was an improvement compared to previous techniques.

To address the limitations of the high number of projected patterns and captured images of temporal phase unwrapping (TPU) in fringe projection, and the low signal-to-noise ratio of the extended phase map of TPU in digital moiré, improved methods using two-image and three-image TPU in digital phase-shifting moiré were developed. For measurement of a pair of hemispherical objects with true radii 50.80 mm by two-image TPU digital moiré, least-squares fitted spheres to the measured 3D point clouds had errors of 0.03 mm and 0.06 mm, respectively (sphere fitting standard deviations 0.15 mm and 0.14 mm), and the centre-to-centre distance measurement between hemispheres had an error of 0.19 mm. The number of captured images required by this new method is one third that for three-wavelength heterodyne temporal phase unwrapping by fringe projection techniques, which would be advantageous in measuring dynamic objects, either moving or deforming.

Acknowledgements

Dedication

I dedicate this thesis to my parents for their constant affection and love throughout my whole life.

Table of Contents

List of Figures

List of Tables

Chapter 1

Introduction

1.1 Demand for fast three-dimensional surface-shape measurement

Fast, accurate, and non-contact three dimensional (3D) surface-shape measurement has diverse applications in object and environment modelling [1-4], such as, human body modeling for entertainment [2, 5-7] and medical diagnosis [8-10], and 3D object recognition [11]. The 3D-shape measurement of moving objects, for example, in online part inspection [2, 3], and measurement of dynamically deforming objects, such as player facial expressions in the gaming industry, and the lungs or heart in medical diagnosis [4, 9, 10], all require fast measurement techniques. Optical techniques have advanced greatly to achieve rapid and accurate non-contact 3D surface-shape measurement [2, 4]. However, motion artifacts [12, 13] are still a problem with high-speed surface-motion especially with increasing demand for higher measurement resolution and accuracy.

Structured-light techniques are among the most common types of optical 3D measurement technology [14]. Fringe projection profilometry (FPP) [15-17] and moiré profilometry (MP) [18-20] are among the common structured-light techniques. The following sections briefly review FPP and MP techniques toward defining the research problem and objectives.

1.1.1 Fringe projection techniques

In fringe projection techniques, a fringe pattern is projected onto an object surface, and a camera positioned at an angle to the projector captures an image of the fringe patterns that appear distorted on the object surface (Fig. 1.1) [16]. In phase-shifting fringe projection techniques [21-23], multiple phase-shifted patterns are sequentially projected onto the object. The object height is modulated in the phase information [24], which can be extracted by analyzing the captured images of at least three phase-shifted patterns on the object surface (explained further in Section 1.2).
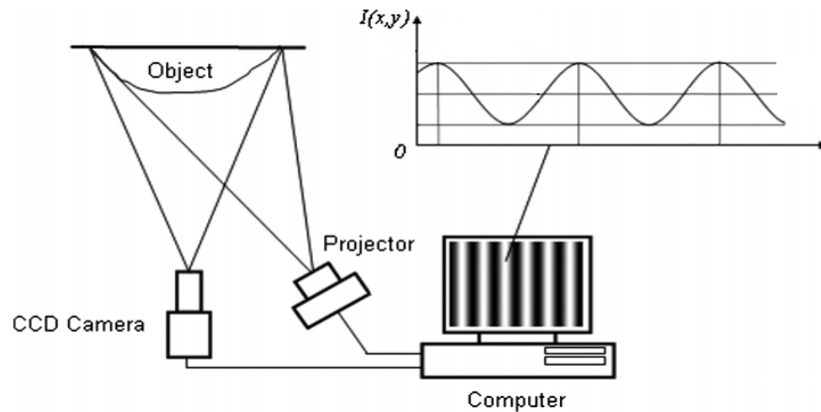
Figure 1.1. Optical system configuration in fringe projection technique. (Adapted from [16]).

1.1.2 Moiré profilometry techniques

A moiré effect can be generated by placing two periodic patterns over each other (Fig. 1.2a). Moiré profilometry generates equal-depth moiré contours to determine object height distribution (Fig. 1.2b) [25].

(a)   (b)
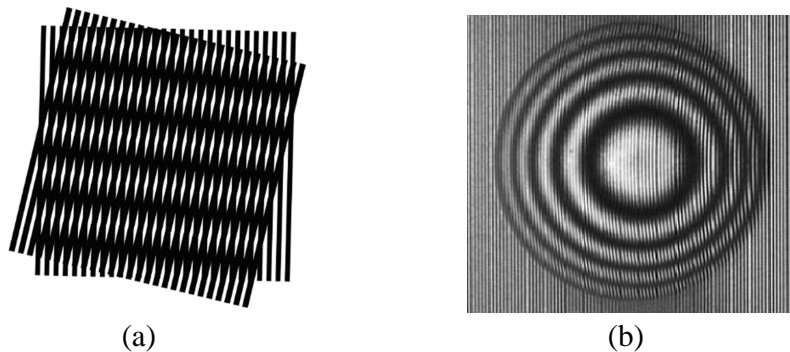
Figure 1.2. (a) Moiré pattern generated with two linear gratings (b) Moiré contour on a hemisphere.

Moiré-based surface measurement is performed by first projecting light through a grating onto an object surface. In shadow moiré [26,27] an image of the deformed light pattern on the surface, is captured by viewing through the same grating at an angle to the projection (Fig. 1.3a), while in projection moiré [28,29], the image of the deformed pattern is captured by viewing through a second grating at an angle to the projection (Fig. 1.3b). Shadow and projection moiré both require complicated optical setup, such as physical gratings and optical lens. Digital moiré [18], detailed in Chapter 2, is another type of moiré topography that is easy to implement without complicated optical equipment. Flexibility in adjusting the virtual grid pitch, the ability to generate arbitrary phase shifts, and the ability to perform phase-shifting as a post-process to

2

image capture, make the digital moiré technique potentially more useful than conventional moiré. In comparison to fringe projection, in moiré profilometry, the useful moiré patterns, which contain object shape information, are always contaminated with a high-frequency grid-pattern (Fig. 1.2). This grid pattern is considered as noise and must be removed in order to perform further analysis on the moiré patterns to extract object shape information [30].

(a)   (b)
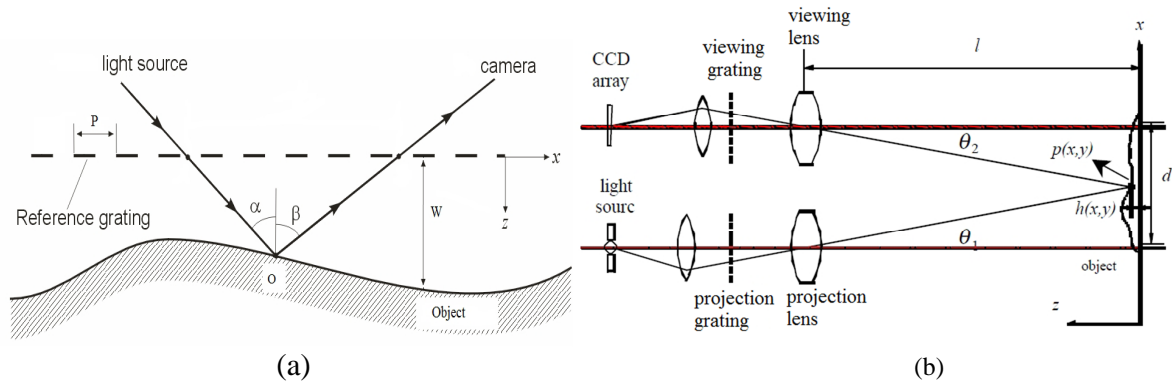
Figure 1.3. Optical setup in (a) shadow moiré, and (b) projection moiré techniques.

1.2 Phase measurement techniques

In phase measurement techniques, the surface geometry information is modulated in phase information, which is thus important in 3D surface reconstruction. Among different types of phase calculation methods, Fourier Transform [31, 32], Phase-Shifting Profilometry [22], and Wavelet Transform analysis [33, 34] are the most common. The required measurement accuracy and resolution, and the number of projected and captured frames are the main factors in the selection of the proper phase-retrieval method. Fourier and wavelet transform methods require one captured frame of a deformed pattern for phase extraction; however, phase shift analysis requires at least three phase-shifted patterns.

Fourier transform techniques process the whole image of a fringe pattern globally using neighboring pixels which influence each other; however, the requirement of neighboring-pixel information prevents extraction of accurate phase at surface discontinuities and edges. Wavelet transform techniques use variable window sizes to process the fringe patterns locally, however with complex computation. Furthermore, wavelet and Fourier transform methods are sensitive to variation of the background intensity and surface reflectivity.

3

Phase-shifting techniques (used in this research) are the most widely used to extract phase information because of their ability to compute high resolution and accurate phase maps. However surface-shape measurement based on these techniques requires projection of at least three phase-shifted patterns. This requirement limits reliability of phase-shift analysis in 3D-shape measurement of dynamics objects (moving or deforming). The intensity distribution of the phase-shifted patterns is described by:

$$I_i(x,y) = a(x,y) + b(x,y)\cos(\Phi(x,y) + \delta_i) \ , \tag{1.1}$$

where $a(x,y)$ and $b(x,y)$ are intensity background and modulation, respectively, (x,y) are the image coordinates, $\Phi(x,y)$ is the phase map that contains object height information, and $\delta_i = 2\pi i/N$ are the phase-shifts between captured images. To calculate the phase map $\Phi(x,y)$, at least three images (N=3) of phase-shifted patterns are required:

$$\Phi(x,y) = -\tan^{-1}\left(\frac{\sum_{i=1}^{N} I_i(x,y)\sin\delta_i}{\sum_{i=1}^{N} I_i(x,y)\cos\delta_i}\right), i = 1,2,\dots,N. \tag{1.2}$$

Because of the arctan function in Eq.1.2, the computed phase $\Phi(x,y)$ is wrapped in the range $[-\pi, \pi]$, and a phase unwrapping technique [35] is required to calculate a continuous phase map $\varphi(x,y)$ (Fig. 1.4). Phase unwrapping is the process that corrects the 2π ambiguities of wrapped phase using the fringe order $m(x,y)$:

$$\varphi(x,y) = \Phi(x,y) + 2\pi m(x,y). \tag{1.3}$$
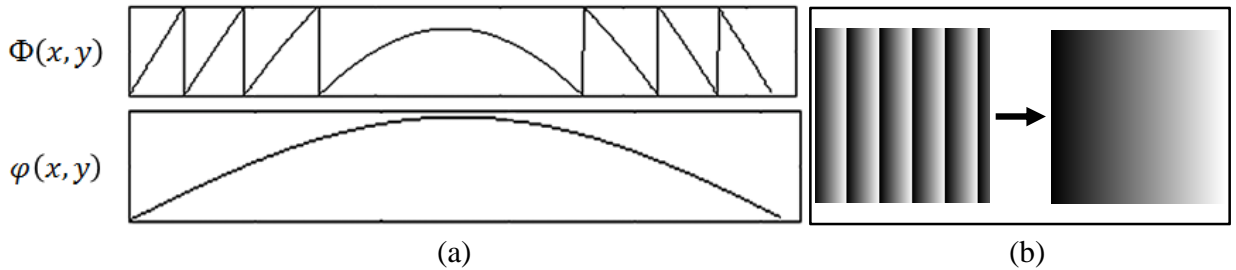
Figure 1.4. Phase unwrapping: a) 1D, and b) 2D.

1.3 Spatial phase unwrapping versus temporal phase unwrapping

Two general approaches to perform phase unwrapping are spatial and temporal phase unwrapping techniques. In spatial phase unwrapping [36, 37], the phase of each pixel is unwrapped based on the phase value of adjacent pixels using only a single phase map; however,

errors occur at surfaces with geometric discontinuities or of multiple spatially isolated objects. In temporal phase unwrapping [38, 39], the phase at each pixel is unwrapped in the temporal domain independently of adjacent pixels, thus preventing error propagation from a noisy phase value at a pixel to adjacent pixels. Therefore, measurement of an object with continuous geometry requires computation of only one phase map and performing spatial phase unwrapping, while measurement of an object with surface discontinuities or spatially isolated objects, commonly requires computation of two or more phase maps by performing temporal phase unwrapping techniques [39]. Other temporal phase unwrapping methods require only one phase map (detailed in Chapter 2), but all temporal phase unwrapping methods require projection of multiple patterns. Minimization of the number of projected and captured frames (while maintaining the level of measurement resolution and accuracy) during the image acquisition stage, is always desirable for measurement of dynamic objects.

1.4 System calibration

To determine the parameters that relate the phase distribution to the 3D coordinates of points of an object surface, system calibration is required. System calibration techniques can be categorized into two general approaches: phase-to-height mapping, used in this research, and fringe-projection stereo-vision.

1.4.1 Phase-to-height mapping

Phase-to-height mapping [40-42] relates phase φ values, computed by phase analysis applied to acquired 2D images of fringe patterns, to object surface height. The relationship of the phase of projected patterns and object height depends on the optical system-geometry parameters (projector-camera relative angle and distance, projector-camera distance to the reference plane, and projected fringe frequency) (Fig. 1.5). For a projector at P and camera at E, at a distance H to the reference plane, with projector-camera distance d and pattern pitch (period width) p, the object height h at point D from the reference plane is given by:

$$h = \frac{H}{1+\frac{2\pi d}{p\Delta\varphi}} \tag{1.4}$$

where φ_A and φ_C are the phase values at points A and C respectively, and $\Delta\varphi = \varphi_A - \varphi_C$. Since in practice, determination of system parameters is difficult, system calibration approaches are commonly used without explicit computation of each system parameter.
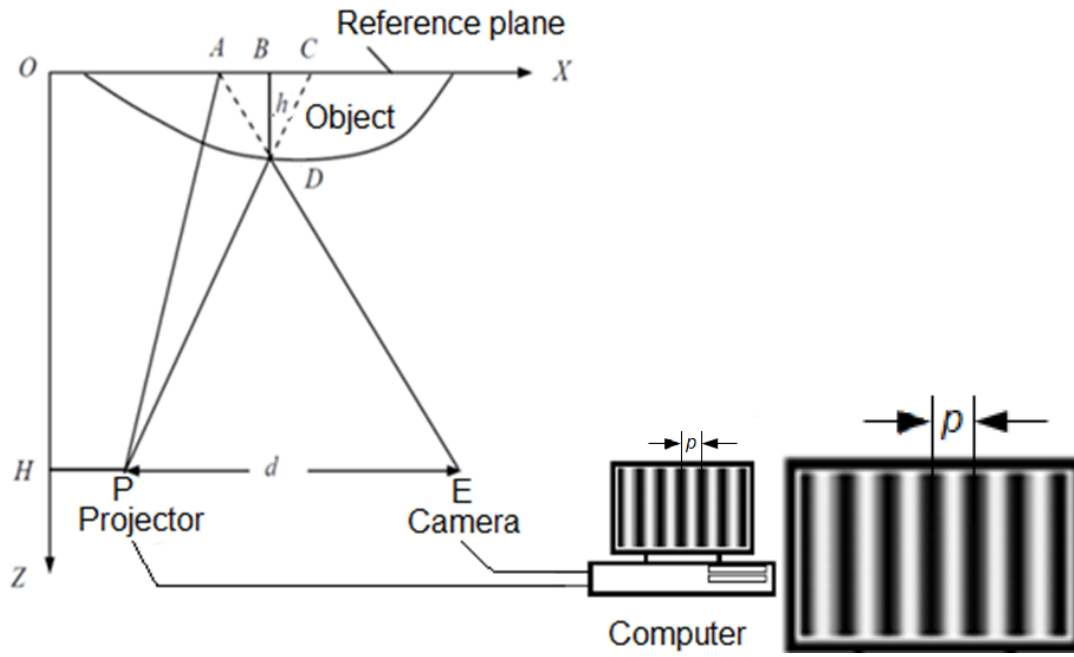
Figure 1.5. System parameters in fringe projection.

1.4.2 Combined stereo-vision with fringe projection technique

The combination of stereo-vision with fringe projection [43-45] allows the 3D real-world coordinates of the object surface to be computed from 2D image coordinates based on established techniques for stereo cameras. A calibration board with known calibration point locations (e.g. vertices of squares on a checkerboard, or white circles on a black background) with several arbitrary poses (positions and orientations) is used for the determination of intrinsic (camera optics) and extrinsic (system geometry) parameters as for stereo cameras [44]. Fringe projection is used to aid determination of correspondence between camera images. Vertical and horizontal fringe patterns are projected, and the intersection of phase values along constant horizontal phase lines, and constant vertical phase lines are used as matching features. For a single-camera projector system [45], the projector is treated as an inverse camera, a virtual projector image is generated, and the calibration parameters for the projector and camera are performed as for a two-camera stereovision system.

1.5 Multi-frame versus single-frame methods

In 3D shape measurement, phase information can be extracted from a single captured image (single-frame or "single-shot") [46] or multiple captured images (multiple-frame) [23, 47]. Using more frames (images) makes it possible to use phase-shift analysis to extract accurate phase values and perform temporal phase unwrapping to handle object discontinuities; however, the use of multiple frames is not desirable for measurement of dynamics objects, since motion of the object between acquired frames may cause phase computation error. Therefore, minimization of the number of projected and captured frames (while maintaining the measurement resolution and accuracy) during the image acquisition stage is highly desirable for 3D measurement of dynamics objects. Even if fast projection techniques could be available (together with fast image capture), single-frame acquisition will always enable faster image acquisition than multiple-frames and minimizing the number of projected patterns will always contribute to faster image acquisition. This is explained further in the context of the rationale in the following section.

1.6 Rationale

Phase-shifting techniques have the advantage of computing an accurate phase map to achieve high spatial-resolution and accurate measurement. However, as mentioned, these techniques require projection and capture of multiple phase-shifted images, which can cause errors when applied to dynamically deforming or moving objects. Fast multi-frame methods [5-8, 47-51] and single-frame techniques [46], which imbed multiple phase-shifted patterns into a single composite pattern, are two approaches that permit phase-shift analysis to be applied to fringe-projection techniques for accurate 3D surface-shape measurement of dynamic surfaces. Because fast image acquisition is one of the most important issues in dynamic object measurement, it is thus desirable to devise methods of 3D surface-shape measurement that require few projected patterns, while still maintaining an accurate measurement.

1.6.1 Approaches and limitations of fast multi-frame techniques

In fast multi-frame techniques [5-8, 47-51], to calculate each phase map, at least three phase-shifted patterns are projected sequentially onto the object at high speed, and a high speed camera captures images of the distorted patterns. Even small object motion between captured frames causes an unknown phase-shift and artifacts in the phase, which can be seen as ripples on the reconstructed surface [12, 13]. The speed of switching patterns in commercial digital light

processing (DLP) projectors is constrained by the low refresh rates (120 Hz for non-LED, 60 Hz for LED-based DLP projectors). To achieve a higher rate of switching phase-shifted frames, hardware modification of the DLP projector is required [48, 49]. Furthermore, due to the small exposure time of the camera with fast projection, a high luminance projector is required, and if used, the bright light would prohibit some applications, for example, scanning human faces. High-speed multi-frame techniques also require complicated camera-projector synchronization. Recent research in LED-based projection systems has improved on the DLP projection rate [50]. However, the high luminance required for multiple-frame projection remains a problem. For all of the multi-frame approaches, the high speed projection is also more costly. Even if these disadvantages are acceptable (higher cost, complex hardware), and even if the rate of acquisition achievable with current systems is fast enough to avoid errors, the demand for measuring even faster moving and faster deforming surfaces than those possible today with current systems, will continue to increase, and the minimization of the number of captured frames required will always contribute to reduce further the effect of object motion on measurement accuracy.

1.6.2 Approaches and limitations of single-frame composite-pattern techniques

Capture of a single-frame instead of multiple frames would be advantageous for measuring moving or deforming objects. Since accurate measurement generally requires multiple phase-shifted images, imbedding multiple patterns into a single projected composite pattern is one approach to achieve accurate single-frame 3D surface-shape measurement [46]. The main limitations of existing single-frame methods based on composite patterns are poor resolution, small range of gray-level intensity due to collection of multiple patterns in one image, and degradation of the extracted patterns because of modulation and demodulation processes on the captured composite pattern image.

1.6.3 Approaches and limitations of digital moiré techniques

Another approach to take advantage of multiple-pattern and single-frame techniques together is to use digital moiré. A single pattern is projected onto the object, a single frame (image) is captured, and then multiple separate phase-shifted moiré images can be generated as a post process (detailed in Chapter 3). The method eliminates the problem of the small range of gray-level intensity in composite-pattern techniques. The post-processing allows digital generation of multiple phase-shifted images separately from the image capture, thus permitting different types

of phase-shift analysis. Furthermore, it removes the modulation and demodulation processes in composite-pattern techniques which cause degradation of the patterns. An accurate phase map can be computed by projecting a single pattern and capturing a single frame. However, in previous attempts to apply digital phase-shifting moiré to 3D surface shape measurement [52-54], there have been significant limitations (described in the following sections) that require further investigation.

1.6.3.1 System calibration

One problem in the digital moiré methods of [52-54] was the use of direct measurement of system-geometry parameters to calculate the height information from the phase distribution. Because the explicit accurate measurement of these parameters is difficult, an accurate system calibration is required to relate calculated phase to height and this has remained a challenge for 3D shape measurement by digital phase-shifting moiré. In optical moiré (shadow and projection) profilometry, the moiré wavelength λ can implicitly represent system geometry parameters [55], and can therefore be used in system calibration. It is common to assume that λ is constant over a small range of depth. However, using a single constant wavelength in system calibration (phase-to-height mapping) limits the range of depth for accurate measurement.

1.6.3.2 High-frequency grid-pattern removal

In moiré profilometry techniques, both optical and digital moiré, the useful moiré patterns are always contaminated with a high-frequency grid-pattern (Fig. 1.2), which must be removed before performing further analysis on the moiré patterns to extract surface height information. In the single-frame digital moiré in [52], a low-pass filter was used to suppress the high-frequency noise originating from the grid pattern, and this filtering results in restrictions on the projected grid frequency. The grid frequency had to be higher than the moiré frequency to clearly separate the frequencies. Furthermore, there was difficulty in selecting the cut-off frequency to completely remove the high-frequency grid without distortion of the moiré pattern. In addition to losing the spatial resolution, the use of the low-pass filter thus limits the measurement range and generation of a clear moiré pattern. The development a new single-frame grid removal technique for application in single-frame digital moiré 3D shape measurement that addresses the needs to remove high frequency grid lines, without introducing artifacts, while preserving the moiré pattern without blurring and degradation, is required.

1.6.3.3 Temporal phase unwrapping

As stated earlier, to extract the phase map, phase-shifting analysis is the most common and accurate technique, because of the high spatial resolution and low sensitivity to variation of background intensity and surface reflectivity possible. However, the computed phase map is wrapped between $-\pi$ and π, and consequently a phase unwrapping algorithm is required to remove the phase ambiguity. While spatial phase unwrapping is suitable for continuous surfaces, to handle object height discontinuities, a temporal phase unwrapping method is required. However, temporal phase unwrapping requires projection of more patterns than for spatial phase unwrapping.

In non-moiré methods, the minimum number of frames to apply temporal phase unwrapping in FPP techniques with phase-coding [56] is five [57]. However in this method, a further algorithm was required to compensate the impact of random noise on measurement due to dithering of defocused binary patterns. Heterodyne temporal phase unwrapping [58] combined with phase-shift analysis permits measurement of discontinuous surfaces. To apply the common heterodyne temporal phase unwrapping using three phase maps, FPP methods require the projection and capture of at least nine images (three patterns at three frequencies), which would tend to cause phase error in measuring dynamic objects, either moving or deforming.

Temporal phase unwrapping has been applied to digital moiré methods using fewer projected and captured patterns (two frames) [54]; however, the calculated continuous phase map had a low signal-to-noise ratio. Two-frequency phase-shifting projection-moiré [59, 60], was also developed for measurement of discontinuous surfaces. However, in addition to the capture of four phase-shifted moiré patterns at each frequency (using mechanical translation of grating), the absolute fringe order was only estimated using grating pitches applied at different frequencies, which causes error in the phase unwrapping process. It would be desirable to devise a method of temporal phase unwrapping that reduces the number of required projected patterns, while still maintaining a high spatial resolution and accurate measurement of discontinuous surfaces.

1.7 Objectives

For certain applications of moving or deforming objects, real-time 3D measurement may not necessary. The speed of the image acquisition stage (2D image acquisition of projected patterns on the object surface) would thus be the most important in 3D-shape measurement of moving or deforming objects, and the phase extraction and phase-to-height mapping could be done as a post-process. Capturing the fewest frames during the image acquisition stage of 3D object surface shape measurement will thus always be important for high-speed applications. The main goal of this research is to develop new methods with off-the-shelf system components (single camera and single projector), for full-field 3D-shape measurement of objects using the fewest required projected patterns, while achieving the best possible measurement resolution and accuracy. High speed in all stages of measurements including 2D-image acquisition, phase retrieval, and 3D-coordinate computation is important in 3D real-time profilometry. However, the focus of this research is to develop methods that reduce the number of captured frames in the 2D-image acquisition stage, while maintaining high quality measurement. Even if well synchronized fast pattern projection and image capture hardware and software were available, minimizing the number of captured frames during the image acquisition stage will always contribute to faster image acquisition. The detailed objectives of this research are as follows:

1. Develop digital moiré for single-frame 3D-shape measurement of objects without surface discontinuity:

    1.1 Develop a new calibration technique in digital moiré to compute height from phase without requiring direct measurement of the system geometry.

    1.2 Investigate pixel-wise phase-to-height mapping system-calibration based on moiré-wavelength refinement to enable object measurement over extended depth without decreasing measurement accuracy.

2. Develop new single-frame grid removal techniques for application in single-frame digital moiré 3D shape measurement to addresses the needs to remove high frequency grid lines, without introducing artifacts, while preserving the moiré pattern without blurring and degradation.

3. Developed new temporal phase unwrapping techniques for measurement of spatially isolated and discontinuous surfaces:

3.1 Develop a new temporal phase unwrapping technique using multi-wavelength digital phase-shifting moiré to address the limitations of the high number of projected and captured images of temporal phase unwrapping in FPP, and the low signal-to-noise ratio of the extended phase map of temporal phase unwrapping in digital moiré.

1.8 Thesis outline

The remainder of the thesis is organized as follows. Chapter 2 reviews existing fast-2D-image-acquisition 3D optical metrology, temporal phase unwrapping, and digital moiré. Chapter 3 details a new single-frame digital phase-shifting 3D shape measurement method that uses a new system calibration technique by pixel-wise moiré-wavelength and height (depth) refinement, and includes experiments to demonstrate improvement in measurement accuracy compared to measurement using a single global wavelength across all pixels. Chapter 4 presents a new improved grid removal method for single-frame digital moiré 3D shape measurement, and includes experiments performed on moiré-pattern images containing grid lines, generated by digital moiré, for several test objects, for comparison of the new method to previous grid removal techniques. Chapter 5 presents new methods of two-image and three-image temporal phase unwrapping using multi-wavelength digital phase-shifting moiré with experiments to demonstrate improved phase measurement with two spatially isolated objects including an object with surface discontinuities. Chapter 6 discusses contributions of this research and future work.

Chapter 2

Background and Literature Review

This chapter reviews existing fast-2D-image-acquisition 3D optical metrology, temporal phase unwrapping, and digital moiré. For 3D shape measurement of dynamic objects (with either moving or deforming surfaces), using fewer projected fringe patterns contributes to faster acquisition of the required 2D images (frames) of the patterns, and thus to capturing higher object dynamics while avoiding motion artifacts. Projection of a single fringe pattern with certain measurement methods could be sufficient for certain conditions (objects with continuous geometry) and levels of accuracy. However, for accurate measurement of objects with complex geometry (surface discontinuities), other techniques are required. Fast multi-pattern projection techniques, and methods that aim to minimize the number of projected patterns are two general optical approaches for fast 2D image acquisition in 3D shape measurement of dynamic objects.

2.1. Fast-2D-image-acquisition 3D optical metrology

2.1.1 Fast multi-pattern projection (hardware modification or new projector design)

In fast projection techniques [5-8, 47-51], multiple patterns are projected sequentially onto an object with synchronized image capture. While high speed projection is used to minimize the effect of object motion during measurement, even small object motion between captured frames may cause an additional unknown phase-shift and motion artifacts in the measurement, which can be seen as ripples on the reconstructed surface [12, 13]. The speed of switching patterns in commercial digital light processing (DLP) projectors is constrained by the low refresh rates. To achieve a higher rate of switching frames, these methods require costly projector hardware modification [48, 49] or new designs of projection systems [50, 51] to increase the projection rate beyond the capabilities of off-the-shelf projectors. For example, modification to a DLP projector (by removing the color wheel and using a micro-controller to trigger the digital micro-mirror device (DMD) and projector-camera synchronization [48, 61]), configuration of a new projector to generate patterns using an array of LEDs with minimal switching time [50], and using fiber interference for fast generation of fringe patterns [51], have been used for fast multiple-pattern projection. Furthermore, due to the small camera exposure time with fast projection, a high luminance projector is required, which could prohibit some applications. Even

if these disadvantages were acceptable (higher cost, complex hardware), and even if the rate of acquisition achievable with current systems were fast enough to avoid errors, the demand for measuring even faster moving and faster deforming surfaces than those possible today with current systems, will continue to increase, and the minimization of the number of captured frames required will always contribute to reduce further the effect of object motion on measurement accuracy.

2.1.2 Minimization of number of projected patterns

2.1.2.1 Single-pattern projection with single-frame (image) capture

There are several techniques which use only a single projected pattern and captured image in the 2D image acquisition stage to perform 3D surface-shape measurement. Both gray-scale and colour pattern methods have been used.

Among gray scale pattern methods, Fourier-based [62], regularized phase-tracking [63, 64], and local model-fitting [65, 66] have been used to compute a phase map from a single fringe pattern. Since these methods compute only one phase map, these methods are only useful for 3D shape measurement of continuous surfaces (without complex geometry or discontinuity). Moreover, the phase accuracy obtained from these methods [62-66] is low due to sensitivity to variation of the background intensity and surface reflectivity.

In colour pattern techniques, a single projected image is composed of a single sinusoidal intensity fringe pattern and colour-coded stripes (Fig. 2.1) [67]. A phase map is extracted from the single fringe pattern and absolute fringe order is determined from the colour-coded stripes. This prevents unwrapped-phase error propagation under conditions of noise and surface discontinuities. However, due to overlap of the fringe pattern and colour-coded stripes, the calculated phase and the edge identification of stripes are not accurate. Moreover, using a colour pattern is not desirable for measuring coloured objects. Another method uses binary stripes with colour grids [68] to facilitate identification of fringe order and distinguishing of the binary stripes. The method can better handle 3D measurement of coloured objects compared to the previous method; however, the use of colour grids with binary stripes lowers the intensities, which makes it difficult to distinguish edges of the binary stripes.

Digital moiré [25] is another method that permits single-pattern projection with single-frame capture. This is discussed in detail in Section 2.3.
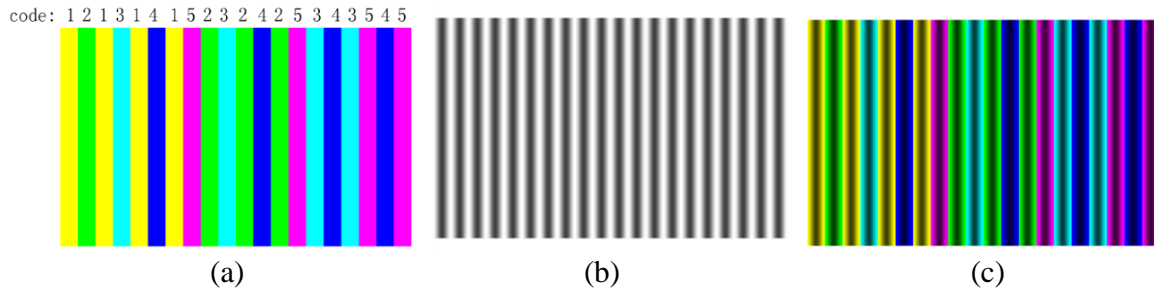
Figure 2.1. (a) Colour encoded stripes (b) cosinoidal intensity fringes (c) combination of (a) and (b) [67].

2.1.2.2 Multiple-patterns in a single composite pattern

By embedding multiple phase-shifted patterns into a single gray-scale image utilization of phase-shifting analysis can be achieved with one captured frame. However, the small gray-level range of fringe-patterns when accumulating multiple patterns into one image and the repeated use of filters to separate phase-shifted patterns from captured images lead to reduced measurement accuracy. Also, the high frequency carrier detection for reliable depth recovery is highly dependent on the intensity and spatial resolution of the projector and camera.

One gray-scale technique used for single-frame 3D measurement imbeds multiple patterns into a single projected composite pattern [69, 70] by multiplying phase-shifted patterns by a cosine wave with different carrier frequencies and computing the sum (Fig. 2.2a). To demodulate the captured image, band-pass filters separate each channel (Fig. 2.2b). However, due to perspective distortion, the cosine carriers have an unknown phase shift, and several operations are required to retrieve the final phase map (Fig. 2.2b).
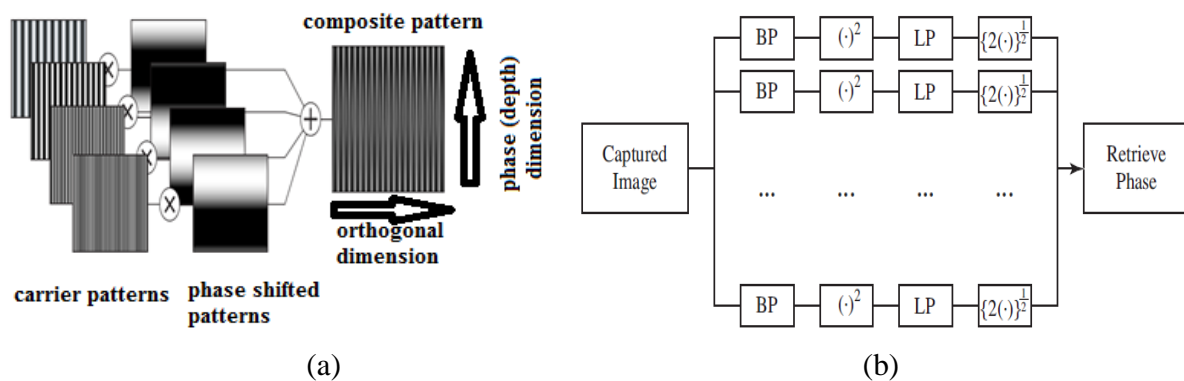
Figure 02.2. (a) Procedure of generating composite pattern, (b) Demodulation procedure in composite pattern projection technique (BP: band-pass filter; LP: low-pass filter) [69].

16

To handle surface discontinuities by single-frame projection and capture, the spatial frequency-multiplex Fourier transform was used to extract multiple phase maps with various phase sensitivities to object height [71]. A pattern composed of multiple sinusoids with k different, two-component spatial carrier frequencies $(f_{x,k}, f_{y,k})$ were projected (Fig. 2.3), and the Fourier transform extracted individual phase maps, which were unwrapped by [72]. The carrier frequencies control the fringe sensitivity and separation of multiplexed signals in the frequency domain.
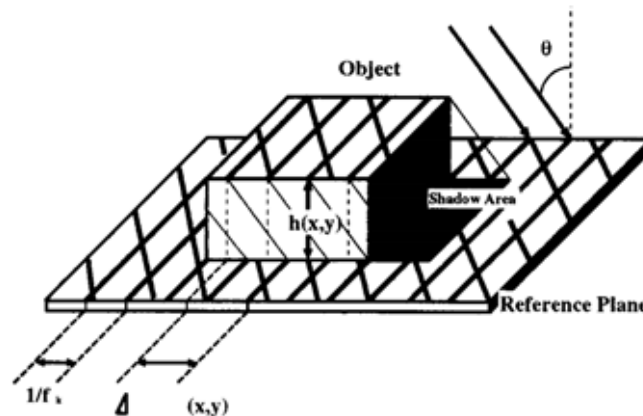
Figure 02.3. Frequency multiplex composite pattern [71].

A micro-polarizer-array camera approach [73, 74] uses polarizing grids to acquire four phase-shifted images simultaneously and permit single-frame acquisition of multi-phase-shifted patterns (Fig. 2.4); however, it requires complex optical hardware for projection of polarized light. Furthermore, to avoid compromised spatial resolution, sequential measurements are required, making the technique multi-frame.
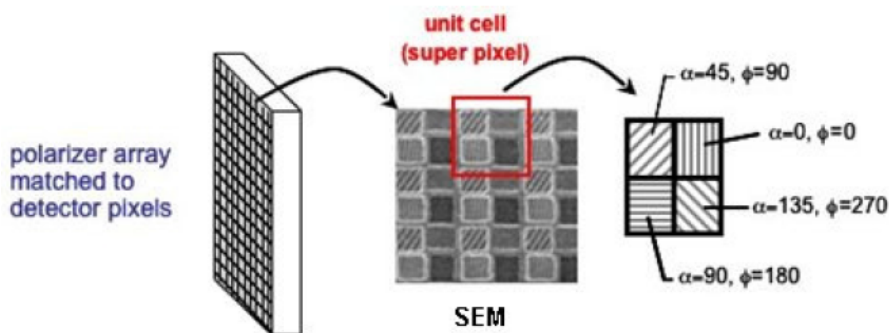
Figure 2.4. Diagram of pixelated micro-polarized array [74].

17

Another approach to achieve single-frame multi-pattern measurement uses red, green, and blue channels to modulate three phase-shifted patterns within a single colour composite pattern (Fig. 2.5a) [75]. In [76], the colour channels are used as a carrier to code three fringe patterns with different frequencies (Fig. 2.5b). The fringe frequencies are chosen based on the optimum, three-frequency method with N, $N-1$, and $N-\sqrt{N}$ fringes across the pattern. The colour composite fringe pattern is projected onto the object and the wrapped phase map is calculated for each colour channel based on the Fourier transform method. This three-frequency method resolves the fringe order ambiguity with the beat frequency of the first and second fringe as the third frequency, whose pattern covers the full field of view. In [77] (Fig. 2.5c) encoding of sine and cosine fringe patterns in red and green channels is used to extract the wrapped phase, and a stepped intensity pattern encoded in the blue channel is used to unwrap the phase map extracted from two fringe patterns. However, in all colour composite pattern methods, colour channel crosstalk and colour imbalance (mismatch of colour spectra between camera and projector) result in errors in the extracted phase [78]. Therefore, for highly accurate measurement, using a gray-scale pattern or even binary pattern is typically preferable.

(a)   (b)   (c)
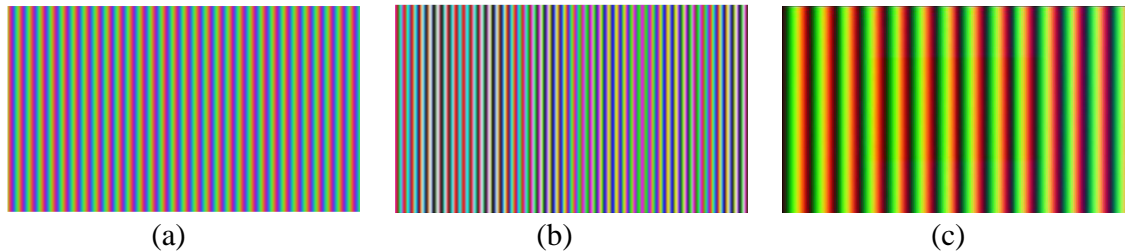
Figure 2.5. Composite colour fringe patterns: (a) three sine fringe patterns with $2\pi/3$ phase shift, (b) three sine fringe patterns with optimum fringe number (42,48,49), and (c) sine and cosine fringe patterns encoded into green and red channels and stepped intensity pattern into blue channel [75-77].

2.1.2.3 Coded-patterns

In sequential binary-coding pattern projection techniques [14, 79-81], black and white stripes provide a unique binary code to each surface point of an object (Fig. 2.6). These techniques are very reliable, however projection of a large number of binary-coded patterns is required to achieve a high spatial resolution, which is not suitable for 3D measurement of dynamics objects.
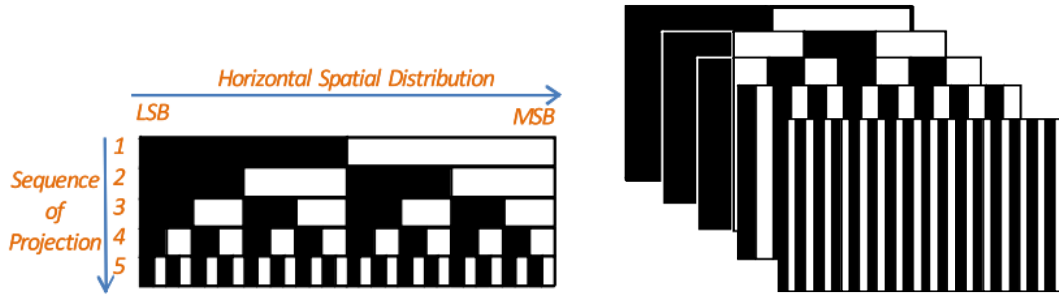
Figure 2.6. Sequential binary-coding pattern projections [14].

Gray-coded patterns decrease the number of projected patterns significantly [82-84]. In these techniques, using N number of projected patterns with M distinct gray levels of intensity provides M^N unique codes.
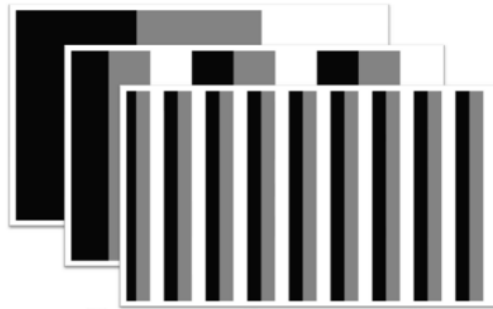
Figure 2.7. Gray-Coded pattern $N=M=3$ [14].

2.1.2.4 Single marker or stripe encoding on phase-shifted FPP

Encoding a single marker or single stripe [85, 86] on three phase-shifted fringe patterns have been used to calculate absolute phase values using spatial phase unwrapping techniques. However, spatial phase unwrapping methods will fail to measure objects with surface geometry discontinuities, and are thus not discussed further.

2.1.2.5 Dual-frequency pattern projection

To determine fringe order in phase-shifted fringe projection techniques, a dual frequency pattern projection technique [1] has been developed using low and high frequency patterns embedded into a single dual-frequency pattern. The high-frequency phase is unwrapped using the low-frequency phase. In [1], the minimum number of patterns projected onto the object was five to apply five-step phase-shift analysis. However, encoding two frequency phases into a single pattern decreases the extracted phase accuracy in this method, compared to the phase accuracy of single frequency phase encoding methods.

19

2.1.2.6 Combined coded-patterns and fringe projection

Projection of only a few coded-patterns alone leads to low spatial resolution in measurement, while increasing the number of projected coded patterns to achieve high spatial resolution in measurement is not suitable for measurement of dynamics objects. To decrease the number of projected coded patterns and to maintain high spatial resolution in measurement, combined projection of coded patterns with separate phase-shifted fringe patterns was developed. In these techniques, the projection of phase-shifted fringe patterns provides a high-resolution wrapped phase map, and coded-patterns help the phase unwrapping process to determine the fringe order. Gray-coding, spatial-coding, and phase-coding all combined with phase-shifting methods are common pattern-coding methods.

2.1.2.6.1 Gray-coding combined with phase-shifting fringe projection

Gray-coding combined with phase-shifting FPP [87, 88] is based on the projection of eleven patterns. The first seven patterns are formed such that their projection corresponds to the formation of a gray code of seven bits. To generate four phase-shifted fringe patterns, the pattern of the gray-code sequence is generated and then spatially shifted by a fraction $p/4$ of its spatial period p and finally digitally smoothed to get a sinusoidal profile. The gray-coding phase unwrapping methods are not suitable for dynamic object measurement, since they require projection of many binary patterns to determine fringe orders.

2.1.2.6.2 Spatial-coding combined with phase-shifting fringe projection

In comparison to gray-code phase unwrapping, the method of spatial-coding temporal phase [89] unwrapping requires projection of fewer patterns onto an object; however the method requires the knowledge of adjacent pixel information, which makes them unsuccessful for surfaces that are not locally continuous.

2.1.2.6.3 Phase-coding combined with phase-shifting fringe projection

In phase-coding phase unwrapping techniques [56, 90, 91] the code word required to determine the fringe orders are embedded into the phase instead of intensity. Therefore, they are robust to the variation in surface contrast and ambient light, and camera noise. The number of projected patterns in the phase-coding technique proposed in [90] is six: three phase-encoded patterns in addition to three phase-shifted fringe patterns. In [91], one phase-shifted fringe pattern is combined with one phase-coded pattern in a single colour image. A total of three colour images thus need to be projected. However, projection of colour patterns leads to less accurate phase

maps due to colour channel crosstalk and colour imbalance in separation of fringe pattern and coded pattern. In another method [57], five projected patterns are required; three binary dithered patterns are projected separately to calculate the wrapped phase map, and the average intensity of the dithered pattern combined with two additional phase-coded patterns are used to determine the fringe order and perform phase unwrapping. However a further algorithm is required to compensate random noise impact on the measurement due to dithering and defocusing [57].

2.2 Temporal phase unwrapping

To handle object discontinuities, temporal phase unwrapping and thus projection of multiple patterns is required. On the other hand, minimizing the number of projected patterns is always preferable in measuring dynamics objects. Different temporal phase-unwrapping algorithms [92] have been developed, including coded-pattern projection and temporal phase unwrapping using additional phase maps with different fringe periods.

2.2.1 Temporal phase unwrapping using coded-pattern projection

As described in Section 2.1.2.6, the projection of phase-shifted fringe patterns, which provide a high-resolution wrapped phase map, has been combined with pattern coding, such as gray-, spatial-, and phase-coding, which aid to determine the fringe order. The limitations of these methods have been described in Sections 2.1.2.6.1 to 2.1.2.6.3.

2.2.2 Temporal phase unwrapping using additional phase maps

Temporal phase unwrapping using additional phase maps [93-95] are more accurate than coded-pattern projection temporal phase unwrapping. Moreover, the computational simplicity of these methods makes it possible to use them for dynamic measurement. Multi-frequency (hierarchical) [96-98], multi-wavelength (heterodyne) [58, 99-101], and number-theoretical approaches [102-104] are different categories of temporal phase unwrapping techniques using additional phase maps. In comparison to other techniques, heterodyne temporal phase unwrapping methods have highest flexibility in selecting the fringe frequency (wavelength), and less sensitivity to spike-like error in fringe-order number [92].

Heterodyne temporal phase unwrapping, used in this research, employs multiple phase maps with different fringe frequencies to create a new synthetic phase map with extended unambiguous phase range. In heterodyne phase unwrapping, two shorter wavelengths were first used to synthesize a longer beat wavelength [105]; however, the synthetic phase was noisy in

comparison to single wavelength analysis. To improve two-wavelength analysis, the unambiguous and continuous phase value of the beat wavelength can be used as a reference phase to unwrap the phase of the smaller wavelengths [105, 106], and three and multiple-wavelength temporal phase unwrapping can further extend the beat wavelength to increase the measureable height with less noise [107, 108]. In FPP, projection of lower frequency fringe patterns yields fewer phase jumps (Fig. 1.4) and decreases the number of projected fringe patterns with different fringe frequencies required for the period corresponding to the beat frequency to cover the whole field of view, thus providing a continuous extended phase map without ambiguity. However, this method results in a noisy phase map [109]. Projection of fringe patterns with higher frequencies leads to higher quality (less noisy) phase maps; however, more phase jumps occur. To obtain an accurate full continuous extended phase map, a higher number of projected fringe patterns with different frequencies are required [94]. In FPP, calculation of the phase map for each fringe frequency requires the capture of at least three phase-shifted images. Therefore, to apply heterodyne temporal phase unwrapping using three different phase maps, FPP methods require the projection and capture of nine images, which may cause phase error in measuring dynamic objects, either moving or deforming. It is thus desirable to devise a method of temporal phase unwrapping that reduces the number of required pattern projections, while still maintaining an accurate full continuous phase map.

2.3 Digital Moiré

To benefit from the advantages of multi-pattern projection of phase-shifted fringes and single-frame techniques, without combining phase-shifted patterns into one frame, a digital moiré technique [18] can be used. In digital moiré [110], moiré patterns are generated by projecting a computer-generated grid onto the object (Fig. 2.8), capturing a single frame from an angle (Fig. 2.9a), and in a post-process, superimposing a synthetic grid of the same frequency as in the captured image (Fig. 2.9a) to obtain a moiré pattern (Fig. 2.9b), while phase-shifting is carried out as a post-process simply by digitally shifting the synthetic grid across the captured image using digital image processing to obtain a phase-shifted moiré pattern (Fig. 2.9c). The digital post-process phase-shifting generates separate phase-shifted moiré patterns in separate images, and thus eliminates the problems associated with multiple phase-shifted patterns combined in a single composite pattern. As a result, a high quality (resolution and accuracy) phase map can be computed by capturing a single image. This advantage of digital moiré provides an opportunity

to decrease the number of patterns projected. However, in previous attempts to apply digital phase-shifting moiré to perform 3D surface-shape measurement [52-54], there have been significant limitations.
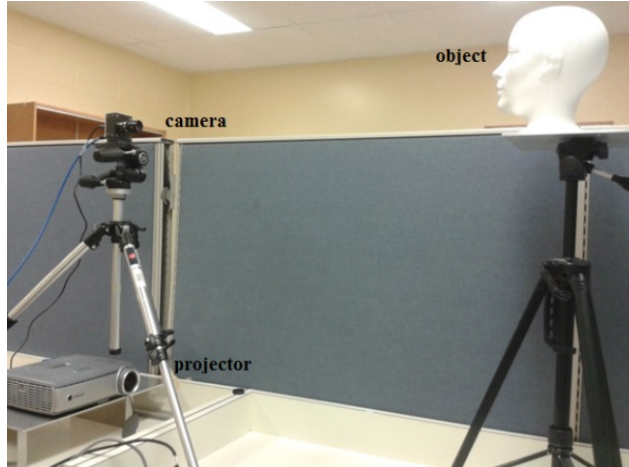
Figure 2.8. Optical setup of the digital moiré technique.

(a)	(b)	(c)
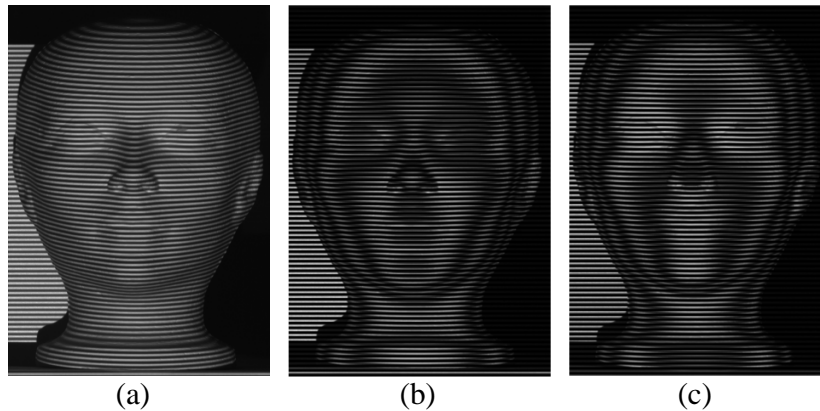
Figure 2.9. (a) Captured image of line patterns on a manikin head, (b) generated moiré pattern based on digital moiré, and (c) phase-shifted moiré pattern.

2.3.1 System calibration in digital moiré

In the digital moiré technique in [52], the computation of surface height from phase was performed using direct measurement of system parameters, without system calibration of phase-to-height mapping. Accurate system calibration has since remained a challenge for 3D shape measurement by digital phase-shifting moiré. In optical moiré (shadow and projection) profilometry, the moiré wavelength λ can implicitly represent system geometry parameters [55], and can be therefore used in system calibration. However, moiré wavelength was only used for

23

measurement of objects with small range of depth, such as optical lenses. Therefore, a new method of system calibration is required to avoid the need for optical-setup parameter measurement, as well as handle a greater range of calibration depth.

2.3.2 Grid removal in digital moiré

For optical and digital moiré techniques, the superposition of the grid lines with the deformed light pattern generates an image containing useful moiré contours with encoded surface-height information, as well as unwanted high-frequency grid lines. In order to calculate the object surface height from the moiré contours, the generated images must be free of grid lines. Several grid removal methods, including time averaging [111], multiple-image discrete averaging [112], and single-image filtering [52, 113], have been used in moiré profilometry but all methods have limitations. In-plane translation of the grating in shadow moiré [111, 114] and synchronized in-plane translation of the projection and viewing gratings in projection moiré [29, 115] can eliminate the grid lines by continuous time-averaging image capture of the grid (during a single camera time-exposure). In-plane grating translation in shadow moiré and synchronized in-plane translation of the gratings in projection moiré to multiple equidistant positions and discrete averaging of the images captured at these static-grating positions can also eliminate the grid lines [112, 116]. Alternatively, discrete grid averaging can be achieved without mechanically moving any optical components using two separate liquid crystal light modulating grids [117]. However, the main limitations of these averaging processes in grid removal are the requirement of precise grid translation for discrete and continuous methods, and the need to capture more than one frame for discrete averaging. Multiple-frame capture is a disadvantage for 3D shape measurement of dynamic object surfaces, either moving or deforming, because of the higher risk of motion artifacts compared to single-frame measurement. Digital moiré permits measurement using only a single frame (image capture) of the projected grid on the object with a continuous surface using only one phase map. However, digital moiré sacrifices the advantages of shadow and projection moiré of acquiring grid-free moiré contours (by the in-plane grating translation and simple intensity averaging described above). A single-frame grid removal technique is therefore required in order to permit single-frame moiré-based measurement.

Low-pass filtering (LPF) has been used for single-frame grid removal in digital moiré [52]. However, LPF causes blurring and smearing of the fine details of moiré contours and furthermore, requires clear separation between the moiré contour and grid frequencies in order to

24

set a suitable cut-off frequency. Grid removal in digital moiré was also achieved without LPF by sequentially projecting and capturing images of multiple shifted grids, and performing discrete image averaging [53]. However, the multiple-image capture rendered the method a multiple-frame technique.

The Stationary Wavelet Transform (SWT) has been used for single-frame grid removal in simulated shadow moiré [113] and performs well in removing grid lines and preserving fine details without introducing artifacts to the de-noised image in comparison to LPF. However, SWT only works well in removing straight lines, and is unable to completely remove curved grid lines, which occur in regions of large changes in depth. Increasing the decomposition level could improve grid removal, but at the cost of excessive smearing of moiré contours. Therefore, a reliable single-frame grid removal technique is required to completely remove the high frequency grid (both straight and curved lines) without introducing artifacts, and preserve the moiré pattern without blurring and degradation.

2.3.3 Temporal phase unwrapping in digital moiré

In moiré fringe profilometry, methods have been developed to minimize the number of projected patterns for temporal phase unwrapping. Within plane rotation of two gratings in opposing directions generates open moiré patterns with different pitches [118]; however, the application of Fourier transform to extract the phase map limits accuracy, and the requirement of physical and precise mechanical rotation of gratings limits applications, especially for dynamic object measurement. In colour grating projection moiré [119], a colour projection grating is used with a black and white viewing grating. Three moiré phase maps with different wavelengths can be computed and used in temporal phase unwrapping; however, colour channel crosstalk and colour imbalance make colour stripe separation difficult. Two-frequency phase shifting projection moiré topography [59, 60], was also developed to cope with the measurement of objects with discontinuities and spatially isolated objects. However, in addition to the capture of four phase-shifted moiré patterns at each frequency (using mechanical translation of grating), the absolute fringe order was only approximated using grating pitches applied at different frequencies, which causes error in the phase unwrapping process.

In digital moiré, a single grid image is projected and captured and phase shifting is performed digitally in a post process. These benefits were utilized in [54] to achieve digital-moiré temporal phase unwrapping with few images. Two fringe patterns with different

frequencies were projected separately onto an object surface to calculate two phase maps with different wavelengths, and the extended phase map was then calculated by subtracting the two phase maps. While this technique can handle surface discontinuities, the calculated extended phase map has a low signal-to-noise ratio (SNR). Therefore, a method of accurate temporal phase unwrapping is required using few projected patterns while maintaining an accurate continuous phase map.

2.4 Discussion

The speed of the image acquisition stage (2D image acquisition of projected-patterns on the object surface) is important in the 3D-shape measurement of moving and deforming objects to avoid motion artifacts. Digital moiré has the advantageous of minimizing the number of patterns projected compared to FPP; however there have been significant limitations in current digital moiré techniques. Lack of suitable methods for system calibration over extended depth, high frequency grid removal, and temporal phase unwrapping, have been the main limitations of digital moiré techniques.

Direct measurement of optical system parameters in digital moiré, and small range of depth measurement in optical moiré (shadow and projection methods) are two main limitations in previous system calibration techniques in moiré profilometry. A new calibration method is developed, as detailed in Chapter 3, to address the limitation of previous system calibration and to handle a greater range of calibration depth.

The requirement of precise mechanical grid translation, and capture of multiple frames are the main limitations of continuous and discrete averaging grid removal methods, respectively. Blurring of moiré pattern, introduction of artifacts, and inability to completely remove curved grid lines are the main limitations in previous single-image filtering grid removal techniques. The developed single-image filtering method detailed in Chapter 4, removes high frequency grid lines, both straight and curved lines, without introducing artifacts, while preserving the moiré pattern without blurring and degradation.

To perform temporal phase unwrapping in moiré, plane rotation of two gratings in opposing directions has been developed. However, application of Fourier transform to extract the phase map and requirement of physical and precise mechanical rotation of gratings are the main limitation of this technique. Colour channel crosstalk and colour imbalance are the main limitations of temporal phase unwrapping using colour grating projection moiré. Absolute fringe

order approximation using grating pitches developed in two-frequency phase shifting projection moiré makes that temporal phase unwrapping procedure unreliable. Further limitations of previous temporal phase unwrapping methods are the high number of projected and captured images used in FPP, and the low signal-to-noise ratio of the extended phase map in digital moiré approaches. An improved temporal phase unwrapping was developed to address these limitations, as detailed in Chapter 5.

The new digital moiré techniques developed in Chapters 3 to 5 minimize the number of projected patterns, while maintaining accurate 3D surface-shape measurement either with continuous or discontinuous surface geometry.

Chapter 3

Digital moiré system calibration
by pixel-wise moiré-wavelength refinement

In this chapter, a novel pixel-wise moiré-wavelength refinement technique was developed for system calibration in single-frame digital phase-shifting 3D shape measurement. The method requires projection of only a single binary grid pattern and capture of a single image frame.

3.1 Overview of 3D shape measurement and calibration

The 3D shape measurement method includes the following steps (Fig. 3.1), each of which is explained in detail in Sections 3.2 to 3.6. A binary grid pattern is projected onto the object and a single frame of the deformed grid is captured by camera (Fig. 3.1a, Section 3.2). Phase-shifted images (containing moiré pattern and grid) are digitally generated (Fig. 3.1b, Section 3.2). Pure moiré patterns are extracted from the generated images by grid removal (Fig. 3.1c, Section 3.3). Phase is extracted from moiré patterns by phase-shift analysis (Fig. 3.1d, Section 3.4). System calibration is performed to determine the phase-to-height mapping (Fig. 3.1e, Section 3.5). Height is computed from phase using pixel-wise moiré-wavelength refinement and the phase-to-height mapping (Fig. 3.1f, Section 3.6).

As commonly done in optical metrology, the full process of measurement system calibration is carried out only once before height computation from phase [24]. However, in this thesis, one calibration parameter, the moiré-wavelength, is refined based on an initial surface height measurement as detailed in Section 3.6.

3.2 Generation of phase-shifted images from single frame capture

The entire image acquisition process consists simply of projecting a binary grid pattern (black and white parallel-lines) onto the object surface, and capturing a single frame (image) of the deformed lines on the object surface by a camera (Fig. 3.1a). Then in a post process, a synthetically produced (computer generated) grid of the same pitch (period) as the captured frame is overlaid on the captured image and digitally shifted to generate multiple phase-shifted images [110]. In comparison to conventional shadow [26] and projection moiré [29], the ability to perform phase-shifting as a digital post-process to the frame (image) capture rather than optically, avoids complicated setup, and permits flexibility in adjusting the grid pitch, number of

28

phase-shifted patterns, and amount of phase shift. Furthermore, the projection of a binary grid pattern has the advantages of avoiding gamma nonlinearity [8].

a. Grid projection and single frame capture **b. Generation of phase-shifted moiré patterns** **c. Extraction of moiré patterns by grid removal**

d. Wrapped phase **Unwrapped phase** **e. System calibration** **f. 3D point cloud from phase to height computation**
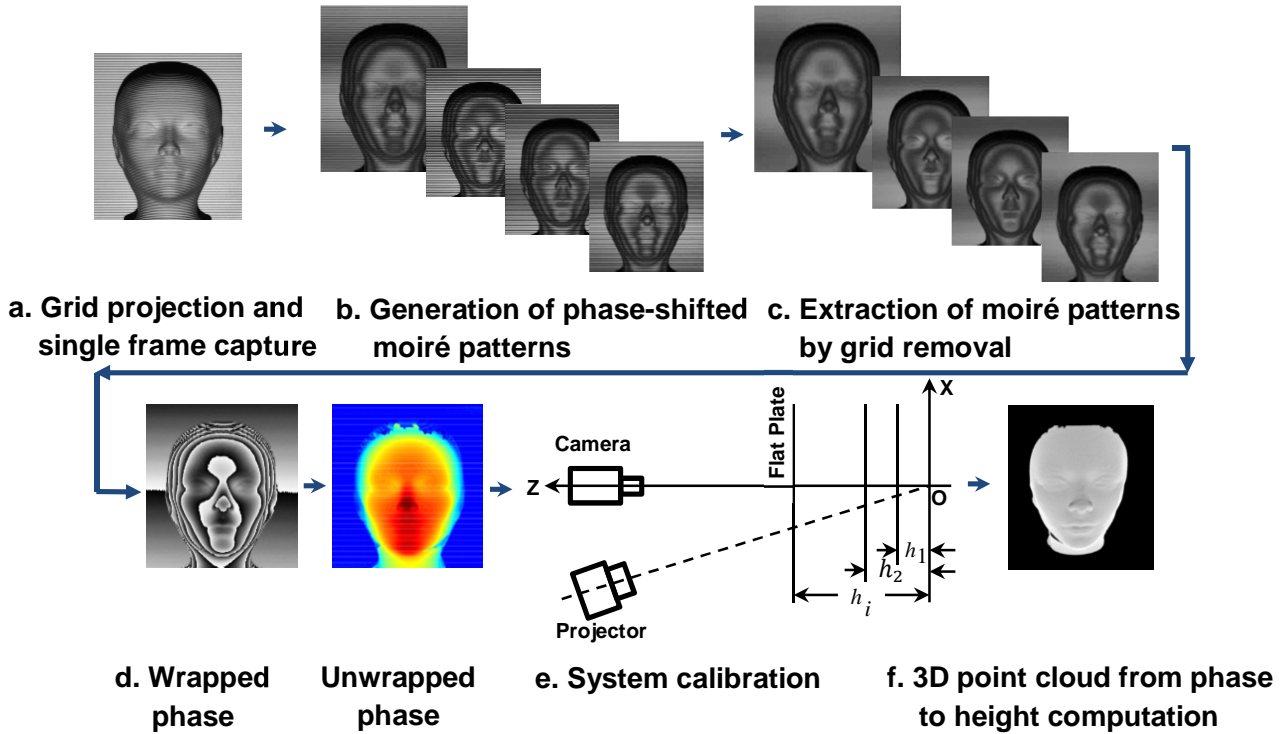
Figure 3.1. Procedure of 3D object-shape measurement based on single-frame moiré.

Since the phase shifting is performed digitally, it is not possible to perform subpixel shifting of the superimposed synthetic grid. Thus, the constraint on the amount of phase shift δ is that it should not require subpixel shifting. The smallest amount of phase shift that can be performed digitally is one pixel. Using this one-pixel shift gives flexibility in the amount of phase shift for the remaining images and in the number of phase shifted images that can be used. Such an approach of phase shifting and phase extraction, developed for conventional shadow moiré [120], is thus used here for digital moiré. Four phase-shifted patterns, required to extract the phase map, are generated as follows:

The first phase-shifted frame is produced by superimposing the computer-generated grid onto the captured frame and is considered to have zero phase-shift:

$$I_1(x, y) = a(x, y) + b(x, y)\sin\big(\Phi(x, y)\big) \, , \tag{3.1}$$

where $I_1(x, y)$ is the intensity map, $a(x, y)$ and $b(x, y)$ are intensity background and modulation, respectively, (x, y) are the image coordinates, and Φ is the phase value that contains object height information. The computer-generated grid is then translated digitally by half of its pitch (period), to generate the second frame with phase shift π with respect to the first frame:

$$I_2(x, y) = a(x, y) + b(x, y)\sin\left(\Phi(x, y) + \pi\right). \tag{3.2}$$

The third frame is generated by translating the computer-generated grid by a single pixel with the aim of achieving the smallest amount of phase shift with respect to the first frame:

$$I_3(x, y) = a(x, y) + b(x, y)\sin\left(\Phi(x, y) + \delta\right). \tag{3.3}$$

The amount of phase shift thus depends on the resolution of the captured frame. For instance, if the grid pitch in the captured frame is 6 pixels, the smallest amount of phase shift generated by translating the computer-generated grid by one pixel is $\delta = 2\pi/6$. Finally, the fourth frame is generated with a phase shift of π with respect to the third frame:

$$I_4(x, y) = a(x, y) + b(x, y)\sin\left(\Phi(x, y) + \delta + \pi\right). \tag{3.4}$$

The resulting phase-shifted images (Fig.3.1b) contain the moiré contours generated by the interference of the projected and overlaid synthetic grids, as well as unwanted high-frequency grid patterns. These grid patterns must be removed in order to extract the pure moiré patterns, from which phase information and object surface height will be computed.

3.3 Extraction of moiré pattern by wavelet-Fourier grid removal

To remove the unwanted high frequency periodic grid pattern and thus extract the pure moiré patterns from the generated phase-shifted images, Fourier transform [52] and wavelet transform [113] techniques have been used. Application of Fourier transform with a low-pass filter (LPF) [52] can remove the unwanted pattern; however, overlapping frequencies of the moiré and grid patterns cause poor quality of the extracted moiré patterns. The Stationary Wavelet Transform (SWT) was used for noise suppression [121] without excessive blurring of important image

30

details; however, the method was only successful in removing straight grid lines. SWT was unable to remove curved lines, especially those with higher curvature at greater depth gradient. Increasing the decomposition level can improve grid removal, but at the cost of excessive image blurring and degradation of the moiré contours.

To improve the ability of the wavelet transform to remove curved grid lines from the generated phase-shifted images, a combination of wavelet and Fourier transforms [122] is newly used here for grid removal. In this wavelet-Fourier technique, wavelet coefficients are dampened by multiplying the Fourier transform of the wavelet coefficients by a Gaussian function $g(x, y)$:

$$g(x, y) = 1 - e^{-\frac{x^2}{2\sigma^2}}, \qquad (3.5)$$

where the value of damping factor σ is based on the amount of grid line deviation from a straight line. The damping coefficient is applied only to the wavelet coefficients that contain the relevant grid line information. The grid removal technique based on combined wavelet and Fourier transform are detailed in Chapter 4. Once the unwanted high frequency periodic grid pattern is removed from the phase shifted images, the extracted moiré patterns (Fig. 3.1c) can be used for phase-shift analysis to compute phase.

3.4 Phase-shift analysis

To compute the object surface height from the generated moiré patterns, the phase information must first be calculated. From Eqs. 3.1 and 3.2, by subtracting I_1 from I_2 and dividing by 2, the coefficient $a(x, y)$ can be removed and the computed phase thus becomes independent of the background intensity.

$$I'_0(x, y) = \frac{I_2(x, y) - I_1(x, y)}{2} = b(x, y)\sin(\Phi(x, y)) \ . \qquad (3.6)$$

From Eqs. 3.3 and 3.4, for the third and fourth frames:

$$I'_\delta(x, y) = \frac{I_4(x, y) - I_3(x, y)}{2} = b(x, y)\sin(\Phi(x, y) + \delta). \qquad (3.7)$$

Finally by solving Eqs. 3.6 and 3.7 simultaneously, the phase can be calculated as follows:

$$\Phi(x, y) = \arctan \frac{I_0'(x, y)\sin\delta}{I_\delta'(x, y) - I_0'(x, y)\cos\delta} \ . \tag{3.8}$$

Eq.3.8 implies that the computed phase is independent of the background $a(x, y)$ and modulation intensities $b(x, y)$. Because of the arctan function, the computed phase (Fig. 3.1d) is wrapped in the range $\left[-\pi, +\pi\right]$ and can be unwrapped by applying a 2D phase unwrapping technique [36].

3.5 System calibration

The main purpose of system calibration (Fig. 3.1e) is to determine the phase-to-height mapping that will be used during height (depth) reconstruction for object shape measurement. The relationship between the computed unwrapped phase φ and object height h depends on the system-geometry parameters and can be expressed as follows [24]:

$$h(x, y) = K\varphi(x, y) . \tag{3.9}$$

In this research, the moiré wavelength can implicitly represent system geometry parameters [55], and was therefore used in system calibration. In this approach, there is no need to compute the unwrapped phase φ during the entire system calibration. The coefficient K in Eq. 3.9 is a function of the moiré wavelength λ :

$$K = \frac{\lambda}{2\pi}, \tag{3.10}$$

where, the moiré wavelength λ is defined as the distance between two successive bright or dark fringes of a moiré pattern on a flat plate, and is determined as follows. A plate is mounted on a translation stage and moved toward the camera-projector plane to several known positions (Fig. 3.1e). At each position, the same grid pattern used during object measurement is projected onto the plate and an image is captured by a camera. The translation should be performed over the full depth of the object of interest. The capture of multiple frames is only required during system calibration, and not during object measurement.

32

For each plate position, a computer-generated grid pattern, of the same pitch as in the captured frame, is digitally superimposed onto the captured image to generate a moiré pattern. Each moiré pattern has a phase shift relative to the previous frame due to plate translation toward the camera-projector plane. The generated frames (for all positions) are filtered by the wavelet-Fourier method to remove the high frequency grid and extract pure moiré patterns.

The moiré pattern at each position is then used to obtain the moiré wavelength λ. The intensity at a single pixel is tracked across all plate positions, seen as red nodes in Fig. 3.2. For any pixel, the moiré fringe intensities across plate positions follow a near-sinusoidal function of the plate translation. The moiré wavelength λ can be estimated by the distance between two successive maxima (bright fringes) or two successive minima (dark fringes), respectively. A coarse measurement of the object height is possible using this estimated moiré wavelength.

It is common to assume that λ is constant between successive moiré fringes [55]. However, the moiré wavelength decreases with increasing calibration depth. This means that during object measurement, the value of the moiré wavelength would vary for different object heights. The determination of the moiré wavelength as a function of height should therefore be included in the calibration process, to allow refinement of the height reconstruction later during object measurement.
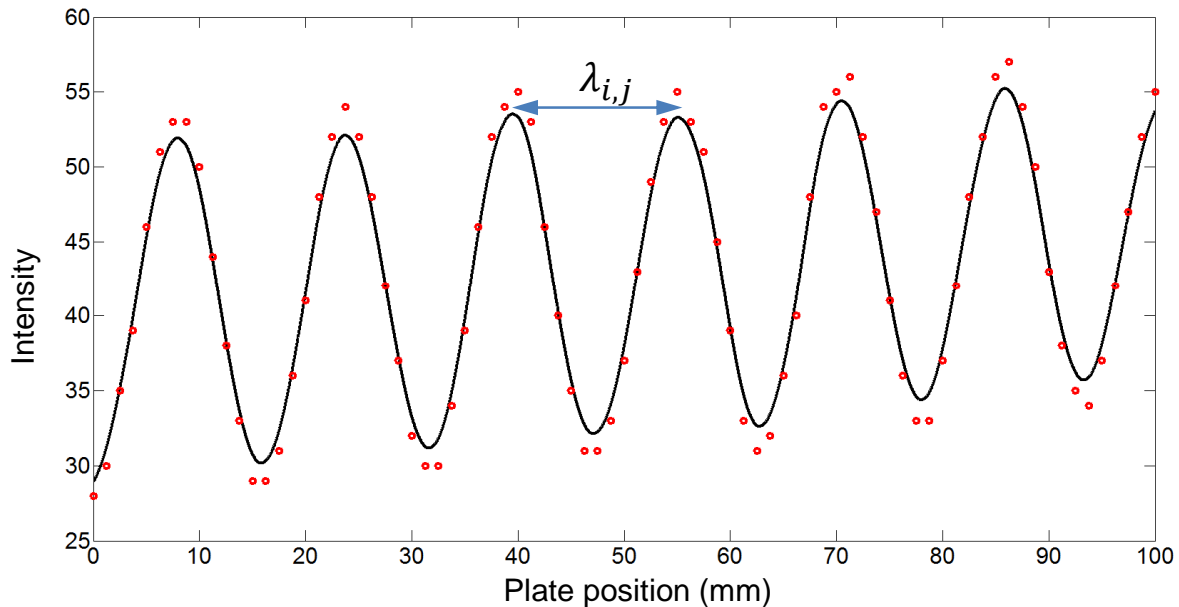
Figure 3.2. Intensity variation across different plate positions at arbitrary pixel j during calibration, showing six peaks and moiré-wavelength shown at $\lambda_{3,j}$.

For each pixel $j=1,2,\ldots n$, where j is the pixel index, and n is the total number of pixels in an image, the intensities are tracked over plate positions and a multi-quadric approximation function is fitted to the intensity-position nodes (Fig. 3.2). The moiré wavelength $\lambda_{i,j}$ is computed at each pair of successive peaks (where $i=1,2\ldots m\text{-}1$ is the peak number, and m is the number of successive peaks), for all pixels. The average moiré wavelength over all pixels $\bar{\lambda}_i$ is then computed at the different peak pairs corresponding to different positions (heights).

$$\bar{\lambda}_i(h) = \frac{1}{n}\sum_{j=1}^{n}\lambda_{i,j}(h) \ . \tag{3.11}$$

Finally, the moiré wavelength as a function of height is approximated by a line fit to all $\bar{\lambda}_i(h)$, $i=1,2\ldots m\text{-}1$.

The entire process to determine the moiré wavelength as a function of height $\lambda(h)$ is summarized as follows:

1) Project grid pattern onto plate.

2) Translate plate toward camera-projector plane to several known positions.

For each plate position:

   3) Capture frame and overlay synthetic grid on each captured frame to generate moiré pattern (containing grid).

   4) Remove high frequency grid to extract pure moiré pattern from each generated frame.

For each pixel:

   5) Track pixel intensities over all plate positions.

   6) Fit an approximation function to the intensity-position nodes extracted in Step 5.

   7) Compute moiré wavelength at each pair of m successive peaks of fitted function.

8) Average extracted moiré wavelength in Step 7 over all pixels, at different peak pairs corresponding to different plate positions, yielding $\bar{\lambda}_i(h)$.

9) Determine moiré wavelength as a function of height $\lambda(h)$ by fitting a line to all $\bar{\lambda}_i(h)$ computed in Step 8.

Once $\lambda(h)$ is determined by the above process, the phase-to-height mapping is completed:

$$h(x, y) = \frac{\lambda(h)}{2\pi} \varphi(x, y) \ . \tag{3.12}$$

The developed system calibration only performs phase-to-height mapping (depth, Z axis), and thus requires separate X-Y plane calibration. An object with known geometry (WxL, width x length) in the X-Y plane is used to perform X-Y plane calibration. The mapping of pixel coordinates to real world coordinates is computed by:

$$P_x = \frac{W}{N_x}, \quad P_y = \frac{L}{N_y}. \tag{3.13}$$

where, N_x and N_y are the number of pixels in the captured image corresponding to the true width W and length L of the object of known geometry, and (P_x, P_y) are the scaling parameters, respectively. The real world coordinates of an object surface in the X-Y plane, (X_o, Y_o), are calculated as $X_o = x \, P_x$ and, $Y_o = y \, P_y$, where (x, y) are the image coordinates. The reference plate images, used in phase-to-height mapping, are also used for the X-Y plane calibration.

3.6 Height computation from phase using pixel-wise moiré-wavelength refinement

For object shape reconstruction, the phase-to-height mapping (Eq.3.12), determined during calibration (Section 3.5), is used to obtain an estimate of the object height distribution. A more accurate height distribution is then computed after refinement of the moiré wavelength using the wavelength-height relation explained below. The entire height computation procedure in Steps I-III below, is performed during object measurement using the moiré wavelength as a function of height $\lambda(h)$, determined in Step 9 of Section 3.5. $\varphi(x, y)$ in Eqs. 3.14-3.16 below, is the unwrapped phase difference between the object and a reference plane. A flat region in the only frame captured during the single-frame object measurement can be used as the reference plane.

I.   Estimate the object height distribution by:

$$\tilde{h}_1(x, y) = \frac{\lambda(\frac{H_C}{2})}{2\pi} \varphi(x, y) \ , \tag{3.14}$$

where H_C is the entire calibration depth (over which calibration is performed).

II.   a) Determine the maximum object height $\tilde{h}_{1\,max}$ over all pixels.

b) Refine the object height by:

$$\tilde{h}_2(x,y) = \frac{\lambda(\dfrac{\tilde{h}_{1\,max}}{2})}{2\pi}\varphi(x,y)\ .$$ (3.15)

III.   a) Perform pixel-wise moiré-wavelength refinement: $\lambda\big(\tilde{h}_2(x,y)\big)$.

b) Perform pixel-wise object height refinement by:

$$h(x,y) = \frac{\lambda\big(\tilde{h}_2(x,y)\big)}{2\pi}\varphi(x,y)\ .$$ (3.16)

In Step III, the moiré-wavelength refinement is performed pixel-wise because the object height will vary across pixels. There is no further iteration beyond Step III, once the height computation is performed pixel-wise (Eq. 3.16).

3.7 Experiments and results

3.7.1 Experimental setup

To demonstrate the method of single-frame digital phase-shifting shape measurement using pixel-wise moiré-wavelength refinement, experiments were performed using an optical setup consisting of a LCD projector (Panasonic PT-AE7000U), monochrome CCD camera (Basler avA1000-100gm) with 1024 x 1024 resolution, with approximately 11 deg camera-projector angle, and 2.5 m camera-projector-plane to object distance (Fig. 3.3).
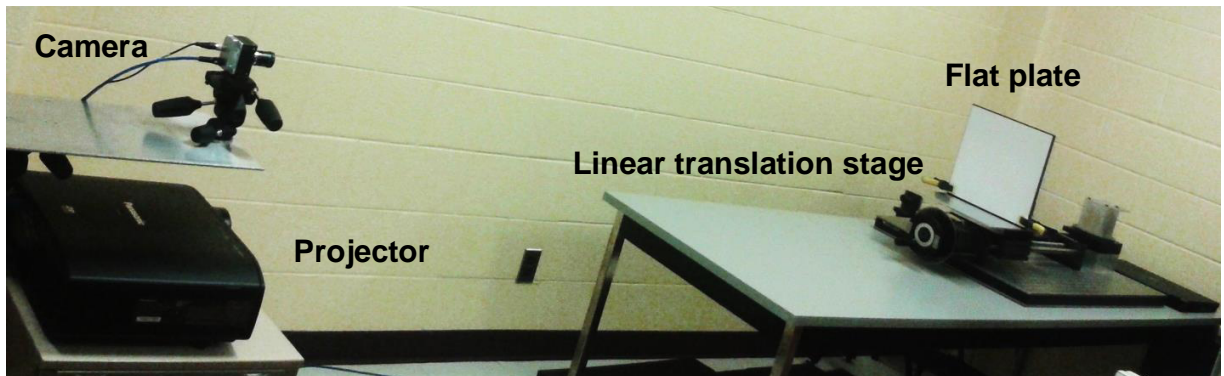
Figure 3.3. Optical setup in single-frame digital phase-shifting moiré.

3.7.2 Calibration

Calibration was performed as in Section 3.5 using a flat plate, mounted on a linear translation stage and translated to 81 positions in 1.25 mm increments over a 100 mm calibration depth with 0.007 mm translation precision. The grid in all captured frames had a 6-pixel pitch. Extraction of moiré patterns by high frequency grid removal employed the wavelet-Fourier transform with Daubechies wavelets (*DB30*), three decomposition levels, and damping factor $\sigma = 15$.

The resulting captured frame of the binary grid projected onto the plate, the generated moiré pattern containing the high frequency grid after superposition of the computer-generated grid on the captured frame, and the moiré pattern extracted by the wavelet-Fourier transform grid removal are shown in Figs. 3.4a-3.4c, respectively. An intensity plot of one column of Fig. 3.4c shows the moiré pattern to be nearly sinusoidal (Fig. 3.4d). The moiré patterns, phase shifted due to plate translation toward the camera-projector plane, are shown in Fig. 3.5 after grid removal, for five sample positions of 81 positions.

| (a) | (b) | (c) | (d) |
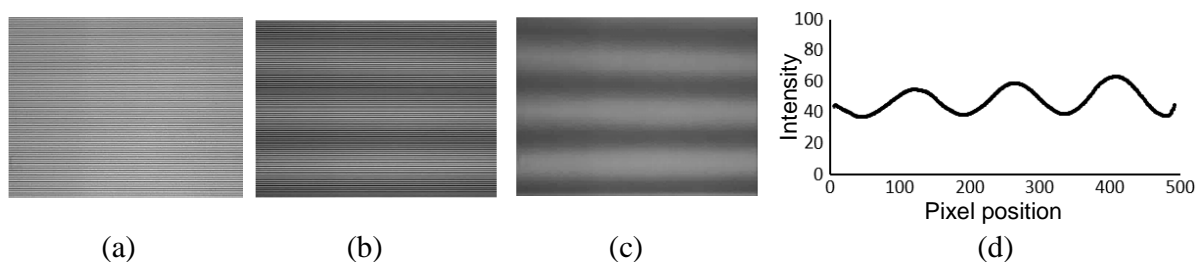
Figure 3.4. Generation of moiré pattern during calibration: a) captured frame of binary grid projected onto plate, b) generated moiré pattern image containing high frequency grid, c) moiré pattern extracted by wavelet-Fourier transform grid removal, and d) intensities along middle column of image in (c).

| (a) | (b) | (c) | (d) | (e) |
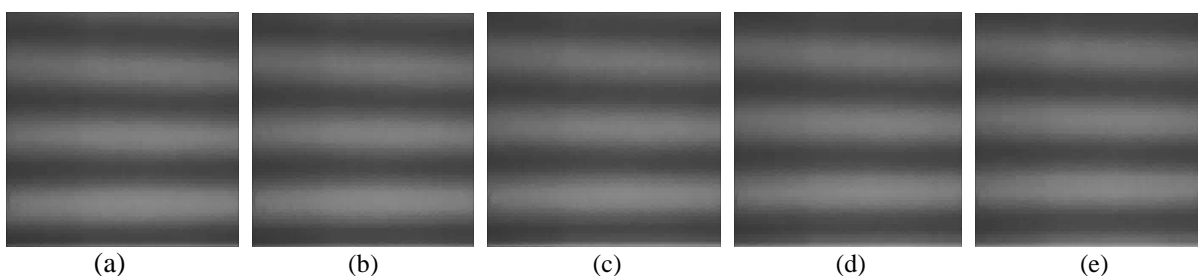
Figure 3.5. Phase shifted moiré patterns due to plate translation to known positions with shifts: a) 0, b) 1.25 mm, c) 2.5 mm, d) 3.75 mm, e) 5 mm.

The tracking of pixel intensities over 81 plate positions produced six peaks, from which five $\bar{\lambda}_i(h)$ were computed (Fig. 3.2). The moiré-wavelength function of height (plate position) approximated by fitting a line to the five $\bar{\lambda}_i(h)$ is shown in Fig. 3.6. The moiré wavelength varies from 15.2 to 16 mm, over the calibration depth of 100 mm, indicating the potential benefit of pixel-wise wavelength refinement (using this wavelength-height function) when performing a measurement.
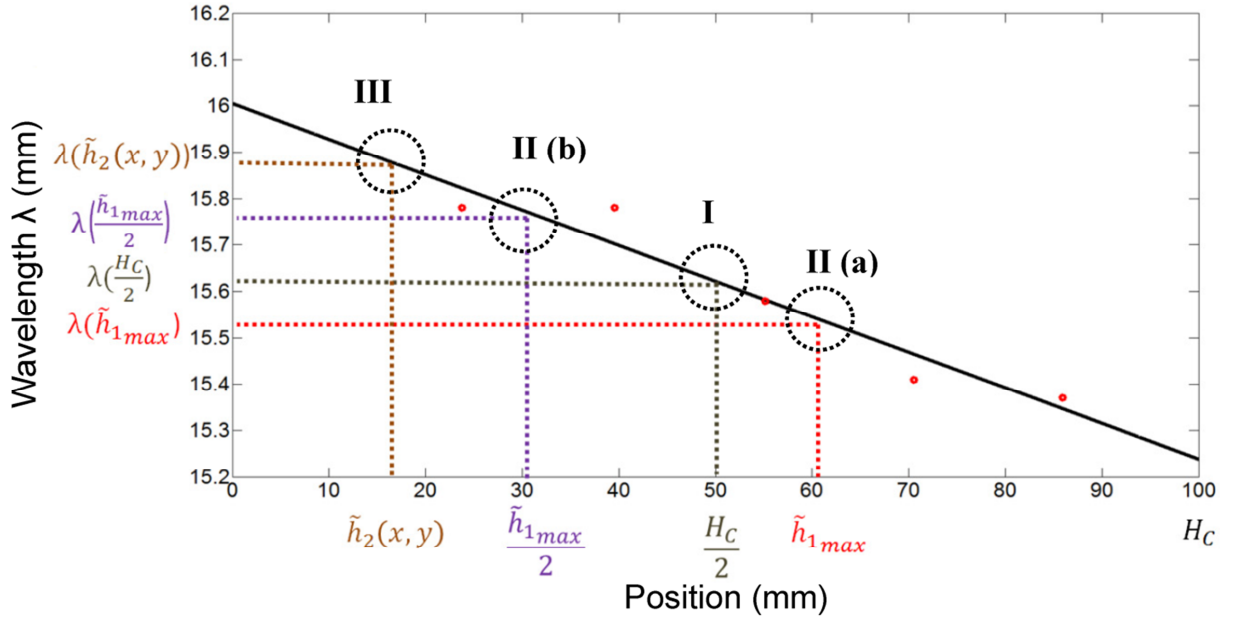
Figure 3.6. Moiré-wavelength function of height (plate position) approximated by fitting line to five $\bar{\lambda}_i(h)$ (seen as nodes), for wavelength and object height refinement.

3.7.3 Measurement

For all object measurements, a single grid pattern (with the same pitch used in the calibration) was projected onto the object and only a single frame was captured. The computer-generated grid pattern of the same pitch (6 pixels) as the captured frame was digitally superimposed and shifted to generate four phase-shifted images with $\delta_1 = 0$, $\delta_2 = \pi$, $\delta_3 = 2\pi/6$, $\delta_4 = 2\pi/6 + \pi$, respectively. The high-frequency grid removal was performed using the same parameters as in the calibration above. The phase calculation and height computation from phase using pixel-wise moiré-wavelength refinement were performed as in Sections 3.4 and 3.6, respectively.

The single-frame digital phase-shifting shape measurement with pixel-wise moiré-wavelength refinement was performed on a flat plate at multiple positions, a hemispherical object, and a manikin head. All measurement results are presented with no filtering or smoothing at any stage.

The flat plate was measured at depths of 5 to 30 mm from an initial position in increments of 5 mm. For each plate position, computation was performed of the mean depth ($\bar{d} = \frac{1}{N}\sum_{k=1}^{N} d_k$), over all measured points (all pixels), standard deviation (SD) of the measured depth $SD = \sqrt{\frac{1}{N}\sum_{k=1}^{N}(d_k - \bar{d})^2}$, and root-mean-square error (RMSE) (over all pixels)

$$RMSE = \sqrt{\frac{1}{N}\sum_{k=1}^{N}(d_k - D)^2} \ , \tag{3.17}$$

where d_k is the perpendicular distance between a measured point and a plane fitted to all measured points in the initial position; D is the true depth (height), determined from the translation stage; and N is the total number of measured points.

The RMSE in measurement of the flat plate at Steps I, II, III (Section 3.6) (Fig. 3. 7) of the pixel-wise moiré wavelength and height refinement show improvement in measurement accuracy at each step. The ranges of RMSE were 0.334 to 0.828 mm at Step I, 0.199 to 0.360 mm at Step II, and 0.204 to 0.261 mm at Step III of the measurement. Improvement in measurement accuracy was generally seen at each step, with the best improvements of 0.567 mm from Steps I to III at plate position 30 mm and 0.156 mm from Steps II to III at plate position 25 mm.
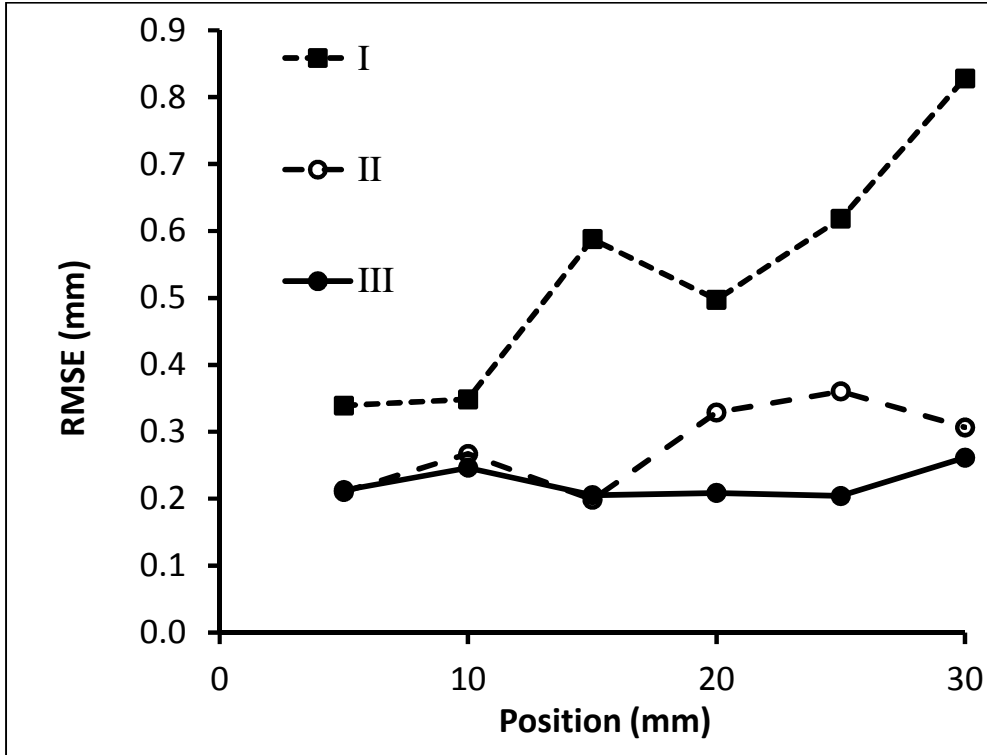
Figure 3.7. RMSE in measurement of a flat plate at known positions, using the new single-frame digital phase-shifting moiré method, at Steps I, II, III (Section 3.6) of the pixel-wise moiré wavelength and height refinement.

These improvements demonstrate the benefit of the pixel-wise moiré wavelength and height refinement using $\lambda\left(\tilde{h}_2(x,y)\right)$ in Step III, compared to using half the maximum object height in Step II, and half the calibration depth in Step I. Details of the measurement accuracy are given in Table 3.1 for the final refinement (Step III). The developed single frame method achieved RMSE of 0.20 to 0.26 mm, and mean plate depth measurement accuracies within 0.15 mm at a 2.5 m camera to object standoff distance.

Table 3.1. Mean depth (height), SD, and RMSE in measurement of a flat plate at known positions.

True depth ±0.007(mm)	5.000	10.000	15.000	20.000	25.000	30.000
Mean depth (mm)	4.915	10.096	14.933	20.114	25.045	29.850
SD (mm)	0.195	0.226	0.194	0.174	0.199	0.222
RMSE (mm)	0.213	0.246	0.205	0.209	0.204	0.261

40

The hemispherical object was measured by projecting the same grid pattern as for the plate. The single captured frame and four generated phase-shifted moiré frames are shown in Figs. 3.8a-3.8e. The computed wrapped and unwrapped phase maps and 3D measured surface represented as a point cloud are illustrated in Fig. 3.9. A least-squares fitted sphere to the measured points had a radius of 50.93 mm compared to the true radius 50.80 mm, and thus an error of 0.13 mm, with sphere fitting SD 0.37 mm. The hemisphere measurement RMSE (based on differences between radius of measured points and true radius) was 0.39 mm. A sample cross-section of measured points with the true semicircle (Fig. 3.10), demonstrate the effectiveness of the proposed single-frame measurement method. The measured points are close to the true values for most of the surface. As commonly occurring, larger errors are seen near the edge of the surface, where the camera and projector optical axes are nearly parallel to the surface.

(a)   (b)   (c)   (d)   (e)
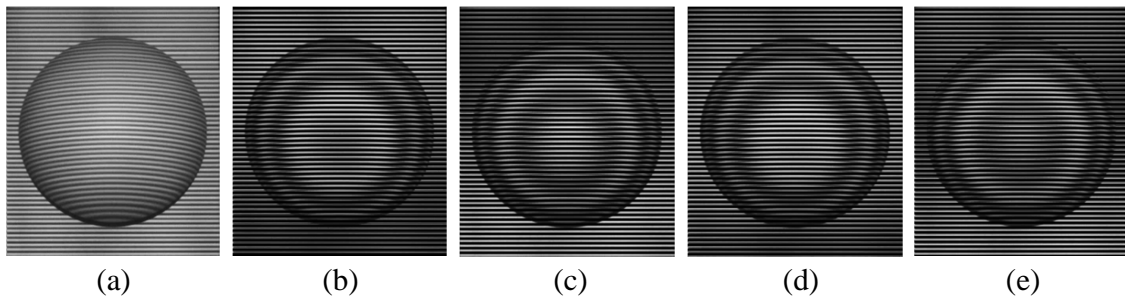
Figure 3.8. Hemispherical object measurement: a) single captured frame, and b-e) four generated phase-shifted moiré frames with $\delta = 0$, $\delta = \pi$, $\delta = 2\pi/6$, and $\delta = 2\pi/6 + \pi$, respectively.

(a)   (b)   (c)
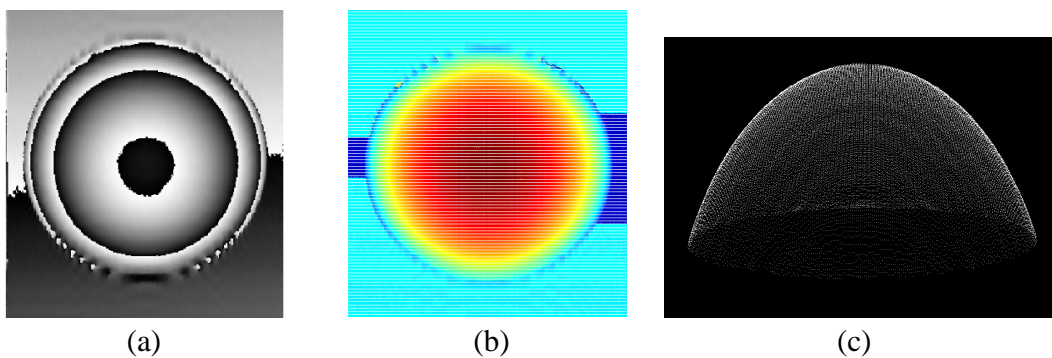
Figure 3.9. Hemispherical object measurement: a) wrapped phase map b) unwrapped phase map (c) 3D measured surface as point cloud.
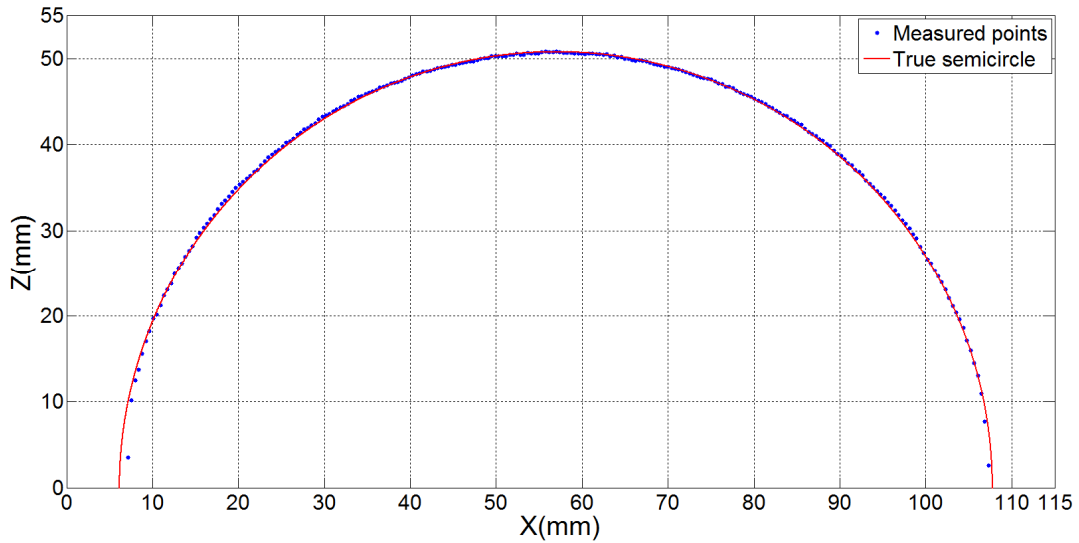
Figure 3.10. Sample cross-section of measured points of hemisphere and true semicircle.

The manikin head was measured by the single-frame measurement method using the same grid pattern as for the plate and hemisphere. A single captured frame of the projected grid on the object surface, a sample generated moiré pattern containing the high frequency grid, and four phase-shifted moiré patterns after grid removal are shown in Fig. 3.11. The computed wrapped and unwrapped phase maps and 3D measured surface represented as point clouds are illustrated in Fig. 3.12. The measurement shows the ability of the proposed method to measure surface features of the object.

| (a) | (b) | (c) | (d) | (e) | (f) |
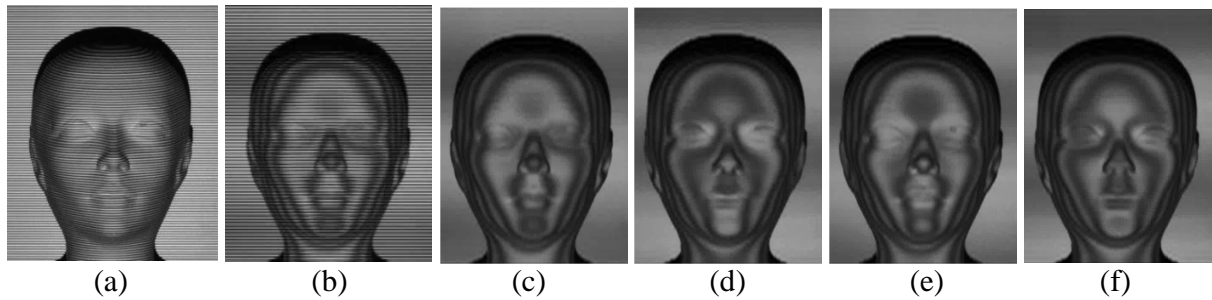
Figure 3.11. Generation of moiré contours on manikin head by digital phase shifting: (a) captured frame of projected grid, b) sample generated moiré pattern containing high frequency grid, c-f) generated phase-shifted moiré patterns after grid removal with $\delta = 0$, $\delta = \pi$, $\delta = 2\pi/6$, and $\delta = 2\pi/6 + \pi$, respectively.
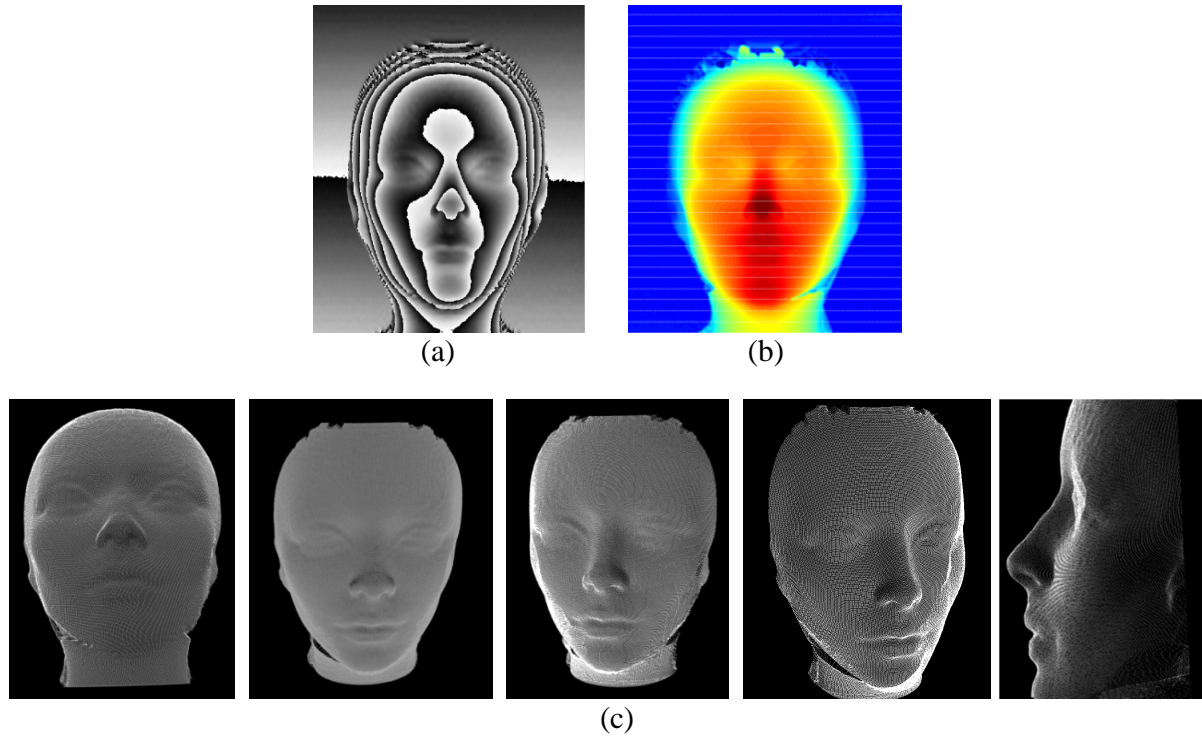
Figure 3.12. 3D measurement of manikin head: (a) wrapped phase (b) unwrapped phase (c) point cloud representations of measured points of the surface.

3.8 Discussion

Direct measurement of optical system parameters in digital moiré, and small range of depth measurement in optical moiré (shadow and projection method) are two main limitations in previous system calibration techniques in moiré profilometry. The moiré-wavelength based phase-to-height mapping method, developed in this thesis for digital moiré, avoids the need for optical-setup parameter measurement and is thus an improvement over previous digital moiré techniques. The computed wavelength-height function takes into account the moiré wavelength variation over calibration depth when measuring an object over extended depth. The novel moiré-wavelength refinement technique, which performs pixel-wise computation of the wavelength based on height (depth), improved measurement accuracy compared to measurement using a single global wavelength across all pixels. The new method was able to measure surface height using only a single captured frame of the object surface with only a single projected grid pattern. The projected pattern was a simple binary grid, which avoids problems associated with gamma nonlinearity.

Chapter 4

Single-frame grid removal in digital moiré

In this chapter, a new single-frame grid removal technique was developed for application in single-frame digital-moiré 3D shape measurement. The ability of the stationary wavelet transform (SWT) to prevent oscillation artifacts near discontinuities, and the ability of the Fourier transform (FFT) applied to wavelet coefficients to separate grid lines from useful image information, were combined in a new technique, SWT-FFT, to remove grid lines from moiré-pattern images generated by digital moiré.

4.1 Digital generation of phase-shifted moiré patterns

In digital-moiré, phase-shifted moiré patterns are generated by firstly projecting a binary grid onto the object surface, using the setup shown in Fig. 4.1, and capturing a single frame (Fig. 4.2a).
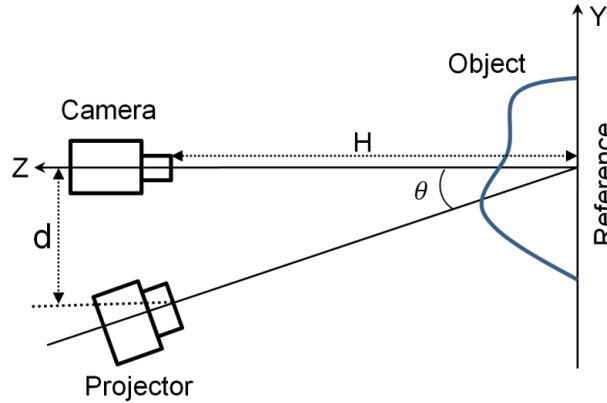
Figure 4.1. Optical setup for digital moiré 3D shape measurement (side view).

The Fourier series expansion of the intensity distribution I_R of the captured image when a horizontal binary grid is projected onto a reference flat plate is given by:

$$I_R\left(x, y\right) = a_0 + \sum_{n=1}^{\infty} a_n \cos(\frac{2\pi n}{p} y), \tag{4.1}$$

where p is the grid pitch, and (x, y) are the image coordinates. The intensity distribution I_O of the captured image when the same binary grid is projected onto an object surface is:

$$I_O\left(x, y\right) = b_0 + \sum_{m=1}^{\infty} b_m \cos(\frac{2\pi m}{p} y + \phi(x, y)), \tag{4.2}$$

44

where $\phi(x, y)$ is the phase distribution which contains object height information:

$$\phi(x, y) = \frac{2\pi}{p}\left(\tan\theta\right)Z(x, y), \tag{4.3}$$

where θ is the angle between the camera and projector and $Z(x, y)$ is the height distribution. Assuming that the object to camera-projector standoff distance H is much bigger than the surface height, $H \gg Z(x, y)$, the relation between the phase and object height is linear:

$$\phi(x, y) = \frac{2\pi}{p}(\frac{d}{H})Z(x, y). \tag{4.4}$$

Eq. (4.2) can be rewritten as:

$$I_{\mathrm{O}}(x, y) = b_0 + \sum_{m=1}^{\infty} b_m \cos(\frac{2\pi m}{p}y + \frac{2\pi d\, Z(x, y)}{pH}). \tag{4.5}$$

Moiré patterns are generated digitally in a post-process, by first producing a synthetic grid I_{S} with the same pitch (period) as the captured frame on the flat plate,

$$I_{\mathrm{S}}(x, y) = a_0 + \sum_{n=1}^{\infty} a_n \cos(\frac{2\pi n}{p}y). \tag{4.6}$$

The synthetic grid I_{S} is then superimposed over the captured image of the deformed grid on the object surface, I_{O}. The resultant transmission function I_{M} upon superimposition is given by the product of I_{S} and I_{O}.

$$
\begin{aligned}
I_{\mathrm{M}} &= (a_0 + \sum_{n=1}^{\infty} a_n \cos(\frac{2\pi n}{p}y))(b_0 + \sum_{m=1}^{\infty} b_m \cos(\frac{2\pi m}{p}y + \frac{2\pi d\, z(x, y)}{pH})) \\
I_{\mathrm{M}} &= a_0 b_0 + a_0 \sum_{m=1}^{\infty} b_m \cos(\frac{2\pi m}{p}y + \frac{2\pi d\, z(x, y)}{pH}) + b_0 \sum_{n=1}^{\infty} a_n \cos(\frac{2\pi n}{p}y) \\
&+ \sum_{n=1}^{\infty}\sum_{m=1}^{\infty} a_n b_m \cos(\frac{2\pi n}{p}y)\cos(\frac{2\pi m}{p}y + \frac{2\pi d\, z(x, y)}{pH}).
\end{aligned}
\tag{4.7}
$$

The first term of the product $a_0 b_0$ is the background intensity, and the second and third terms are the deformed and straight grids, respectively. The fourth term represents moiré patterns that can be expressed as:

$$
\begin{aligned}
&\frac{1}{2}\sum_{n=1}^{\infty}\sum_{m=1}^{\infty} a_n b_m \cos(\frac{2\pi n}{p}y + \frac{2\pi m}{p}y + \frac{2\pi dZ(x, y)}{pH}) \\
&+ \frac{1}{2}\sum_{n=1}^{\infty}\sum_{m=1}^{\infty} a_n b_m \cos(\frac{2\pi n}{p}y - \frac{2\pi m}{p}y - \frac{2\pi dZ(x, y)}{pH}).
\end{aligned}
\tag{4.8}
$$

45

The first and second terms in Eq. (4.8) represent the constructive and destructive interference, respectively, of the captured deformed grid and straight synthetic grid. The constructive and destructive interference generate bright and dark fringes of the moiré pattern, respectively (Fig. 4.2b).

In order to extract phase information from moiré patterns to compute height, phase shift analysis [24] can be used with at least three phase-shifted moiré patterns. To generate phase-shifted moiré patterns (Fig. 4.2c), digital translation of the synthetic grid by δ_k, a fraction of the grid pitch, is performed by:

$$I_S^K (x, y) = a_0 + \sum_{n=1}^{\infty} a_n \cos(\frac{2\pi n}{p}(y + \delta_k)), \qquad (4.9)$$

where $\delta_k = p((k-1)/j)$, I_S^K is the synthetic grid for the kth shift ($k=1,...,j$) ,and j is the number of phase shifts. In comparison to optical moiré [26, 29], the amount of phase shift in digital moiré is independent of the system geometry parameters and object height. The generated phase-shifted moiré images in Eq. 4.7, contain useful moiré contours (fourth term) with encoded surface-height information, as well as unwanted high-frequency deformed and undeformed grid lines (the second and third terms).
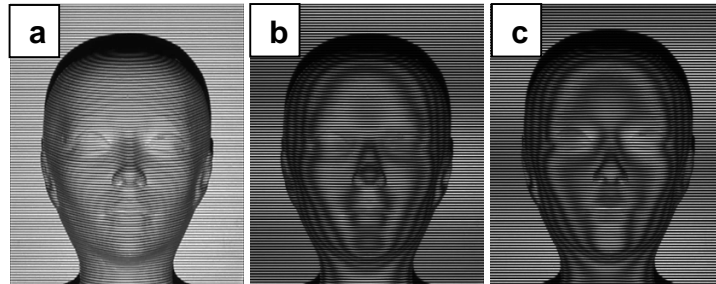
Figure 4.2. Generation of moiré contours on manikin head by digital phase shifting: (a) single captured frame of projected grid, b) generated moiré pattern containing high frequency grid, c) generated phase-shifted moiré pattern with π phase shift respect to (b) containing high frequency grid.

This grid lines must be removed without degradation of the moiré patterns to allow accurate phase extraction from the moiré patterns for object height calculation. The grid removal technique must be single-frame, to maintain the entire method single-frame.

4.2 Grid removal

The Fourier transform has been used in grid removal for moiré patterns; however, it has been found to blur and smear the fine moiré patterns and introduce artifacts in the de-noised images [52]. The wavelet transform has been successful in removing the undeformed (straight) lines; however, it is unable to remove the highly curved deformed lines. A successful single-frame grid removal technique should completely eliminate the highly curved grid lines without blurring and smearing the moiré patterns and without introducing artifacts in the de-noised image.

The stationary wavelet transform (SWT) [123] has the shift-invariant property, which suppresses pseudo-Gibbs oscillations near discontinuities such as edges when performing noise reduction. A 2D wavelet transform of an image $I(x, y)$ with MxN dimensions yields four coefficients: approximation coefficient cA_L, and horizontal cD_l^H, vertical cD_l^V and diagonal cD_l^D, detail coefficients. The image can thus be decomposed into four sub-bands and expressed by [20]:

$$I(x, y) = \sum_M \sum_N cA_L \, \Phi_L(x, y) + \sum_{l=1}^{L} \sum_M \sum_N cD_l^H \, \Psi_{H,l}(x, y)$$

$$+ \sum_{l=1}^{L} \sum_M \sum_N cD_l^V \, \Psi_{V,l}(x, y) + \sum_{l=1}^{L} \sum_M \sum_N cD_l^D \, \Psi_{D,l}(x, y), \qquad (4.10)$$

where $\Phi_L(x, y)$ is the scaling function, $\Psi_{H,l}$, $\Psi_{V,l}$, and $\Psi_{D,l}$ are wavelet functions, and L is the decomposition level. The approximation coefficient can be iteratively decomposed at each level, while the horizontal, vertical and diagonal detail coefficients will remain unchanged. In applying SWT, there is no coefficient decimation at each decomposition level that occurs with other wavelet methods. Thus, the size of all coefficients is equal to the size of the analyzed image for all decomposition levels. At each decomposition level, the scaling function is the low frequency component of the previous scaling function. The wavelet function is related to the order of applying filters. Since the wavelet transform is separable, scaling and wavelet functions can be written as follows:

$$
\begin{aligned}
\Phi(x, y) &= \Phi(x)\Phi(y), \\
\Psi_H(x, y) &= \Psi(x)\Phi(y), \\
\Psi_V(x, y) &= \Phi(x)\Psi(y), \\
\Psi_D(x, y) &= \Psi(x)\Psi(y),
\end{aligned}
\tag{4.11}
$$

where Φ and Ψ are signals with low-pass and high-pass frequency spectra, respectively (Fig. 4.3). Daubechies wavelets [124] are the most commonly used mother wavelets for image denoising and are classified by their number of zero moments or vanishing moments (zero crossings of wavelet). The wavelets with fewer vanishing moments smooth less, preserve more detail, and are therefore preferred for image denoising. Wavelets with more vanishing moments cause more smoothing and produce border distortions, and are therefore less preferred for image denoising. Scaling and wavelet functions for two Daubechies mother wavelets are shown in Fig. 4.4, where the number of vanishing moments for the scaling functions $db5$ and $db12$, are 5 and 12 respectively.
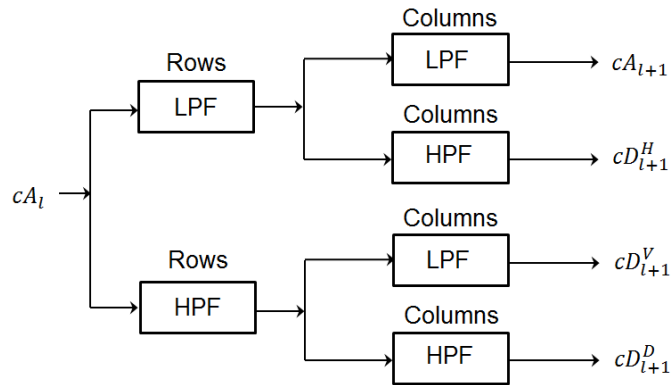
Figure 4.3. Decomposition of image using Stationary Wavelet Transform (LPF: Low-pass filter, HPF: High-pass filter).
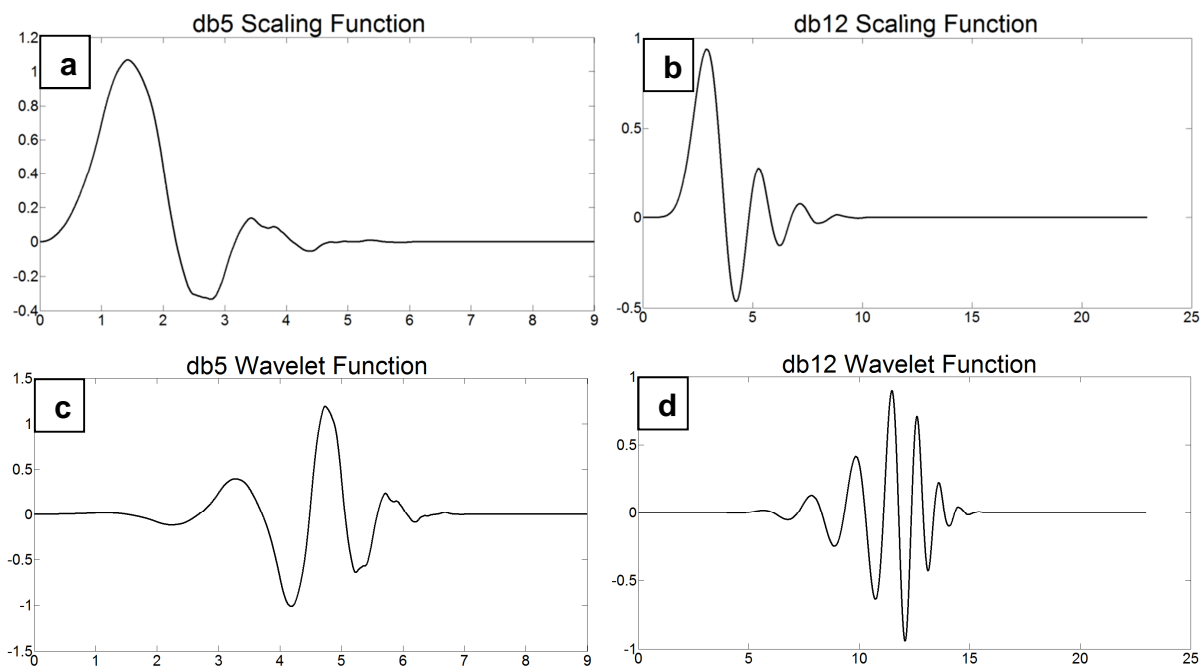
Figure 4.4. Scaling and wavelet functions of two different Daubechies wavelets: scaling functions: a) *db*5, b) *db*12; wavelet functions: c) *db*5, d) *db*12.

Applying wavelet transform to a noisy image effectively condenses the horizontal grid lines (the second and third terms in Eq. 4.7) to the horizontal detail coefficient (cD_l^H) and approximation coefficient (cA_L) and separates the grid lines from useful image components. The amount of grid information in cD_l^H at each decomposition level depends on the spatial frequency of the captured grid on the object surface, which is directly related to the pitch of grid lines. Removal of thicker grid lines (greater pitch) requires a higher decomposition level than removal of thinner grid lines. For a large and adequate decomposition level, the impact of grid lines on the approximation coefficient (cA_L) will be insignificant. To remove the grid lines, several approaches are possible. Setting all cD_l^H at each decomposition level ($l=1, …, L$) to zero and applying the inverse wavelet transform removes grid lines; however, it also removes useful image information, and thus yields a poor quality de-noised image. Hard thresholding of wavelet coefficients related to the grid introduces artifacts to the reconstructed image, and soft thresholding blurs the reconstructed image [121, 125, 126]. Furthermore, both hard and soft thresholding of SWT coefficients are unable to remove grid lines completely in regions of large changes in depth, where the deformed lines on the object surface have greater curvature.

Increasing the decomposition level to remove highly curved grid lines could improve grid removal, but this would smear the useful moiré pattern information.

To improve the ability of the stationary wavelet transform to remove curved lines without increasing the decomposition level and without smearing the useful moiré contours, a combination of stationary wavelet and Fourier transforms (SWT-FFT) was used. The Fourier transform of the wavelet coefficients provides further grouping of the coefficients into the useful details of the image and the grid lines. Wavelet coefficients are dampened by multiplying the Fourier transform of the wavelet coefficients by a Gaussian function $g(u,v)$ [122]:

$$g(u,v) = 1 - e^{-\frac{u^2}{2\sigma^2}} \, , \qquad\qquad (4.12)$$

where u and v are the horizontal and vertical spatial frequency domain coordinates, respectively, and the value of σ (damping factor) can be selected based on the amount of grid line deviation from a straight line. The damping coefficient is applied only to the wavelet coefficients that contain the grid. Since the generated moiré image (Eq. 4.7) contains only horizontal grid lines, the Fourier transform of the horizontal wavelet coefficient includes high frequency components only in the vertical direction (v-axis) in the frequency domain. Therefore, damping of the Fourier transform of the horizontal coefficients only needs to be performed on the v-axis to remove the grid without losing useful image information (Eq. 4. 12). The other wavelet coefficients, which are not related to grid lines, remain unchanged. After grid-coefficient damping, inverse FFT is performed, and the image with grid lines removed is reconstructed by inverse SWT of the dampened and unchanged coefficients. Applying the above SWT-FFT results in further separation of the grid lines from the useful image information, compared to applying SWT only, and permits easy filtering of the noise in the frequency domain.

The SWT-FFT method has two important parameters, the decomposition level and damping factor. The decomposition level depends on the pitch of the captured grid on the object surface and the damping factor depends on the curvature of the grid. For example, narrow-pitch grids require a low decomposition level to decrease the loss of valid information. Straight grids (undeformed lines) require zero damping ($\sigma = 0$), and the value of damping factor required increases as the curvature of the grid increases from a straight line. The damping factor and decomposition level have to be as small as possible to keep the useful information unchanged, but large enough to remove the high frequency grids.

4.3 Assessment of grid removal performance

While common quantitative image de-noising assessment methods, such as peak signal-to-noise ratio (PSNR) and root-mean-square error (RMSE), require a reference image without noise, and since such an image is not available for the generated moiré images, a reference-free quality metric is required. The roughness index [127] estimates the amount of high spatial frequencies associated with the remaining grid lines in a de-noised image. The roughness index ρ can be expressed as:

$$\rho = \frac{\|h \otimes X\|}{\|X\|} \, ,$$ (4.13)

where X is the output image after grid removal, $\otimes$ is the 2D convolution operator, h is a vertical edge-detector filter, and $\|X\|$ is the l_1 norm of X. A low ρ indicates better grid removal in the output image. It is preferred to use the roughness index and visual inspection together to evaluate different grid removal techniques, since the roughness index cannot detect excessive smoothness and other imperfections (artifacts) in the moiré pattern.

4.4 Experiments and Results

To demonstrate the method of SWT-FFT grid removal in single-frame digital moiré, experiments were performed with the optical setup shown in Fig. 4.1, using a LCD projector, monochrome 1024 x 1024 CCD camera, with 11 deg camera-projector angle and 2.5 m camera-projector to object distance. Digital moiré images were generated by the method of Section 4.1 for three objects: a manikin head, a crowned mask, and a double-faced mask (Fig. 4.5).
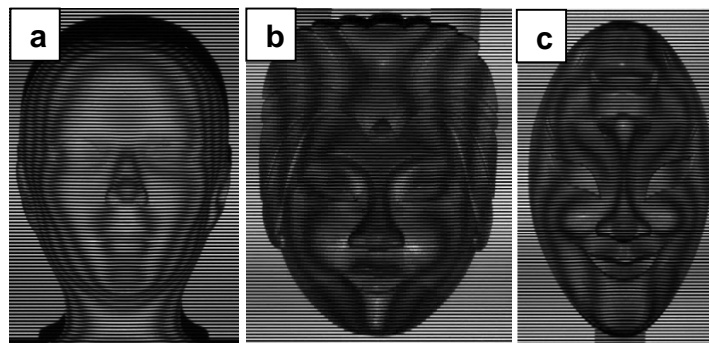
Figure 4.5. Original images with moiré patterns and high-frequency grid lines generated by digital moiré: a) manikin head, b) crowned mask, and c) double-faced mask.

The generated images contain useful moiré patterns with unwanted high frequency grid lines. This grid lines must be removed without degradation of the moiré patterns to allow accurate phase extraction from the moiré patterns for object height calculation. To demonstrate the effectiveness of the SWT-FFT, the method was compared to other single-frame grid-removal techniques using Fourier transform (FFT) and discrete wavelet transform (DWT) separately, as well as combined discrete wavelet and Fourier transform (DWT-FFT).

The Fourier transform using low-pass filtering (LPF) with different bandwidths was applied to the original crowned mask image (Fig. 4.6a). The narrow bandwidth LPF causes blurring of the moiré pattern (Fig. 4.6b) while the wide bandwidth LPF leaves residual grid lines (Fig. 4.6d). The medium bandwidth LPF was found to be the best trade-off between removing the grid lines and preserving the moiré pattern (Fig. 4.6c). However, even using the medium bandwidth, the LPF Fourier transform does not allow complete elimination of the high-frequency grid lines without removing useful fine detail of the moiré-pattern, which should be retained. Furthermore, because FFT is not localized in the spatial domain, artifacts are introduced in the de-noised images.
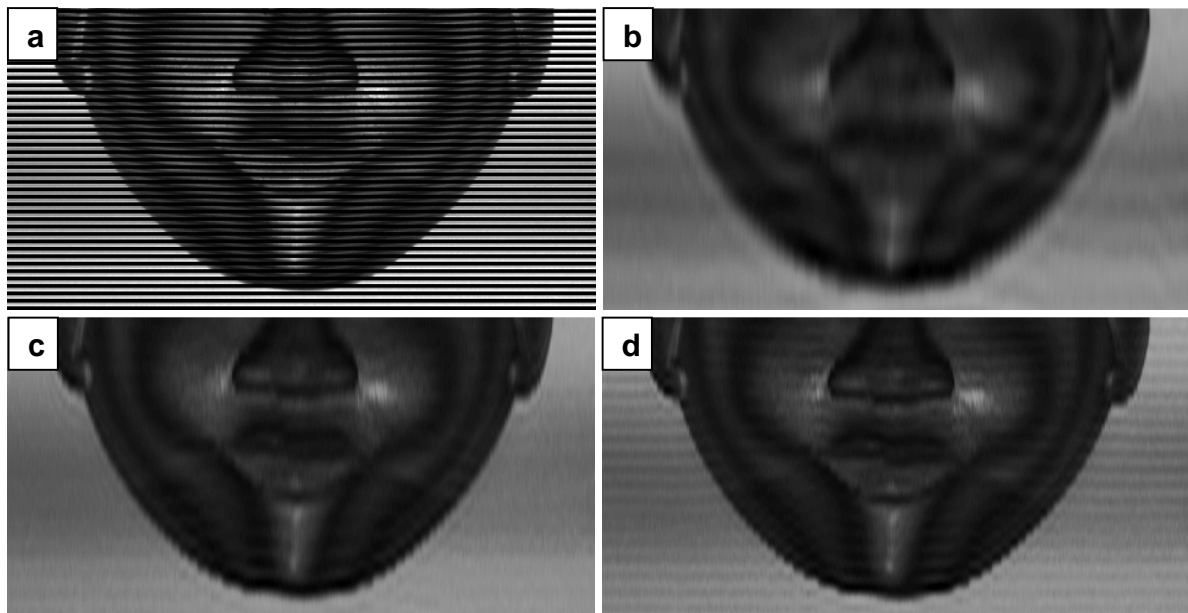
Figure 4.6. Images of the crowned mask zoomed-in on the chin: a) original image containing moiré pattern and grid lines; de-noised images by Fourier transform using low-pass filtering with b) narrow bandwidth, c) medium bandwidth, and d) wide bandwidth.

The discrete wavelet transform (DWT) was used to remove the grid lines and preserve more moiré information than by FFT. The number of vanishing moments in the Daubechies wavelet has to be high enough to remove the grid lines but low enough to prevent artifacts at the borders. In the experiments, Daubechies wavelet *db*12 was used as it was found to be best in preliminary experiments. The crowned mask image containing the moiré pattern and grid lines (Fig. 4.7a) was wavelet decomposed into 2, 3, and 4 levels using Daubechies wavelet *db*12. The results (Fig. 4.7) show that using three decomposition levels (*L*=3) with *db*12 and applying soft-thresholding to the horizontal wavelet coefficients was partly successful in removing grid lines and preserving the moiré pattern (Fig. 4.7c); however, in the bottom chin region, boundary artifacts appear. The lower decomposition level (*L*=2) was unable to remove the grid (Fig. 4.7b) and the higher decomposition level (*L*=4) removed the grid lines but smeared the moiré pattern (Fig. 4.7d). Even for the best case (*L*=3) (Fig. 4.7c), DWT was thus not able to fully remove the highly curved grid lines without smearing the moiré pattern or introducing boundary artifacts.
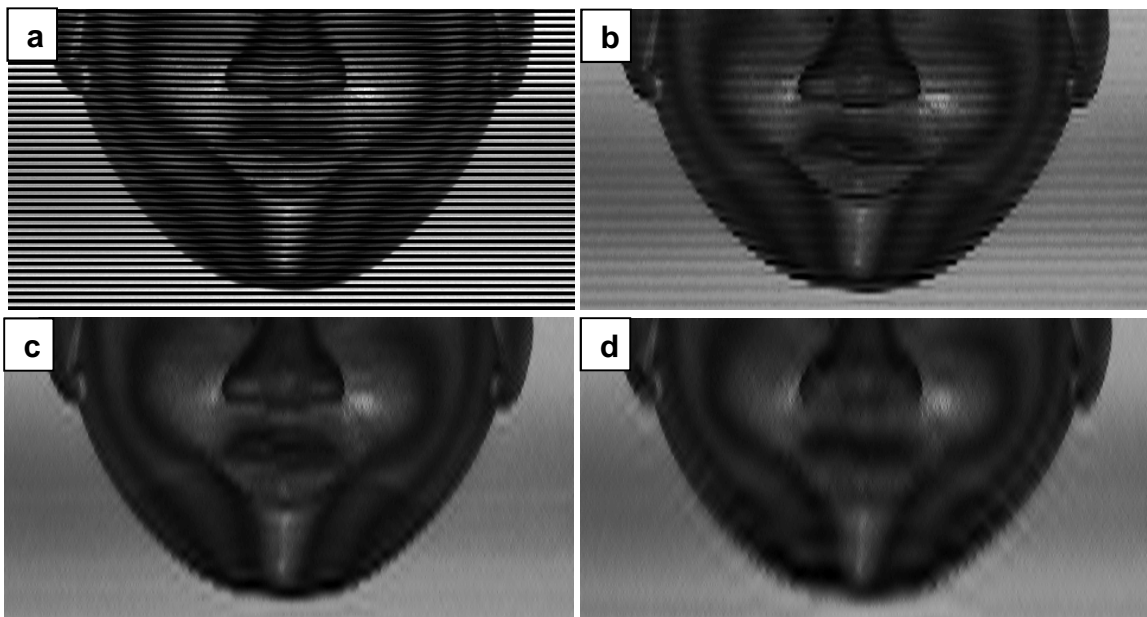
Figure 4.7. Images of the crowned mask zoomed-in on the chin a) original image containing moiré pattern and grid lines; de-noised images by discrete wavelet transform (DWT) (*db*12, soft thresholding) with different decomposition levels (*L*): b) *L*=2, c) *L*=3, and d) *L*=4.

Combined discrete-wavelet and Fourier transforms (DWT-FFT) was used in the current experiments to remove highly curved grid lines without increasing the decomposition level, which tends to smear the moiré pattern. The crowned mask image (Fig. 4.5b) was wavelet

decomposed into three levels (*L*=3) using Daubechies wavelets *db*5, *db*12, *db*24, and *db*45, which have different number of vanishing moments, and damping factor $\sigma = 180$. Image de-noising by *db*5 (Fig. 4.8a) was unable to remove grid lines, while *db*24 (Fig. 4.8c) and *db*45 (Fig. 4.8d) introduced artifacts (stripes in the chin region indicated by the red oval). These artifacts would appear as ripples in the reconstructed surface. Wavelet *db*12 was best in removing the grid lines while preventing artifacts (chin region in Fig. 4.8b). DWT-FFT is able to remove the highly curved grid lines; however, the method introduces boundary artifacts in the de-noised images (Figs. 4.8a-d).
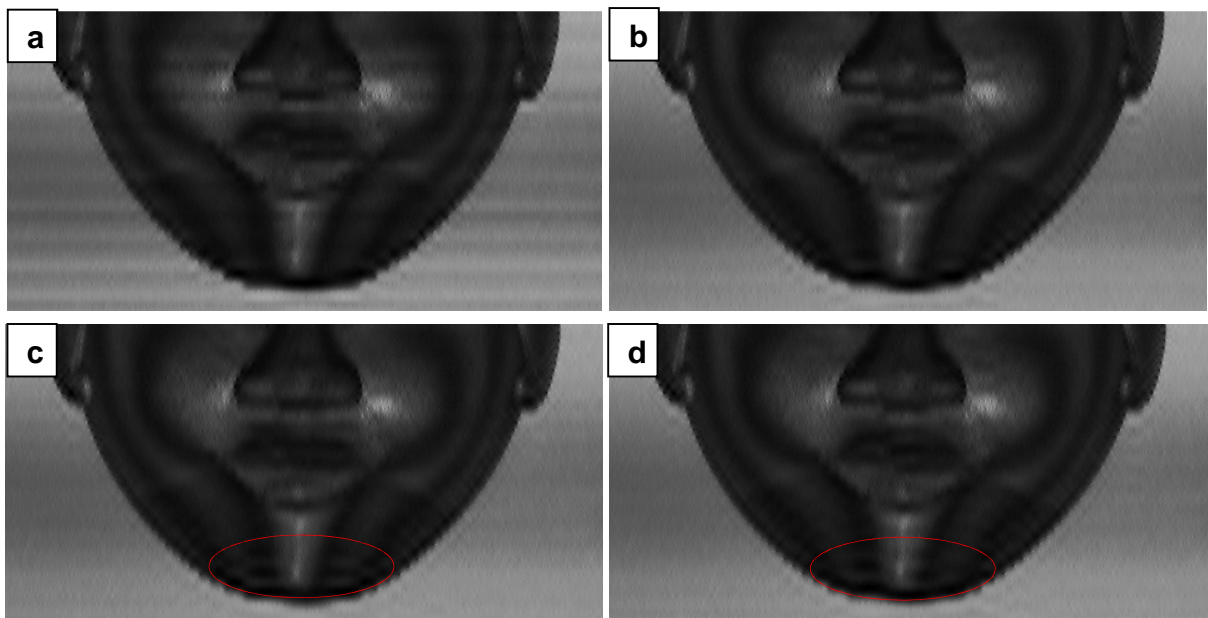
Figure 4.8. Images of the crowned mask zoomed-in on the chin, de-noised by combined discrete wavelet and Fourier transforms (DWT-FFT) using *L*=3, $\sigma = 180$, and Daubechies wavelet with different vanishing moments a) *db*5, b) *db*12, c) *db*24, and d) *db*45.

Combined stationary-wavelet and Fourier transforms (SWT-FFT) was used to remove highly curved grid lines without introducing artifacts in the de-noised image. SWT decomposes images without decimating the wavelet coefficients (decimation would decrease the resolution of the wavelet coefficients). This property allows SWT to suppress oscillation artifacts near discontinuities (including borders) in comparison to DWT. Daubechies wavelet with different vanishing moments *db*2, *db*5, *db*12, *db*24, and *db*45 were applied to the crowned mask (Fig. 4. 5b) using SWT-FFT with three decomposition levels (*L*=3) and damping factor $\sigma = 180$.

Wavelet *db*5 (Fig. 4.9b) was found to be best in removing the grid lines and preventing artifacts. Image de-noising by *db*2 (Fig.4.9a) was unable to remove grid lines everywhere in the image (best seen in the chin region), while a higher number of vanishing moments (*db*12, *db*24 and *db*45) increased artifacts (in the chin region indicated by the red oval) as seen in Figs. 4.9c, 4.9d, and 4.9e, respectively.
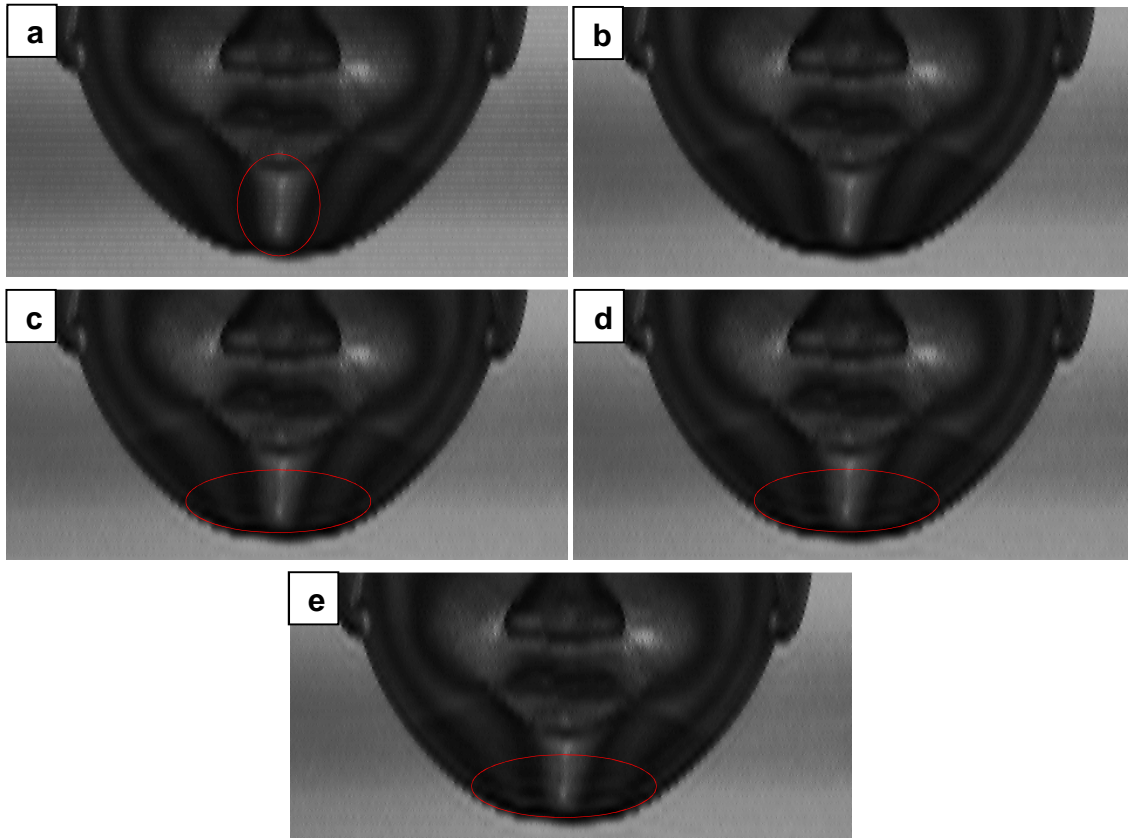
Figure 4.9. Images of the crowned mask zoomed-in on the chin, de-noised by SWT-FFT with $L=3$, $\sigma = 180$ and Daubechies wavelet with different vanishing moments a) *db*2, b) *db*5, c) *db*12, d) *db*24, and e) *db*45.

SWT allows the use of Daubechies wavelet *db*5, which has a low number of vanishing moments, to suppress smoothing and distortion in the de-noised image in comparison to DWT (*db*12). This property would decrease ripples in the reconstructed surface. To determine the damping factor σ, a coarse-to-fine approach was used, starting at $\sigma = 50$ and increment of 50 until moiré-contour loss occurred in the de-noised image. Finer increments of 30 were then used to finalize the damping factor, to best remove the deformed and undeformed grid lines without

moiré-contour loss. Different damping factors $\sigma = 50, 100, 180$ with decomposition levels $L= 3$ applied to the crowned mask image (Fig. 4.5b) with SWT-FFT are shown in Fig. 4.10. Damping factor $\sigma = 180$ achieved the best compromise between grid removal and preservation of the moiré pattern (Fig. 4.10c). Lower damping factors $\sigma = 50, 100$ were unable to completely remove the grid lines (Figs. 4.10a, 4.10b).
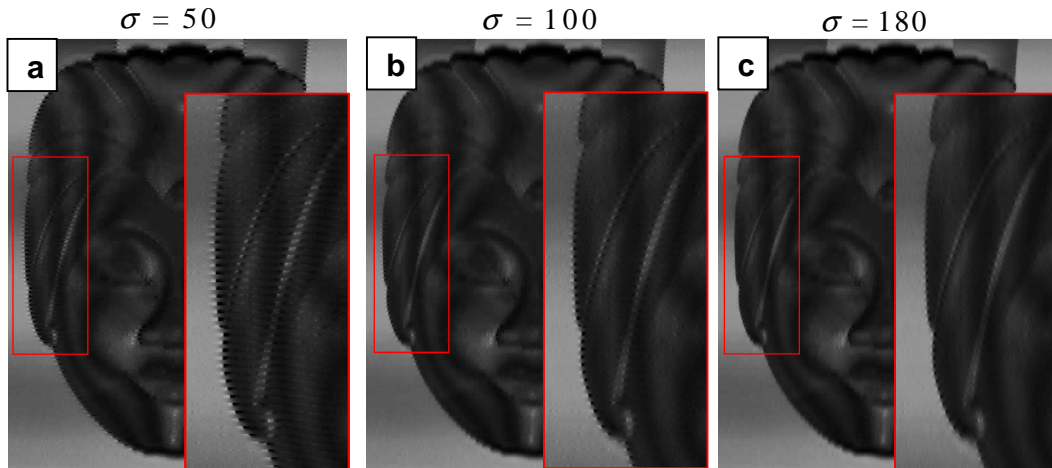
Figure 4.10. Images of the crowned mask with zoomed-in region indicated by red rectangle, de-noised by SWT-FFT (*db*5) using decomposition level *L*=3 and damping factors a) $\sigma = 50$, b) $\sigma = 100$, c) $\sigma = 180$.

To compare the performance of SWT-FFT in grid removal to FFT, DWT, and DWT-FFT methods, de-noised images and wrapped phase maps, zoomed-in on the chin, and object heights calculated by digital-moiré 3D reconstruction are shown for the manikin head (Fig. 4.11), crowned mask (Fig. 4.12), and double-faced mask (Fig. 4.13). The best parameters of each method found earlier, were used in the comparison: FFT with medium bandwidth LPF; DWT with *db*12, *L*=3, and soft thresholding; DWT-FFT with *db*12, *L*=3, and $\sigma = 380$ for manikin head and $\sigma = 180$ for crowned and doubled-faced masks; and SWT-FFT with *db*5, *L*=3, and $\sigma = 380$ for manikin head and $\sigma = 180$ for crowned and doubled-faced masks. A higher damping factor, $\sigma = 380$, was used for the manikin head, compared to $\sigma = 180$ for the crowned and double-faced masks, because of the higher grid-line curvature that occurs in the manikin head due to greater height gradients.

For FFT (Fig. 4.11a), in addition to introducing artifacts, blurring of the moiré pattern occurred with grid removal for the manikin head. For DWT (Fig. 4.11b) and DWT-FFT (Fig. 4.11c), artifacts were introduced because of the decimation of the wavelet coefficients at each

56

decomposition level. The comparison between de-noised images shows that SWT-FFT (Fig. 4.11d) is best in removing the grid lines (straight and curved) without introducing artifacts.

The advantage of SWT-FFT compared to FFT, DWT, and DWT-FFT methods can be seen even more clearly in the wrapped phase maps zoomed-in on the manikin head chin (Figs. 4.11e-4.11h). The artifacts near the large height gradients are seen for FFT (Fig. 4.11e), and appear more prominently as ripples for DWT (Fig. 4.11f), and DWT-FFT (Fig. 4.11g) in the regions indicated by red ovals. For SWT-FFT (Fig. 4.11h) smaller artifacts occur, and they appear only at the outer boundary, indicating more accurate phase extraction (Figs. 4.11h) with SWT-FFT.

The advantage of SWT-FFT compared to FFT, DWT, and DWT-FFT methods can be also clearly seen for the object heights calculated from the wrapped phase map by single-frame digital-moiré 3D measurement (detailed in Chapter 3). Cross-sections of calculated heights are shown in Figs. 4.11i-4.11l, for the middle column of the manikin head image. The calculated heights after de-noising the phase-shifted moiré images by FFT (Fig. 4.11i), DWT (Fig. 4.11j), and DWT-FFT (Fig. 4.11k), were noisy in the regions indicated by the red ovals (I, II, III, IV) with noise amplitude (height measurement error) 0.20, 0.18, 0.12, 0.24 mm for FFT (Fig. 4.11i), 0.23, 0.20, 0.17, 0.21 mm for DWT (Fig. 4.11j), and 0.21, 0.25, 0.15, 0.20 mm for DWT-FFT (Fig. 4.11k), respectively. SWT-FFT (Fig. 4.11l) yielded the best height reconstruction with minimal noise, 0.06, 0.08, 0.11, 0.10 mm for the same regions. In comparison to the other methods, for example in region II, the noise amplitude for SWT-FFT was approximately 0.10, 0.12, and 0.17 mm lower than for FFT, DWT, and DWT-FFT, respectively.
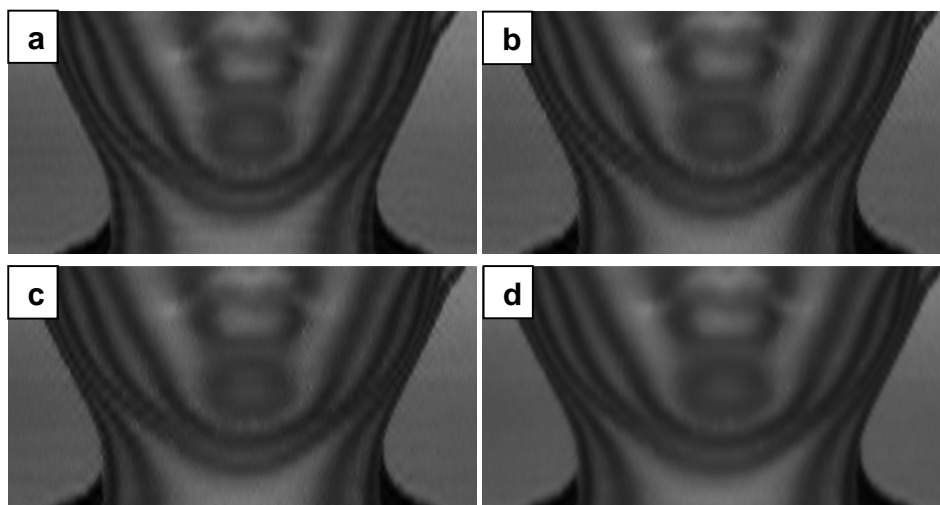
Figure 4.11. Performance comparison of grid removal techniques for manikin head: a-d) images of manikin head (zoomed-in on chin); e-h) wrapped phase maps (zoomed-in on chin); i-l) height for middle cross-section of object (middle image column); after applying: a, e, i) FFT with medium bandwidth LPF; b, f, j) DWT with *db*12*, L*=3, soft thresholding; c, g, k) DWT-FFT with *db*12, *L*=3, $\sigma = 380$; and d, h, l) SWT-FFT with *db*5, *L*=3, $\sigma = 380$.

For the crowned-mask, FFT (Fig. 4.12a) again caused image blurring and FFT (Fig. 4.12a), DWT (Fig. 4.12b) and DWT-FFT (Fig. 4.12c) caused artifacts seen as stripes on the chin in the de-noised images. SWT-FFT (Fig. 4.12d) was best in removing grid lines without stripe artifacts. Boundary artifacts occurred for all de-noised images (Fig. 4.12a-d), but was least for SWT-FFT (Fig. 4.12d). In the wrapped phase maps, artifacts in de-noised images appear as ripples (regions

indicated by red ovals) for FFT (Figs. 4.12e), DWT (Fig. 4.12f) and DWT-FFT (Fig. 4.12g). For FFT (Figs. 4.12e), the stripe artifacts are most noticeable as ripples on the chin. SWT-FFT (Fig. 4.12h) had smallest artifacts in the wrapped phase map. The advantage of SWT-FFT can be most clearly seen for the object heights. The heights calculated from de-noised images by FFT (Fig. 4.12i), DWT (Fig. 4.12j), and DWT-FFT (Fig. 4.12k), were noisy especially in the regions indicated by the red ovals. For example, the noise amplitude in the chin region (pixels 535-590) was 0.72 mm for FFT (Fig. 4.12i), 0.55 mm for DWT (Fig. 4.12j), and 0.60 mm for DWT-FFT (Fig. 4.12k). SWT-FFT (Fig. 4.12l) yielded the best height reconstruction with noise amplitude 0.23 mm in the same region. In the chin region, the noise amplitude for SWT-FFT was approximately 0.49, 0.32, and 0.37 mm lower than for FFT, DWT, and DWT-FFT, respectively.
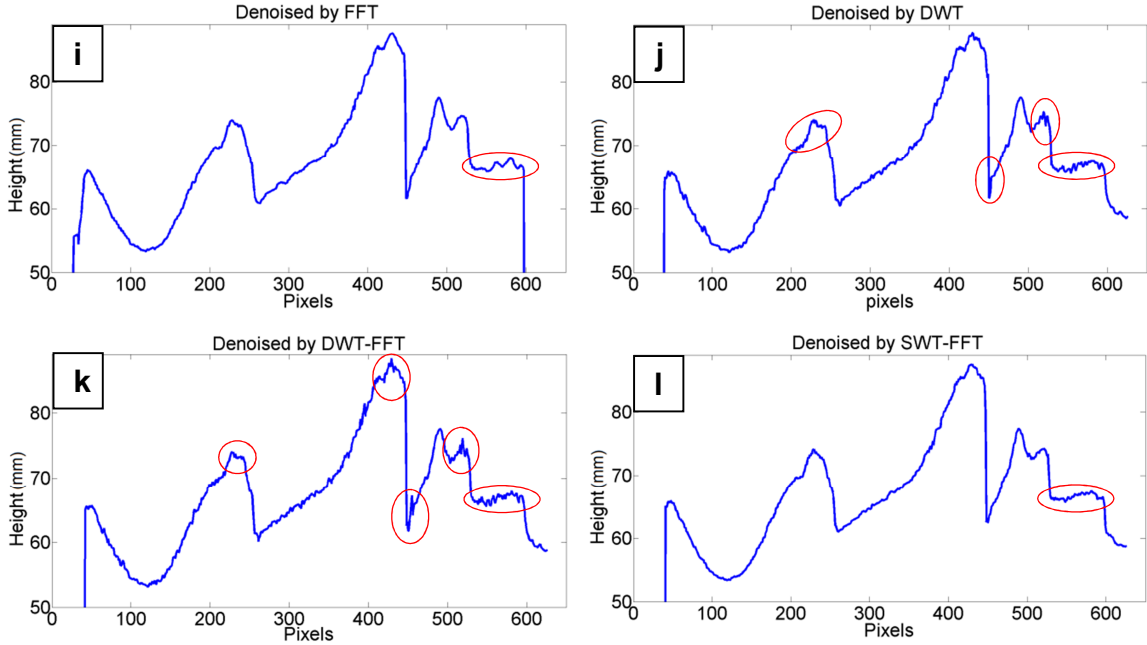
Figure 4.12. Performance comparison of grid removal techniques for crowned mask: a-d) images of crowned mask (zoomed-in on chin); e-h) wrapped phase maps (zoomed-in on chin); i-l) height for middle cross-section of object (middle image column); after applying: a, e, i) FFT with medium bandwidth LPF; b, f, j) DWT with *db*12*, L*=3, soft thresholding; c, g, k) DWT-FFT with *db*12, *L*=3, $\sigma = 180$; and d, h, l) SWT-FFT with *db*5, *L*=3, $\sigma = 180$.

For the double-faced mask, artifacts can be seen as stripes on the chin, most prominent for FFT (Fig. 4.13a), but also for DWT (Fig. 4.13b), and DWT-FFT (Fig. 4.13c). SWT-FFT (Fig. 4.13d) was best in removing grid lines without stripe artifacts. Boundary artifacts occurred for all de-noised images (Fig. 4.13a-d), but was least for SWT-FFT (Fig. 4.13d). In the wrapped phase maps, artifacts in de-noised images appears as ripples (regions indicated by red ovals), most prominent for FFT (Figs. 4.13e), smaller for DWT (Fig. 4.13f) and DWT-FFT (Fig. 4.13g), and smallest for SWT-FFT (Fig. 4.13h). The advantage of SWT-FFT can be also clearly seen for the object heights. The heights calculated from de-noised images by FFT (Fig. 4.13i), DWT (Fig. 4.13j), and DWT-FFT (Fig. 4.13k), were noisy especially in the regions indicated by the red ovals. For example, the noise amplitude in the chin region (pixels 565-595) was 0.65 mm for FFT (Fig. 4.13i), 0.16 mm for DWT (Fig. 4.13j), and 0.18 mm for DWT-FFT (Fig. 4.13k). SWT-FFT (Fig. 4.13l) yielded the best height reconstruction with noise amplitude 0.06 mm in the same region. In the chin region, the noise amplitude for SWT-FFT was approximately 0.59, 0.10, and 0.12 mm lower than for FFT, DWT, and DWT-FFT, respectively.
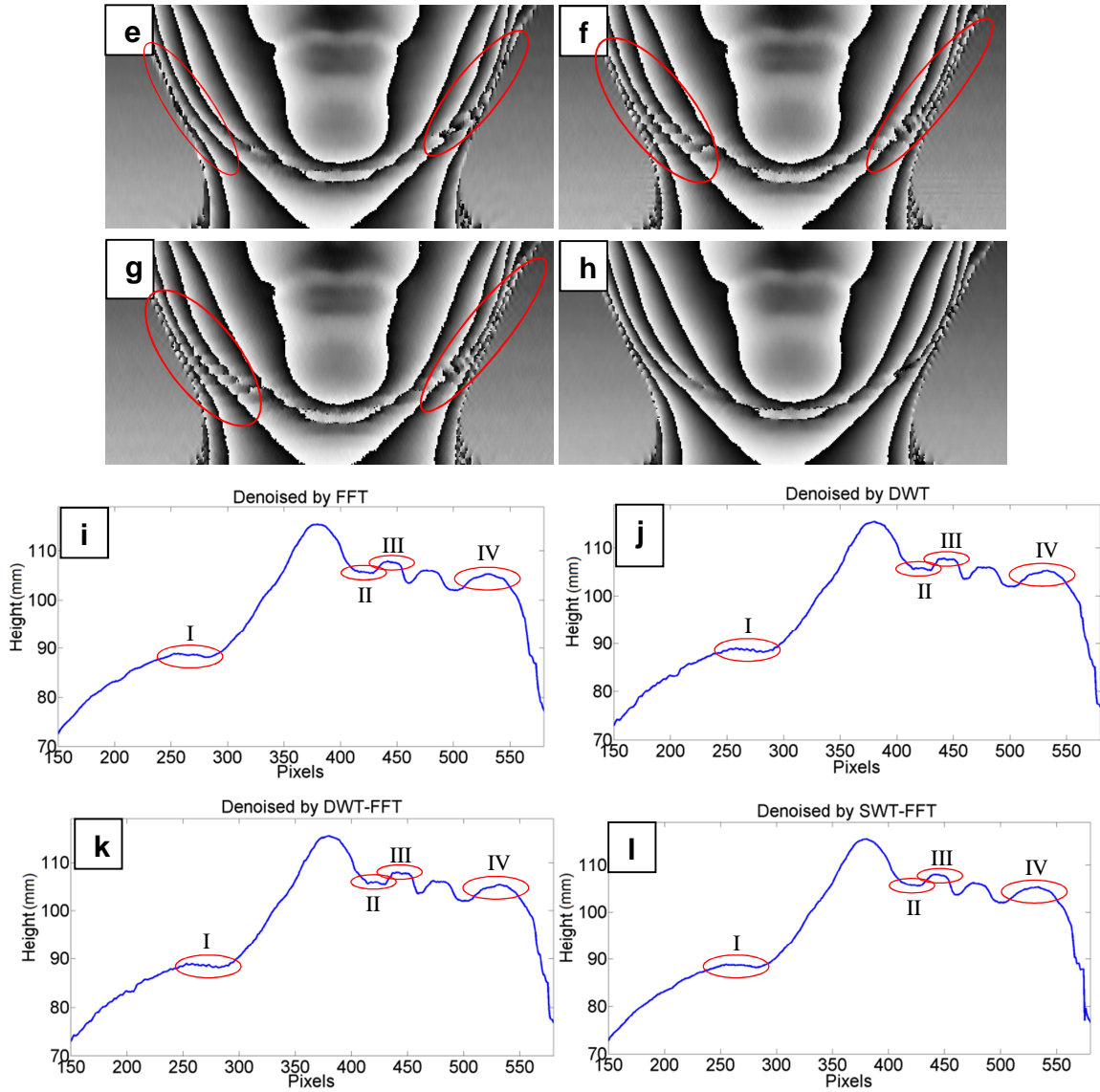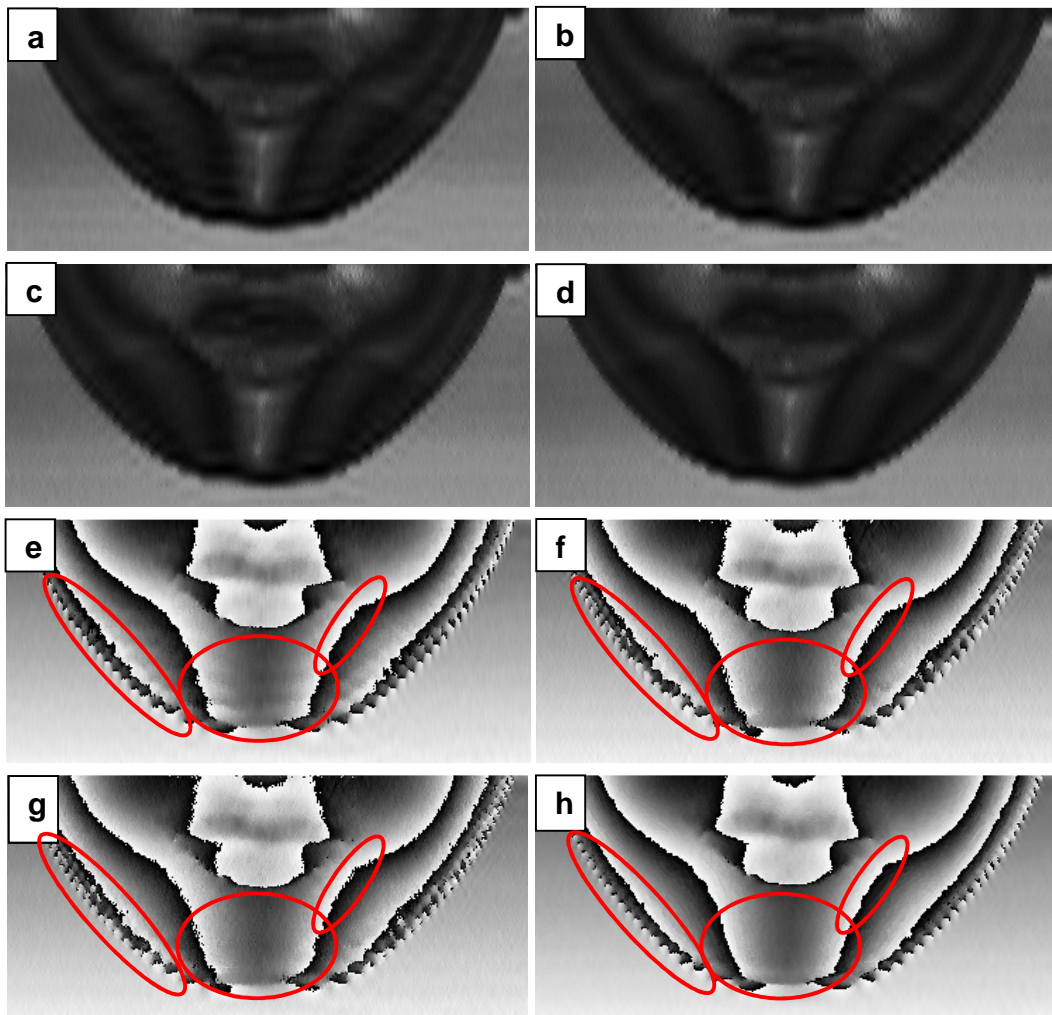
60
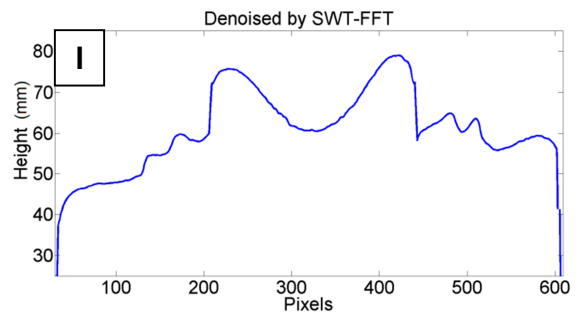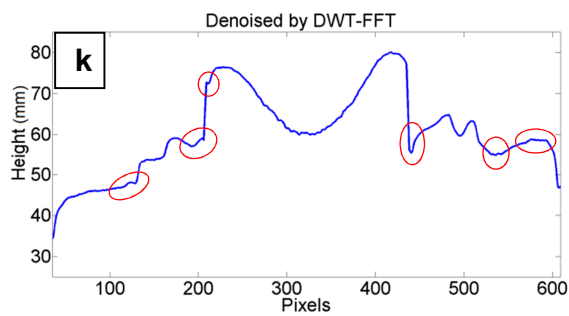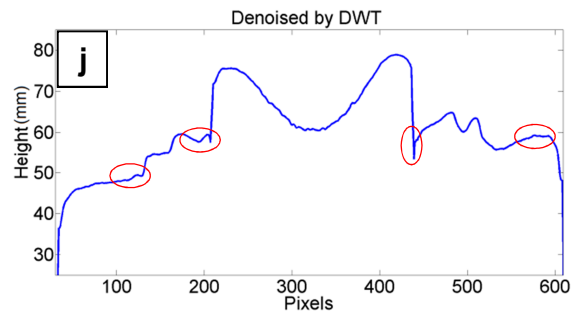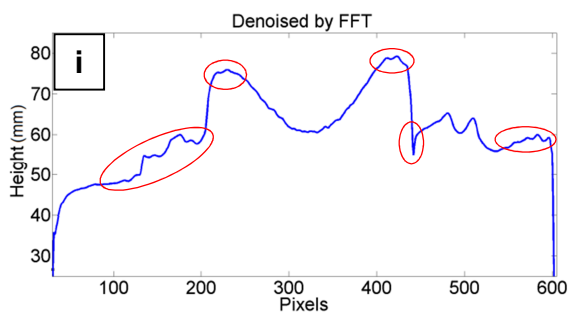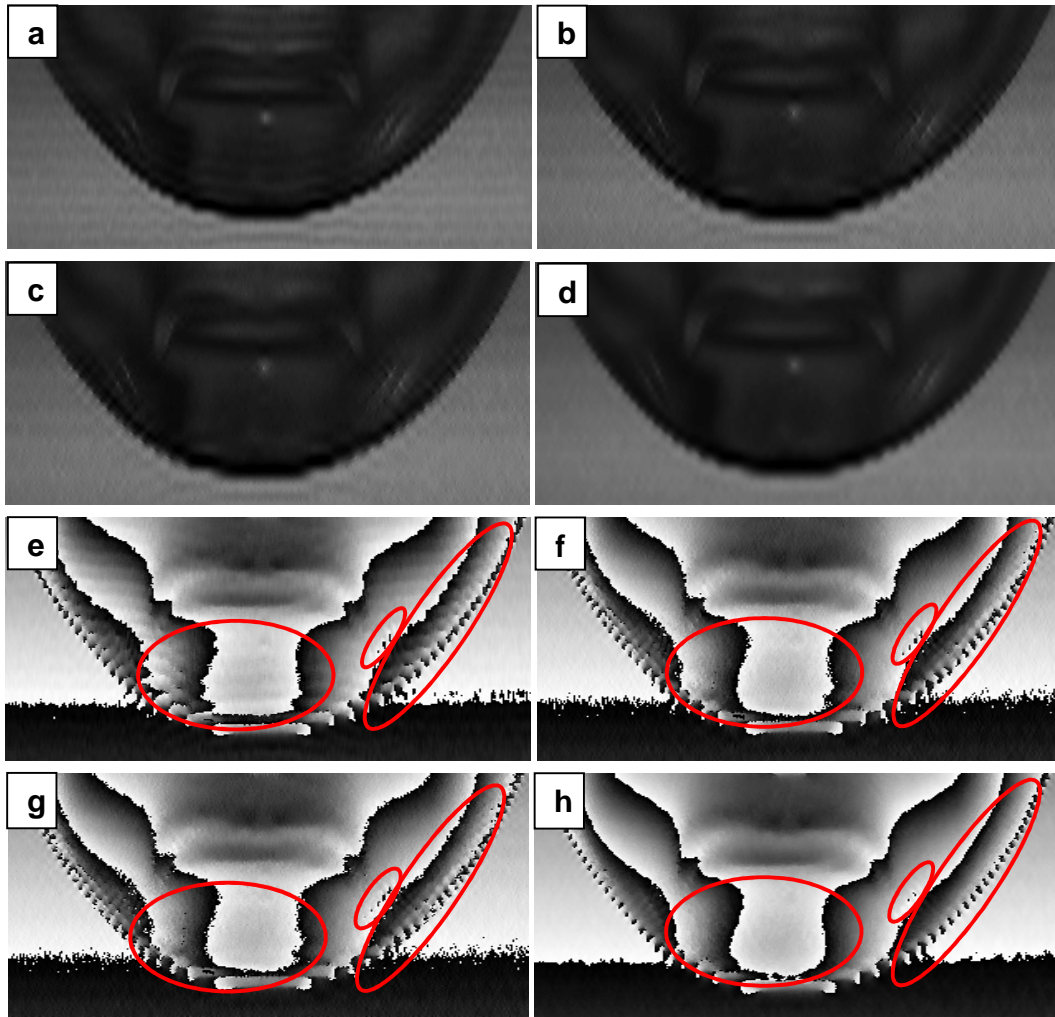
Figure 4.13. Performance comparison of grid removal techniques for double-faced mask: a-d) images of double-faced mask (zoomed-in on chin); e-h) wrapped phase maps (zoomed-in on chin); i-l) height for middle cross-section of object (middle image column); after applying: a, e, i) FFT with medium bandwidth LPF; b, f, j) DWT with *db*12, *L*=3, soft thresholding; c, g, k) DWT-FFT with *db*12, *L*=3, $\sigma = 180$; and d, h, l) SWT-FFT with *db*5, *L*=3, $\sigma = 180$.

SWT-FFT was the most effective in removing the unwanted grid lines and preserving the moiré pattern compared to FFT, DWT, and DWT-FFT. The de-noising ability of SWT-FFT allowed phase extraction and height computation with least noise. The effective performance of SWT-FFT is evident in the raw point-cloud representations of the surfaces shown in Fig. 4.14.

Assessment using the roughness index was also carried out to compare the grid removal ability of FFT, DWT, DWT-FFT, and SWT-FFT. The lowest roughness index and thus best performance over all tests for each object (Table 4.1) was for the de-noised images using SWT-FFT. Although the roughness index is low for de-noised images using other techniques, the low values occur at the cost of introducing artifacts and excessive blurring and degradation of useful image information (the moiré pattern) which is not detectible by the roughness index.

Table 4.1. Roughness index for original images without grid-removal and de-noised images using FFT, DWT, DWT-FFT, and SWT-FFT.

	Roughness index				
	Original	FFT	DWT	DWT-FFT	SWT-FFT
Manikin head	1.471	0.039	0.038	0.037	0.035
Crowned Mask	1.514	0.031	0.033	0.030	0.027
Double-faced mask	1.491	0.041	0.038	0.035	0.031
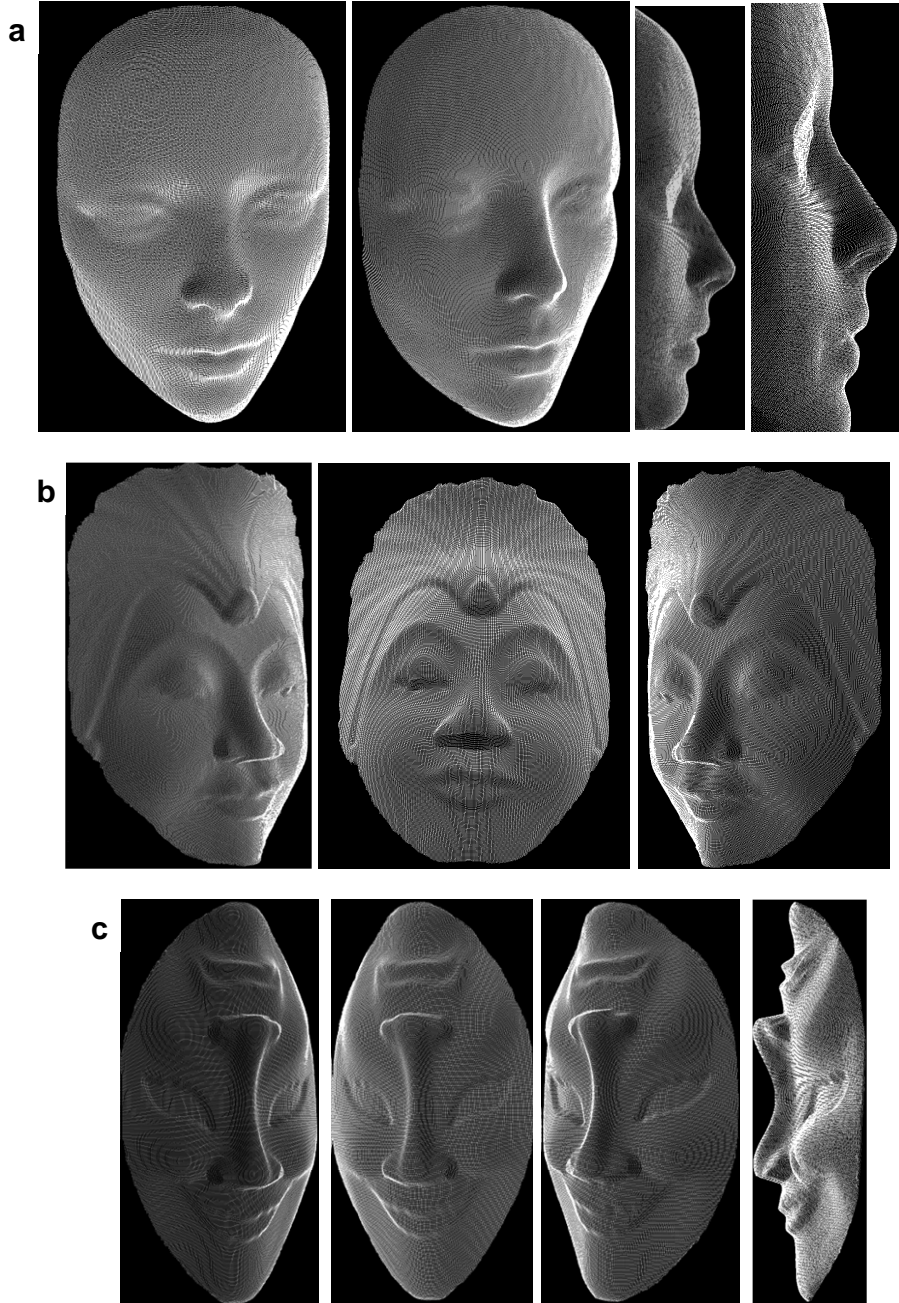
Figure 4.14. 3D surface reconstruction shown by raw point-cloud representations after using SWT-FFT grid removal for a) manikin head, b) crowned mask, and c) double-faced mask.

4.5 Discussion

The requirement of precise mechanical grid translation and multiple-frame capture are the main limitations of continuous and discrete averaging grid removal methods, respectively. Moiré pattern blurring, introduction of artifacts, and inability to completely remove curved grid lines are the main limitations in previous single-image filtering grid removal techniques. A single-frame grid removal technique using combined stationary wavelet and Fourier transform (SWT-FFT) was developed for application in single-frame digital moiré 3D surface-shape measurement. The technique avoids the need to capture multiple frames and perform mechanical translation of optical components for grid removal in moiré-based measurement. SWT-FFT had the best performance in removing the grid lines, both straight and curved lines, minimizing artifacts in the de-noised image, and preserving the moiré pattern without blurring and degradation. Applying SWT to the images contaminated with grid lines made it possible to use a Daubechies wavelet with a low number of vanishing moments to decrease smoothing and distortion in the reconstructed de-noised image. Appling FFT and damping the wavelet coefficients related to grid lines improves SWT in removing highly curved grid lines without increasing decomposition level and smearing of the moiré pattern. In comparison to other techniques, combined SWT-FFT had the lowest noise amplitude in the reconstructed height and lowest roughness index for all test objects. The ability of SWT-FFT to remove grid lines using only a single frame makes it possible to apply single-frame digital phase-shifting moiré in 3D surface-shape measurement.

Chapter 5

Two-image and three-image temporal phase unwrapping

In this chapter, two-image and three-image digital-moiré temporal phase unwrapping were developed to compute an accurate continuous phase map using projection of two and three grid patterns of different frequencies, respectively. The method requires projection of only a single binary grid and capture of a single image for each grid pitch to calculate the wrapped phase map, while phase-shifting is performed digitally in a post-process. The phase-shift analysis results in phase maps with different moiré wavelengths. Calculation of the moiré wavelength for each phase map during the system calibration enables the use of the noisy extended phase map as a reference to unwrap either of the phase maps with the shorter wavelengths. This permits accurate continuous phase map computation using fewer images than for fringe projection methods.

5.1 Digital phase-shifting moiré

The method of temporal phase unwrapping using multi-wavelength digital phase-shifting moiré involves projecting multiple binary grid patterns of different pitch onto the object surface, and capturing only a single image for each projected pattern. Then, for each captured image (of different pitch), a synthetically produced (computer generated) grid of the same pitch as the captured image is overlaid on the captured image and digitally shifted to generate multiple phase-shifted moiré images, as detailed in Chapter 3.

The generated phase-shifted moiré images contain the moiré contours as well as the unwanted high-frequency grid-pattern. Grid removal is then performed to extract pure moiré patterns, as detailed in Chapter 4. The intensity distribution of the phase-shifted moiré patterns after grid removal is described by:

$$I_i(x,y) = a(x,y) + b(x,y)\cos(\Phi(x,y) + \delta_i) \quad , \tag{5.1}$$

where $a(x,y)$ and $b(x,y)$ are intensity background and modulation, respectively, (x,y) are the image coordinates, $\Phi(x,y)$ is the phase map that contains object height information, and $\delta_i = 2\pi i/N$ are the phase-shifts between images. To calculate the phase map $\Phi(x,y)$, at least three images (N=3) of phase-shifted moiré patterns are required:

$$\Phi(x,y) = -\tan^{-1}\left(\frac{\sum_{i=1}^{N} I_i(x,y)\sin\delta_i}{\sum_{i=1}^{N} I_i(x,y)\cos\delta_i}\right), i = 1,2,\dots,N. \tag{5.2}$$

Because of the arctan function in Eq. 5.2, the computed phase $\Phi(x,y)$ is wrapped in the range $[-\pi, \pi]$, and a 2D phase unwrapping technique is required to calculate a continuous phase map $\varphi(x,y)$. This process removes the 2π ambiguities of the wrapped phase according to the fringe order $m(x,y)$.

$$\varphi(x,y) = \Phi(x,y) + (2\pi)m(x,y). \tag{5.3}$$

The relationship between the computed unwrapped phase $\varphi(x,y)$ and object height h depends on the system-geometry parameters and can be expressed as follows:

$$h(x,y) = K\varphi(x,y). \tag{5.4}$$

The coefficient K is a function of the moiré-wavelength λ:

$$K = \frac{\lambda}{2\pi}. \tag{5.5}$$

Eq. (5.4) can thus be rewritten as:

$$h(x,y) = \frac{\lambda}{2\pi}\big(\Phi(x,y) + (2\pi)m(x,y)\big). \tag{5.6}$$

5.2 System calibration

5.2.1 Computation of the moiré wavelength

Computation of the moiré wavelength λ for each phase map can be performed in a system calibration process as follows (detailed in Chapter 3). A flat plate is mounted on a translation stage and moved toward the camera-projector plane to several known positions (depths or heights). At each position, the same grid pattern used during object measurement is projected onto the plate and an image is captured. For each plate position, a computer-generated grid pattern of the same pitch as in the captured image, is digitally superimposed onto the captured image to generate a moiré pattern. The generated images (for all positions) are filtered to remove the high frequency grid and extract pure moiré patterns. The intensity at a single pixel is tracked across all plate positions (over depth). For every pixel, the moiré fringe intensities across plate positions follow a near-sinusoidal function of the plate translation. The moiré wavelength can be estimated by the distance between two successive maxima (bright fringes) or two successive

minima (dark fringes), respectively. It is common to assume that λ is constant between successive moiré fringes; however, the moiré wavelength decreases with increasing calibration depth. To determine the moiré wavelength as a function of height, the moiré wavelength is first computed at each pair of successive peaks from the tracked intensities over plate positions. The average moiré wavelength over all pixels is then computed at the different peak pairs corresponding to different plate positions (heights). Finally, the moiré wavelength as a function of height is approximated by a line fit to all average moiré wavelengths computed at different peak pairs. The capture of multiple images is only required during system calibration, and not during object measurement. To perform heterodyne temporal phase unwrapping, multiple phase maps are required, and the wavelength corresponding to the middle calibration depth is used for each phase map.

5.2.2 *X-Y* plane calibration

To perform *X-Y* plane calibration, the mapping of pixel coordinates to real world coordinates is computed using a method similar to that in Chapter 3. However, a modified method is used to refine the scaling parameters at each height (depth, *Z* axis);

$$(P_x)_z = \frac{W}{(N_x)_z} \ , \quad (P_y)_z = \frac{L}{(N_y)_z}. \tag{5.7}$$

where, $(N_x)_z$ and $(N_y)_z$ are the number of pixels in the captured image corresponding to the true width *W* and length *L* of the object of known geometry, and $(P_x)_z$ and $(P_y)_z$ are the refined scaling parameters, respectively, at each depth. $(N_x)_z$ and $(N_y)_z$ for the reference plate were determined at multiple height (depth) positions using the same images obtained during the system calibration for moiré wavelength.

5.3 Digital-moiré temporal phase unwrapping

5.3.1 Two-wavelength phase-unwrapping

For two-wavelength digital-moiré temporal phase-unwrapping, two fringe patterns of different pitch are projected onto the object surface and a single image is captured for each projected pattern. Phase-shifted moiré patterns (images) are generated by digitally phase shifting a computer-generated grid overlaid on the captured images, followed by grid removal, described in Chapter 4. Phase shift analysis is then applied to compute two wrapped phase maps Φ_1, Φ_2 with

different moiré wavelengths λ_1, λ_2 $(\lambda_2 > \lambda_1)$. In FPP techniques, at least six captured images are needed to perform two-frequency temporal phase unwrapping, while in this research, only two captured images are required. The moiré wavelength of each moiré pattern λ_1, λ_2, are calculated in the calibration stage, as explained in Chapter 3.

From phase maps Φ_1 and Φ_2, an extended continuous phase map Φ_{12} with extended wavelength λ_{12}, where $\lambda_{12} = \frac{\lambda_1 \lambda_2}{|\lambda_1 - \lambda_2|}$, is then calculated:

$$\Phi_{12}(x,y) = \begin{cases} \Phi_1(x,y) - \Phi_2(x,y), & \Phi_1 > \Phi_2 \\ \Phi_1(x,y) - \Phi_2(x,y) + 2\pi, & \text{otherwise} \end{cases} \tag{5.8}$$

Here, the beat wavelength λ_{12} is large enough to cover the entire range of the object's depth $h(x,y)$ (i.e. continuous gray level gradient, no phase ambiguity in Φ_{12}). To minimize the phase error caused by noise, Φ_{12} can be used as a reference to unwrap the phase map Φ_1, which has the lower wavelength λ_1, as follows:

$$\varphi(x,y) = \Phi_1(x,y) + (2\pi) Round\left(\frac{\left(\lambda_{12}/\lambda_1 \right) \Phi_{12}(x,y) - \Phi_1(x,y)}{2\pi} \right), \tag{5.9}$$

where $\varphi(x,y)$ is the unwrapped phase map and $Round(\ )$ computes the closest integer value. This high-SNR unwrapped phase map $\varphi(x,y)$ can then be used during measurement to calculate the object height:

$$h(x,y) = \frac{\lambda_1}{2\pi} \varphi(x,y) \ . \tag{5.10}$$

5.3.2 Three-wavelength phase-unwrapping

A wrapped phase map with large wavelength has few phase jumps but tends to be noisy, while a phase map with smaller wavelength has more phase jumps, but higher SNR. In two-wavelength phase unwrapping the beat wavelength may not be sufficient to cover the entire object depth, leaving phase ambiguity. Increasing the pitch of projected patterns to enlarge the wavelengths λ_1 and λ_2, may help the beat wavelength to cover the entire object depth; however, this sacrifices SNR in the extended unambiguous phase map, which makes the phase unwrapping process unreliable.

Three-wavelength or multi-wavelength heterodyne phase-unwrapping can further increase the beat wavelength without sacrificing SNR in the extended phase map. In three-wavelength digital-moiré temporal phase-unwrapping, three fringe patterns of different pitch are projected onto the object and a single image is captured for each projected pattern. Three wrapped phase maps Φ_1, Φ_2, Φ_3 with different wavelengths λ_1, λ_2, λ_3, $(\lambda_3 > \lambda_2 > \lambda_1)$ are computed using only three captured images. Three scale factors (λ_{12}/λ_2), (λ_{23}/λ_2), and $(\lambda_{123}/\lambda_2)$ from three beat wavelengths, $\lambda_{12} = \frac{\lambda_1 \lambda_2}{|\lambda_1 - \lambda_2|}$, $\lambda_{23} = \frac{\lambda_2 \lambda_3}{|\lambda_2 - \lambda_3|}$, and $\lambda_{123} = \frac{\lambda_{12} \lambda_{23}}{|\lambda_{12} - \lambda_{23}|}$ are used in the phase unwrapping process to produce an extended continuous phase map that covers the entire object range of depth. An extended phase map Φ_{12} with extended wavelength λ_{12}, is computed from phase maps Φ_1 and Φ_2 as follows:

$$\Phi_{12}(x,y) = \begin{cases} \Phi_1(x,y) - \Phi_2(x,y), & \Phi_1 > \Phi_2 \\ \Phi_1(x,y) - \Phi_2(x,y) + 2\pi, & \text{otherwise} \end{cases} \quad (5.11)$$

To minimize the noise in Φ_{12}, Φ_{12} is used as a reference to unwrap the phase map Φ_2 with wavelength λ_2, which results in $\Phi'_{12}(x,y)$ with higher SNR than Φ_{12}:

$$\Phi'_{12}(x,y) = \Phi_2(x,y) + (2\pi)Round\left(\frac{\left(\lambda_{12}/\lambda_2\right)\Phi_{12}(x,y) - \Phi_2(x,y)}{2\pi}\right), \quad (5.12)$$

An extended phase map Φ_{23} with extended wavelength λ_{23}, is computed from phase maps Φ_2 and Φ_3 in a similar manner to Φ_{12}:

$$\Phi_{23}(x,y) = \begin{cases} \Phi_2(x,y) - \Phi_3(x,y), & \Phi_2 > \Phi_3 \\ \Phi_2(x,y) - \Phi_3(x,y) + 2\pi, & \text{otherwise} \end{cases} \quad (5.13)$$

Again to minimize noise, $\Phi'_{23}(x,y)$ with higher SNR than Φ_{23} is calculated as follows:

$$\Phi'_{23}(x,y) = \Phi_2(x,y) + (2\pi)Round\left(\frac{\left(\lambda_{23}/\lambda_2\right)\Phi_{23}(x,y) - \Phi_2(x,y)}{2\pi}\right), \quad (5.14)$$

The extended continuous phase map Φ_{123} with extended wavelength λ_{123} that covers the entire object range of depth $h(x,y)$ (i.e. no phase ambiguity in Φ_{123}), is computed from phase maps $\Phi'_{12}(x,y)$ and $\Phi'_{23}(x,y)$:

$$\Phi_{123}(x,y) = \begin{cases} \Phi'_{12}(x,y) - \Phi'_{23}(x,y), & \Phi'_{12} > \Phi'_{23} \\ \Phi'_{12}(x,y) - \Phi'_{23}(x,y) + 2\pi, & \text{otherwise} \end{cases} \quad (5.15)$$

Finally, the phase unwrapping of Φ_2 is performed using the extended continuous phase map $\Phi_{123}(\text{x}, \text{y})$ as follows:

$$\varphi(x,y) = \Phi_2(x,y) + (2\pi)Round\left(\frac{\left(\lambda_{123}/\lambda_2\right)\Phi_{123}(x,y) - \Phi_2(x,y)}{2\pi}\right), \tag{5.16}$$

This high-SNR unwrapped phase map $\varphi(x, y)$ can then be used during measurement to calculate the object height:

$$h(x,y) = \frac{\lambda_2}{2\pi}\,\varphi(x,y)\;. \tag{5.17}$$

5.4 Experiments and Results

5.4.1 Experimental setup

To demonstrate the method of digital-moiré multi-wavelength temporal phase unwrapping, experiments were performed using an optical setup including a LCD projector (Panasonic PT-AE7000U) and monochrome CCD camera 2048 x 2048 resolution, with approximately 11 deg camera-projector angle, and 2.5 m camera-projector-plane to object distance.

5.4.2 System Calibration

To calculate the moiré wavelengths, system calibration was performed using a flat plate mounted on a linear translation stage and translated to 200 positions in 1.25 mm increments over a 250 mm calibration depth with 0.007 mm translation precision. Three binary grid patterns with different grid pitches were projected onto the flat plate and three images with 10, 12, and 14-pixel grid-pitches, respectively, were capture at each of the different known plate positions. The capture of multiple images at different known positions is not required during object measurement, but was required during system calibration to calculate the moiré wavelengths. Phase-shifted moiré patterns (images) were generated by digitally phase shifting a computer-generated grid overlaid on the captured images, followed by grid removal, as described in Section 5.1. Finally, the procedure of moiré wavelength calculation was performed as described in Section 5.2.1 and the resulting moiré wavelengths were $\lambda_1 = 21.850$ mm, $\lambda_2 = 26.048$ mm, and $\lambda_3 = 30.573$ mm for the 10, 12, and 14-pixel-pitch images, respectively.

5.4.3 Measurement

Object measurements were performed by projecting onto the object a single grid pattern for each grid pitch used in the calibration, and capturing a single image for each pattern. Phase-shifted moiré patterns (images) were generated by digitally phase shifting a computer-generated grid of the same pitch as the captured image overlaid on the captured images, followed by grid removal. Phase-shift analysis was applied to extract the wrapped phase map $\Phi(x, y)$ for each grid pitch. The digital moiré temporal phase unwrapping method was performed on a mask with surface discontinuities, two spatially isolated objects (a mask with surface discontinuities and a manikin head) and a double-hemispherical object.

Two-wavelength temporal phase unwrapping was applied to the mask with surface discontinuities by projecting two binary grid patterns with the grid pitches used in the calibration, and capturing a single image for each pattern (10- and 12-pixel grid pitch) (Figs. 5.1a, 5.2a). For each grid pitch, a moiré pattern with high-frequency grid lines was generated by digital phase-shifting moiré (Figs. 5.1b, 5.2b), and a pure moiré pattern was extracted by grid removal (Figs. 5.1c, 5.2c). Two wrapped phase maps Φ_1 and Φ_2 (Figs. 5.1d, 5.2d) were computed with moiré wavelengths λ_1 and λ_2 (Section 5.4.2). The extended continuous phase map Φ_{12} (Fig. 5.3a) with extended beat wavelength $\lambda_{12} = \frac{\lambda_1 \lambda_2}{|\lambda_1 - \lambda_2|} = 135.567$ mm, which covers the entire range of depth, was computed from wrapped phase maps Φ_1 and Φ_2 (Figs. 5.1d, 5.2d).

| (a) | (b) | (c) | (d) |
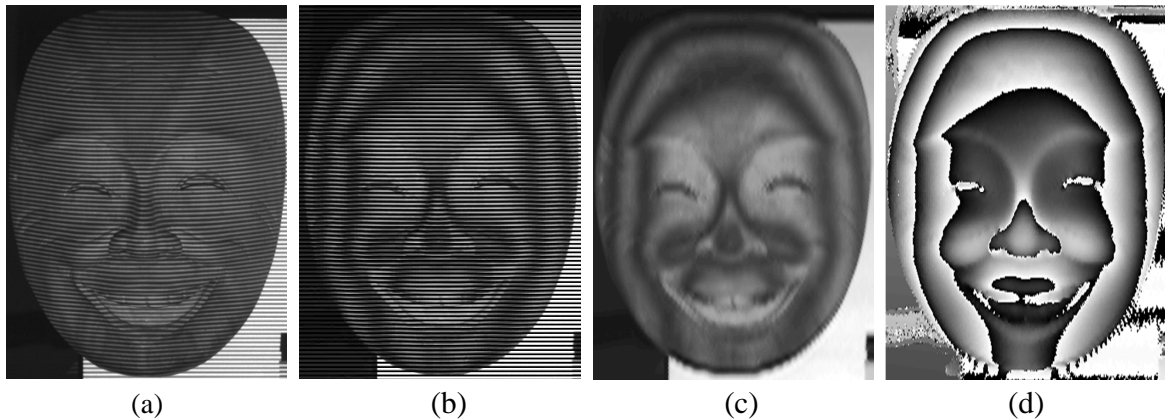
Figure 5.1. Wrapped phase map computation: a) original captured image of the mask with binary grid of 10-pixel pitch, b) generated image with moiré pattern and high-frequency grid lines, c) moiré pattern after grid removal, and d) wrapped phase map Φ_1.
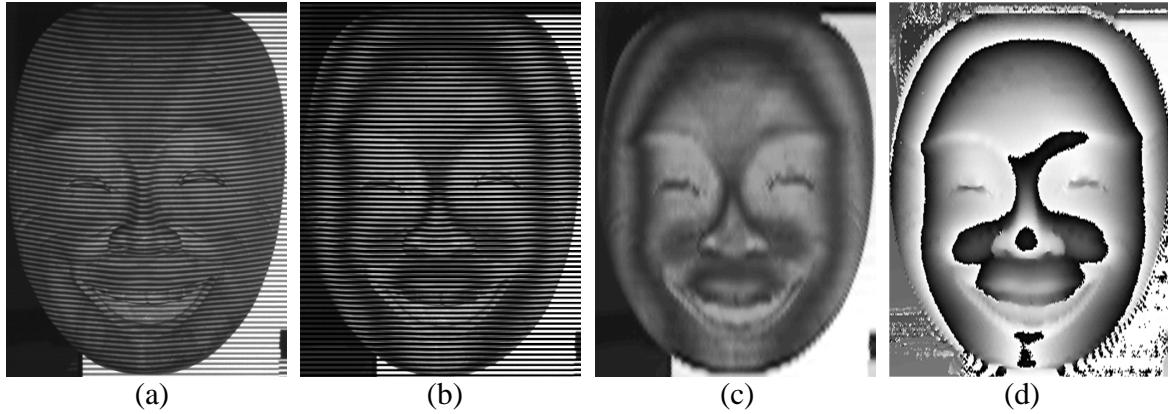
Figure 5.2. Wrapped phase map computation: a) original captured image of the mask with binary grid of 12-pixel pitch, b) generated image with moiré pattern and high-frequency grid lines, c) moiré pattern after grid removal, and d) wrapped phase map Φ_2.
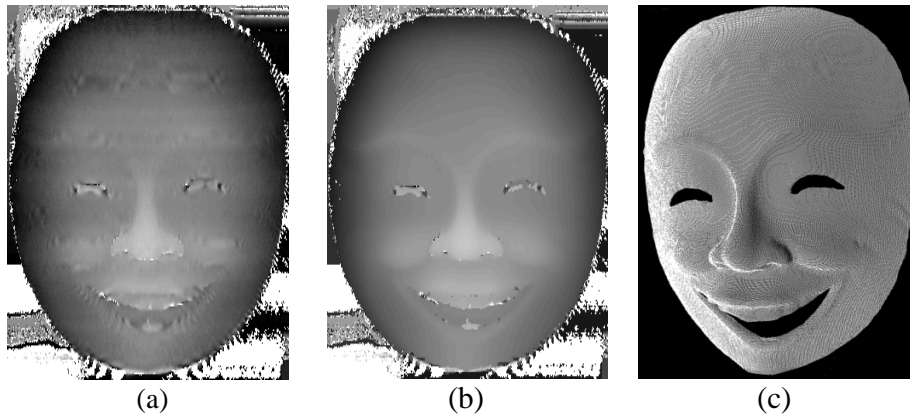
Figure 5.3. a) Extended continuous phase map Φ_{12} with extended beat wavelength λ_{12}, b) unwrapped phase map φ, and c) point cloud representation of measured points of mask.

To minimize the phase error caused by the noise in Φ_{12}, Φ_{12} with no phase ambiguity was used as a reference to unwrap the phase map Φ_1 with smaller moiré wavelength λ_1, to obtain the unwrapped phase map φ (Fig. 5.3b). The result demonstrates the ability to obtain an unwrapped phase map with high SNR to perform accurate 3D measurement (Fig. 5.3c) of objects with discontinuities, using only two captured images.

Three-wavelength temporal phase unwrapping was applied to two spatially isolated objects: a mask with surface discontinuities and a manikin head. To handle the greater depth of the manikin compared to the mask, the beat wavelength was increased without sacrificing SNR in the extended phase map, by projection of another pattern with greater grid pitch. Thus, three binary grid patterns with different grid pitches were projected onto the objects and a single image

was captured for each pattern (10-, 12-, and 14-pixel grid pitch) (Figs. 5.4a, 5.5a, and 5.6a). For each grid pitch, a moiré pattern with high-frequency grid lines was generated by digital phase-shifting moiré (Figs. 5.4b, 5.5b, and 5.6b) and a pure moiré pattern was extracted by grid removal (Figs. 5.4c, 5.5c and 5.6c).

| (a) | (b) | (c) |
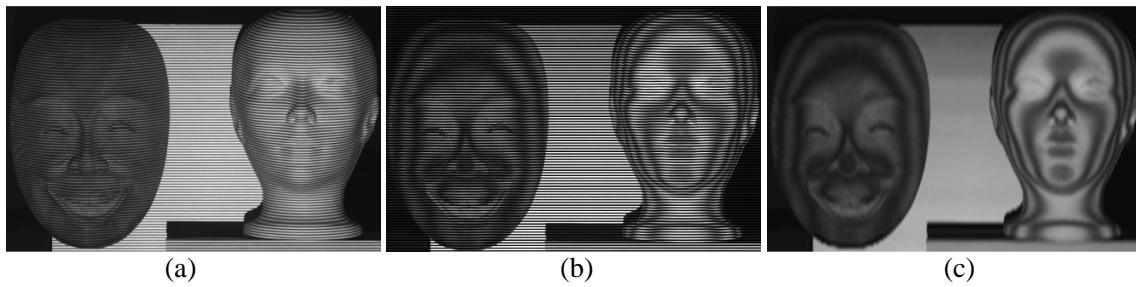
Figure 5.4. Moiré pattern generation: a) original captured image of objects with binary grid of 10-pixel pitch, b) generated image with moiré pattern and high-frequency grid lines, and c) moiré pattern after grid removal.

| (a) | (b) | (c) |
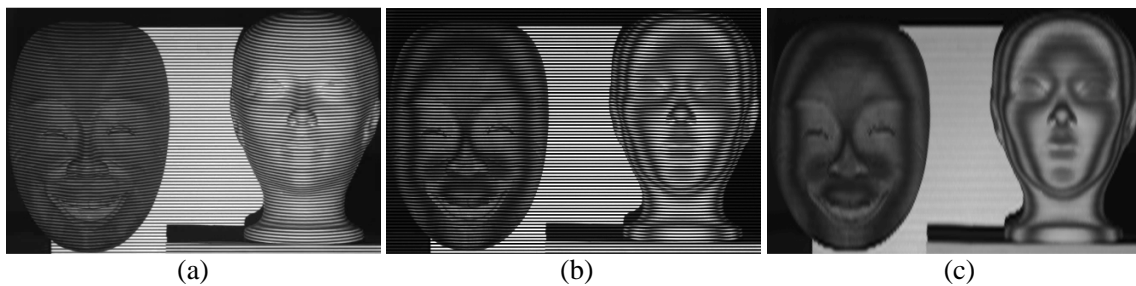
Figure 5.5. Moiré pattern generation: a) original captured image of objects with binary grid of 12-pixel pitch, b) generated image with moiré pattern and high-frequency grid lines, and c) moiré pattern after grid removal.

| (a) | (b) | (c) |
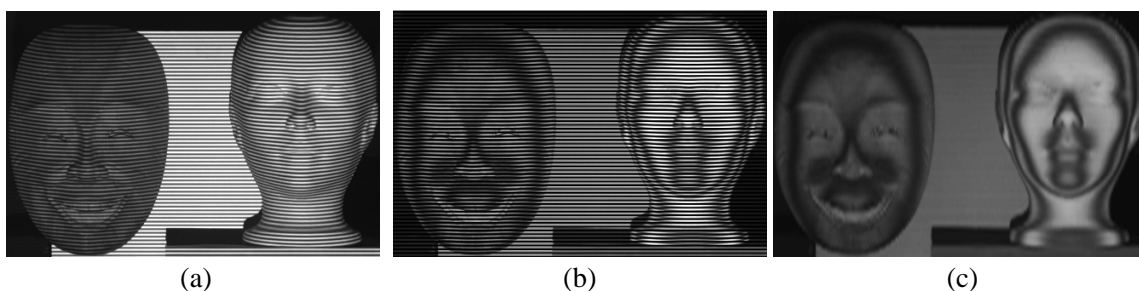
Figure 5.6. Moiré pattern generation: a) original captured image of objects with binary grid of 14-pixel pitch, b) generated image with moiré pattern and high-frequency grid lines, and c) moiré pattern after grid removal.

Three wrapped phase maps Φ_1, Φ_2, and Φ_3 (Figs. 5.7a, 5.7b and 5.7c) were computed with different moiré wavelengths λ_1, λ_2, and λ_3 (Section 5.4.2). The extended phase map Φ_{12} (Fig. 5.8a) with extended beat wavelength $\lambda_{12} = \frac{\lambda_1 \lambda_2}{|\lambda_1 - \lambda_2|} = 135.567$ mm was computed from phase maps Φ_1 and Φ_2. To minimize the phase error caused by the noise in Φ_{12}, Φ_{12} was used as a reference to unwrap the phase map Φ_2 with smaller moiré wavelength λ_2, to obtain the phase map Φ'_{12} (Fig. 5.8b) with higher SNR.

(a)   (b)   (c)
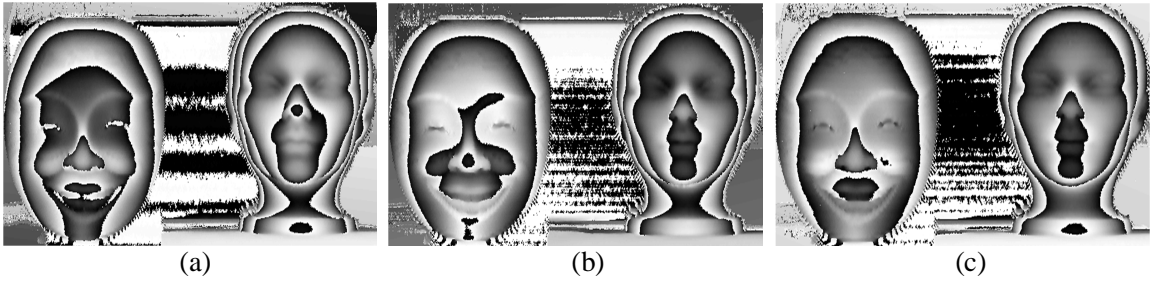
Figure 5.7. Wrapped phase maps a) Φ_1, b) Φ_2, and c) Φ_3

A second extended phase map Φ_{23} (Fig. 5.9a) with extended beat wavelength $\lambda_{23} = \frac{\lambda_2 \lambda_3}{|\lambda_2 - \lambda_3|} = 175.986$ mm was computed from phase maps Φ_2 and Φ_3. To minimize the phase error caused by the noise in Φ_{23}, Φ_{23} was used as a reference to unwrap the phase map Φ_2 with smaller moiré wavelength λ_2, to obtain the phase map Φ'_{23} (Fig. 5.9b) with higher SNR. Using the method in [54], the extended continuous phase map (Fig. 5.10a), which covers the entire range of depth, was computed from phase maps Φ_{12} (Fig. 5.8a) and Φ_{23} (Fig. 5.9a), resulting in a noisy phase map (Fig. 5.10a). The extended continuous phase map with high SNR Φ_{123} (Fig. 5.10b) with extended beat wavelength $\lambda_{123} = \frac{\lambda_{12} \lambda_{23}}{|\lambda_{12} - \lambda_{23}|} = 590.269$ mm was calculated from high quality phase maps Φ'_{12} (Fig. 5.8b) and Φ'_{23} (Fig. 5.9b). Finally, to calculate a more accurate unwrapped phase map with high SNR, Φ_{123} was used as a reference to unwrap Φ_2 with smaller moiré wavelength λ_2, to obtain the unwrapped phase map φ (Fig. 5.10c), which has high SNR. This high-SNR unwrapped phase map enables accurate 3D measurement of objects with discontinuities and multiple spatially-isolated objects (Fig. 5.11) using only three captured images.
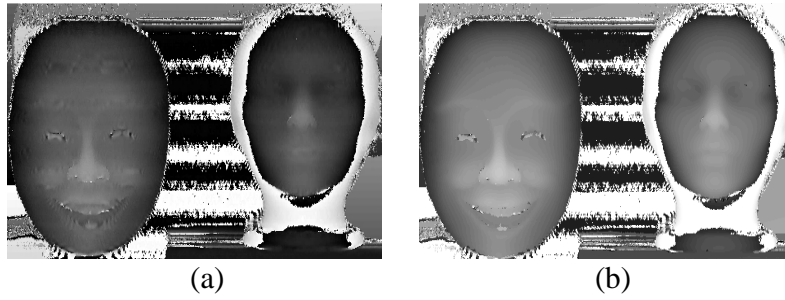
Figure 5.8. Extended phase maps: a) Φ_{12} with extended beat wavelength λ_{12}, and b) Φ'_{12} with higher SNR.
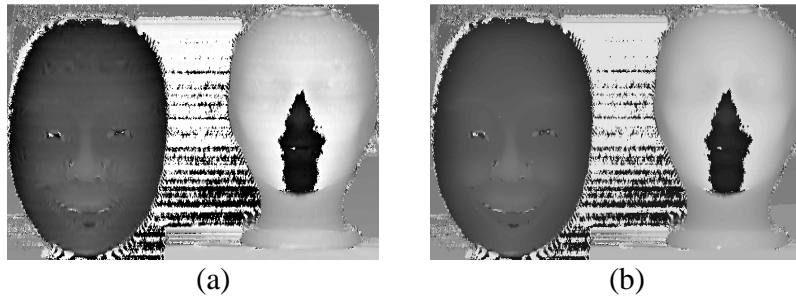
Figure 5.9. Extended phase maps: a) Φ_{23} with extended beat wavelength λ_{23}, and b) Φ'_{23} with higher SNR.
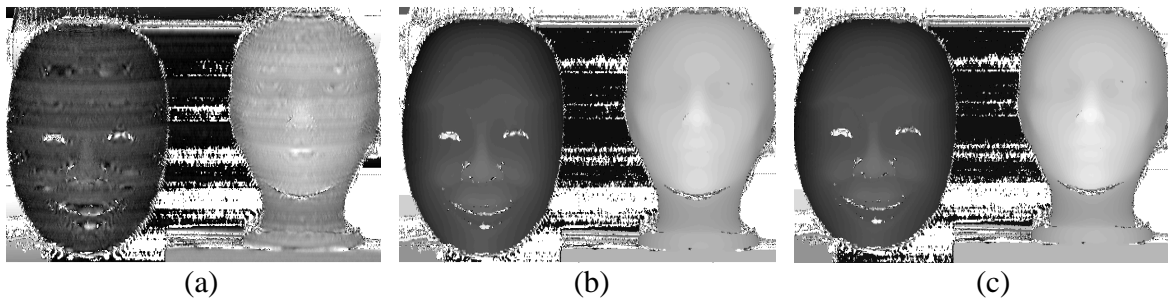
Figure 5.10. Extended continuous phase maps: a) extended continuous phase map based on [54] calculated from Φ_{12} and Φ_{23}, b) Φ_{123} with high SNR and with extended beat wavelength λ_{123} calculated from Φ'_{12} and Φ'_{23}, and c) unwrapped phase map φ.
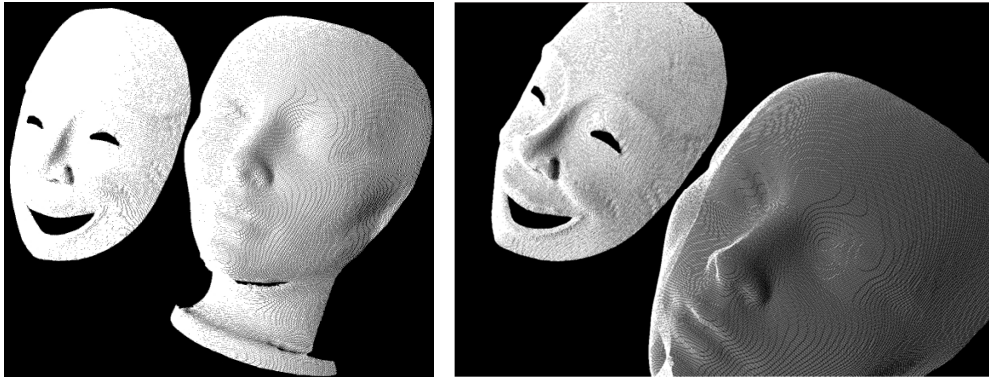
Figure 5.11. Point cloud representations of measured points of spatially isolated objects, mask and manikin head.

To demonstrate the measurement accuracy of the two-image digital-moiré temporal phase unwrapping method, a double-hemispherical object with known radii of two hemispheres (true radius 50.80 mm) and known distance between the centers (120 mm) was measured. To increase the measurement resolution and accuracy, the calibration was performed by projecting two binary grid patterns with smaller grid pitches (resulting in 8- and 10-pixel grid pitch in the captured images) than for the other objects. Moiré wavelength calculation was performed and yielded moiré wavelengths $\lambda_1 =16.966$ mm and $\lambda_2 =21.035$ mm for the 8- and 10-pixel-pitch images, respectively. Two-wavelength temporal phase unwrapping was applied to the double-hemispherical object by projecting two binary grid patterns with the grid pitches used in the calibration, and capturing a single image for each pattern (8- and 10-pixel grid pitch) (Figs. 5.12a, 5.13a). For each grid pitch, a moiré pattern with high-frequency grid lines was generated by digital phase-shifting moiré (Figs. 5.12b, 5.13b), and a moiré pattern was extracted by grid removal (Figs. 5.12c, 5.13c).

| (a) | (b) | (c) |
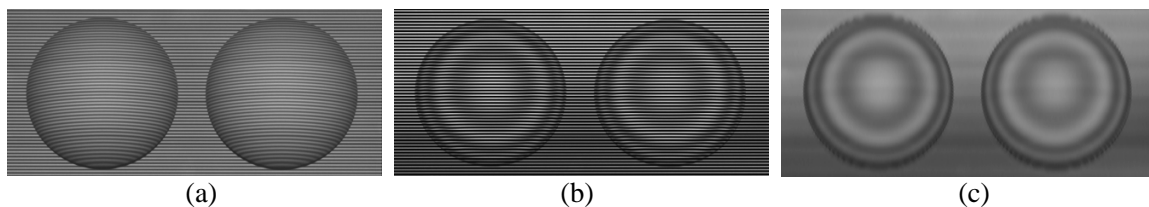
Figure 5.12. Moiré pattern generation: a) original captured image of double hemispherical object with binary grid of 8-pixel pitch, b) generated image with moiré pattern and high-frequency grid lines, and c) moiré pattern after grid removal.
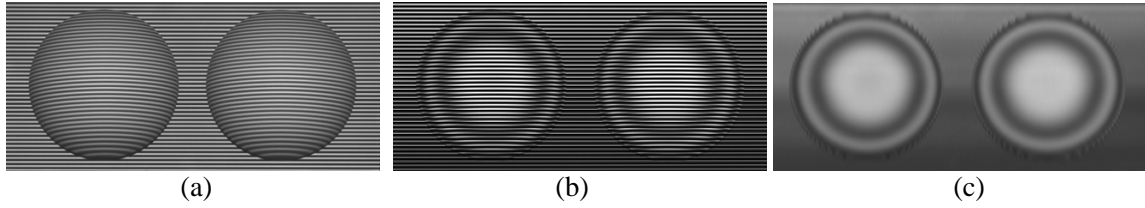
Figure 5.13. Moiré pattern generation: a) original captured image of double hemispherical object with binary grid of 10-pixel pitch, b) generated image with moiré pattern and high-frequency grid lines, and c) moiré pattern after grid removal.

Two wrapped phase maps Φ_1 and Φ_2 (Figs. 5.14a, 5.14b) were computed with moiré wavelengths λ_1 and λ_2. The extended continuous phase map Φ_{12} (Fig. 5.15a) with extended beat wavelength $\lambda_{12} = \frac{\lambda_1 \lambda_2}{|\lambda_1 - \lambda_2|} = 87.720$ mm, which covers the entire range of depth, was computed from wrapped phase maps Φ_1 and Φ_2 (Figs. 5.14a and 5.14b). To minimize the phase error caused by the noise in Φ_{12}, Φ_{12} with no phase ambiguity was used as a reference to unwrap the phase map Φ_1 with smaller moiré wavelength λ_1, to obtain the unwrapped phase map φ (Fig. 5.15b). Height measurement was performed using Eq. (5.10) and least-squares fitted spheres to the measured 3D point cloud data (Fig. 5.15c) had radii of 50.833 mm and 50.738 mm, and thus errors of 0.033 mm and 0.062 mm, respectively (sphere fitting standard deviations were 0.146 mm and 0.142 mm). Centre-to-centre distance between hemispheres was 119.812 mm, thus with an error of 0.188 mm.
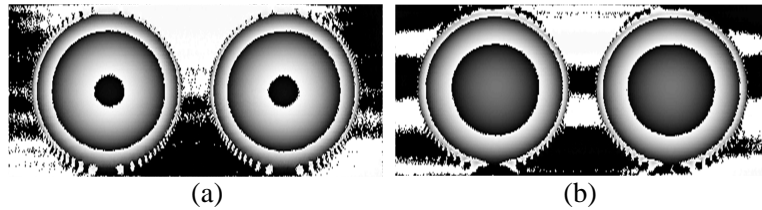
Figure 5.14. Wrapped phase maps: a) Φ_1, b) Φ_2.
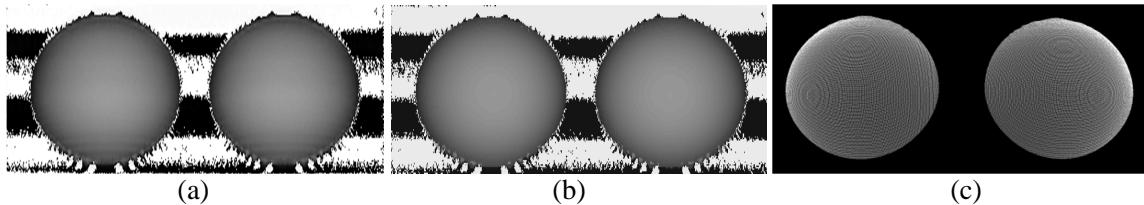
Figure 5.15. a) Extended continuous phase map Φ_{12} with extended beat wavelength λ_{12}, b) unwrapped phase map φ, and c) point cloud representation of double hemispherical object.

A sample cross-section of measured points with the true semicircles is shown in Fig. 5.16, The measured points are close to the true values for most of the surface. As commonly occurring, larger errors are seen near the edge of the surface, where the camera and projector optical axes are nearly parallel to the surface.
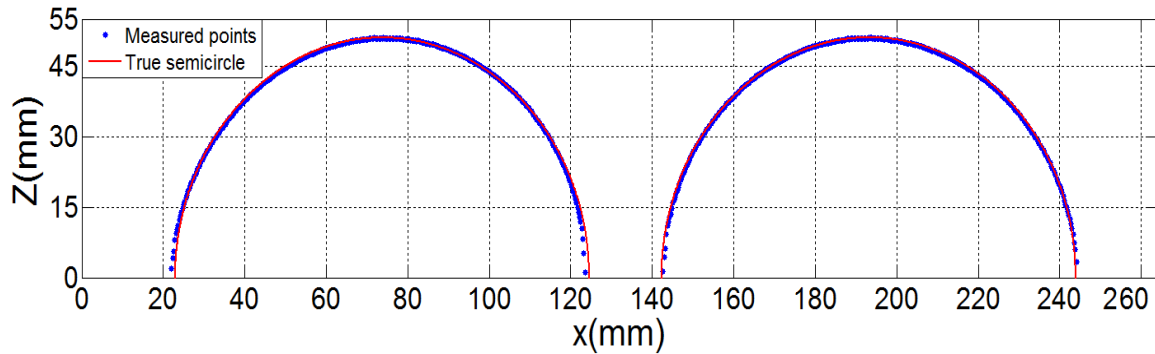
Figure 5.16. Sample cross-section of measured points of double hemispherical object and true semicircles.

5.5 Discussion

Two-image and three-image temporal phase unwrapping, developed in this chapter for digital moiré, yields a high-SNR unwrapped phase map and is thus an improvement over previous temporal phase unwrapping for digital moiré. Moiré wavelength calculation during the system calibration provides an ability to use the extended noisy phase map as a reference to unwrap the phase map with shorter wavelength, and thus achieve a less noisy and more accurate continuous phase map. Only a single pattern has to be projected and thus single image captured to compute each phase map with different wavelength to perform temporal phase unwrapping by digital moiré. The number of captured images required by this new method is one third that for three-wavelength heterodyne temporal phase unwrapping by fringe projection techniques. Decreasing the number of required captured images would be advantageous in measuring dynamic objects, either moving or deforming.

Chapter 6

Contributions and Future Work

This chapter summarizes contributions of the thesis research, and proposes future work. In this thesis, 3D optical metrology techniques were developed for accurate high resolution 3D surface-shape measurement toward minimizing the number of patterns projected and images (frames) captured by camera, using digital moiré: single pattern projection for 3D measurement of objects with continuous surface geometry, and two and three pattern projection for 3D measurement of objects with surface discontinuities and spatially isolated objects.

6.1 Contributions

The main contributions of the research of this thesis are as follows:

1. Developed digital moiré for high resolution and accurate single-frame 3D-shape measurement of objects without surface discontinuity:

    1.1 A new calibration technique in digital moiré to compute height from phase without requiring direct measurement of the system geometry parameters was developed based on moiré-wavelength phase-to-height mapping in the system-calibration stage. This is an improvement over previous digital moiré techniques by avoiding direct measurement of optical system geometry parameters required by previous methods.

    1.2 A new pixel-wise phase-to-height mapping system-calibration was developed based on moiré-wavelength refinement, and permits object surface measurement over extended depth, while maintaining high measurement accuracy. The computed wavelength-height function takes into account the moiré wavelength variation over calibration depth when measuring an object over extended depth. The novel moiré-wavelength refinement technique, which performs pixel-wise computation of the wavelength based on height (depth), improved measurement accuracy by height refinement, compared to measurement using a single global wavelength across all pixels. The new method was able to measure surface height using only a single captured frame of the object surface with only a single projected pattern. Furthermore, the projected pattern was a simple binary grid, which avoids problems associated with gamma nonlinearity.

2. Developed a new single-frame grid removal technique based on combined SWT-FFT for application in single-frame digital moiré 3D shape measurement that addresses the needs to remove high-frequency grid lines, without introducing artifacts, while preserving the moiré pattern without blurring and degradation.

The ability of the stationary wavelet transform (SWT) to prevent oscillation artifacts near discontinuities, and the ability of the Fourier transform (FFT) applied to wavelet coefficients to further separate grid lines from useful image information, were combined in a new technique, SWT-FFT, to remove grid lines from moiré-pattern images generated by digital moiré. In comparison to previous grid removal techniques in moiré, SWT-FFT avoids the requirement for mechanical translation of optical components and capture of multiple frames, to enable single-frame moiré-based measurement. The measurement results have demonstrated that SWT-FFT had the best performance in removing the grid lines, both straight and curved lines, minimizing artifacts in the de-noised image, and preserving the moiré pattern without blurring and degradation. In comparison to other techniques, combined SWT-FFT had the lowest noise amplitude in the reconstructed height and lowest roughness index for different test objects.

3. Developed new temporal phase unwrapping techniques for measurement of spatially isolated and discontinuous surfaces:

3.1. An improved temporal phase unwrapping method was developed using multi-wavelength digital phase-shifting moiré to address the limitations of the high number of projected patterns and captured images of temporal phase unwrapping in FPP, and the low signal-to-noise ratio of the extended phase map of temporal phase unwrapping in digital moiré.

Two-image and three-image digital-moiré temporal phase unwrapping were developed using projection of two and three binary-grid patterns of different frequencies, respectively. Experiments demonstrated accurate high resolution 3D surface-shape measurement of objects with surface discontinuities and spatially isolated objects. The number of captured images required by this new method is one third that for the common heterodyne temporal phase unwrapping by fringe projection techniques. Minimizing the number of required captured images would be advantageous in measuring dynamic objects, either moving or deforming.

6.2 Limitations and Future Work

1. For the techniques developed in this research, a reference plate is required during object surface measurement. Encoding a marker or colour-stripe in the projected pattern as in [85, 86] might avoid the need for the reference plate, and thus simply the measurement setup.

Recommended future work would be to:

- Devise a new technique or new projection pattern to perform absolute measurement of objects without requiring to the reference plate during measurement:

2. The developed grid removal technique based on SWT-FFT requires adjusting of two parameters: the decomposition level of the wavelet transform and the damping factor of the Gaussian function in the Fourier transform. The decomposition level depends on the pitch of the captured grid on the object surface and the damping factor depends on the curvature of the grid. The damping factor and decomposition level have to be as small as possible to keep the useful information unchanged, but large enough to remove the high frequency grids.

Recommended future work would be to:

- Make the grid removal technique automatic by detecting the pitch and curvature of the image-captured grid lines, and adjusting the decomposition level and the damping factor accordingly as described above. This could permit automatic grid removal and thus allow automated measurement.

3. The developed system calibration technique only performs phase-to-height mapping and requires separate *X-Y* plane calibration.

Recommended future work would be to:

- Develop a new calibration technique that combines stereo-vision [43-45] (using two cameras and one projector) with digital moiré. This could allow the 3D coordinates of the object surface to be computed from 2D image coordinates based on well-known established techniques for stereo cameras. This combination may allow the use of moiré patterns to aid determination of the correspondence between camera images and to use the intrinsic (camera optics) and extrinsic (system geometry) parameters in measurement as for stereo cameras. In another approach, the system calibration might be performed using a single camera projector system [45], where the

projector would be treated as an inverse camera, a virtual projector image generated, and the calibration parameters for the projector and camera used as for a two-camera stereovision system.

References

[1] K. Liu, Y. Wang, D. L. Lau, Q. Hao, L. G. Hassebrook ,"Dual-frequency pattern scheme for high-speed 3-D shape measurement", *Optics Express*, Vol. 18, No. 5, 5229-5244 (2010).

[2] X. Su, Q. Zhang, "Dynamic 3-D shape measurement method: A review", *Optics and Lasers in Engineering*, Vol.48, 191–204 (2010).

[3] M. Honegger, M. Kahl, S. Trunz, S. Rinner, A. Ettemeyer, P. Lambelet, "Scanning fringe projection for fast 3D inspection", *Proc. SPIE 8788, Optical Measurement Systems for Industrial Inspection* VIII, 878814 (2013).

[4] L. Ekstrand, N. Karpinsky, Y. Wang, S. Zhang, "High-resolution, high-speed, three-dimensional video imaging with digital fringe projection techniques", *Journal of Visualized Experiments*, Vol.82, e50421 (2013).

[5] L. Lu, J. Xi, Y. Yu, Q. Guo, "New approach to improve the accuracy of 3-D shape measurement of moving object using phase shifting profilometry", *Optics Express*, Vol. 21, No. 25, 30610-30622 (2013).

[6] S. Zhang, "Recent progresses on real-time 3D shape measurement using digital fringe projection techniques", *Optics and Lasers in Engineering*, Vol.48, 149–158 (2010).

[7] S. Zhang, "High-resolution, high-speed 3-d dynamically deformable shape measurement using digital fringe projection techniques", *Advances in Measurement Systems*, 29-50 (2010).

[8] B. Li , Y. Wang, J. Dai , W. Lohry, S. Zhang, "Some recent advances on superfast 3D shape measurement with digital binary defocusing techniques", *Optics and Lasers in Engineering*, Vol.54, 236–246 (2014).

[9] Y. Wang, J. I. Laughner, I. R. Efimov, S. Zhang, "3D absolute shape measurement of live rabbit hearts with a superfast two-frequency phase-shifting technique," *Opt. Express* 21(5), 5822-5832, (2013).

[10] J. I. Laughner, S. Zhang, H. Li, C. C. Shao, I. R. Efimov, "Mapping cardiac surface mechanics with structured light imaging," *American Journal of Physiology*: *Heart and Circular Physiology* 303(6), H712-H720, (2012).

[11] C. Ferreira, J. J. E. Taboada, J. Garcia, "Three-dimensional pattern recognition using fringe projection", *Proceeding of SPIE ,* Vol. 4435, 31-41 (2001).

[12] T. Weise, B. Leibe, L. V. Gool, "Fast 3D Scanning with Automatic Motion Compensation", *Computer Vision and Pattern Recognition Conference*, 1–8 (2007).

[13] B. Li, Z. Liu, S. Zhang," Motion artifact reduction using hybrid Fourier transform with phase-shifting methods", *Proc. of SPIE* Vol. 9960 99600K-1 (2016).

[14] J. Geng," Structured-light 3D surface imaging: a tutorial", *Advances in Optics and Photonics 3,* 128–160 (2011).

[15] S.S. Gorthi, P. Rastogi, "Fringe Projection Techniques: Whither we are?", *Optics and Lasers in Engineering*, 48(2):133-140, (2010).

[16] C. Waddington, J. Kofman," Modified sinusoidal fringe-pattern projection for variable illuminance in phase-shifting three-dimensional surface-shape metrology", *Optical Engineering* 53(8), 084109 (2014).

[17] P.S. Huang, F. Chiang, "Recent advances in fringe projection technique for 3-D shape measurement", *Proceeding of SPIE*, Vol. 3783, 132–142 (1999).

[18] H. Takasaki, "Moiré topography from its birth to practical application", *Optics and Lasers in Engineering*, Vol.3, 3–14 (1982).

[19] K. Creath and J. C. Wyant, ''Moire´ and fringe projection techniques,'' in Optical Shop Testing, D. Malacara, Ed., pp. 653–685, Wiley and Sons, New York (1992).

[20] J. J.J. Dirckx, J. A.N. Buytaert, S. A.M. Van der Jeught, ''Implementation of phase-shifting moiré profilometry on a low-cost commercial data projector,'' *Optics and Lasers in Engineering*,Vol.48, Issue 2, 244–250 (2010).

[21] V. Srinivasan, H. C. Liu, M. Halioua, ''Automated phase-measuring profilometry of 3-D diffuse objects,'' *Applied Optics* 28(18): 3105-3110 (1984).

[22] D. W. Phillion, ''General methods for generating phase-shifting interferometry algorithms,'' *Applied Optics* 36(31), 8098-8115, (1997).

[23] S. Zhang, D. van der Weide, J. Olvier, "Superfast phase-shifting method for 3-D shape measurement," *Opt. Express* 18, 9684–9689 (2010).

[24] P. Jia, J. Kofman, C. English, "Comparison of linear and nonlinear calibration methods for phase-measuring profilometry", *Optical Engineering*, Vol.46, No.4, 043601 (2007).

[25] H. Takasaki, "Moiré Topography", *Applied Optics*, Vol. 9, No.6, 1467–1472 (1970).

[26] L. Jin, Y. Kodera, T. Yoshizawa, Y. Otani,"Shadow moiré profilometry using the phase-shifting method", *Optical Engineering*, Vol.39, No.8, 2119–2123 (2000).

[27] H. Zhao, H. Du, J. Li, Y. Qin," Shadow moiré technology based fast method for the measurement of surface topography", *Applied Optics*, Vol. 52, No. 33(2013).

[28] Y.B. Choi, S.W. Kim, "Phase-shifting grating projection moiré topography", *Optical Engineering*, Vol.37, No.3, 1005–1010 (1998).

[29] J. A. N. Buytaert, J. J. J. Dirckx, "Design considerations in projection phase-shift moiré topography based on theoretical analysis of fringe formation", *Journal of the Optical Society of America. A*, Vol. 24, No. 7, 2003–2013 (2007).

[30] J.B. Allen, D.M. Meadows. "Removal of unwanted patterns from moiré contour maps by grid translation techniques". *Appl Opt*; 10(1): 210–12 (1971).

[31] L. Huang, Q. Kemao, B. Pan, A.K. Asundi, "Comparison of Fourier transform, windowed Fourier transform, and wavelet transform methods for phase extraction from a single fringe pattern in fringe projection profilometry", *Optics and Lasers in Engineering*, Vol.48, 141–148 (2010).

[32] X. Su, W. Chen, "Fourier transform profilometry", *Optics and Lasers in Engineering*, Vol.35 263–284 (2001).

[33] A. Dursun, S. Ozder, and F. N. Ecevit, "Continuous wavelet transform analysis of projected fringe patterns", *Measurement Science and Technology* 15(9): 1768-1772(2004).

[34] J. Ma, Z. Wang, B. Pan, T. Hoang, M. Vo, L. Luu, "Two-dimensional continuous wavelet transform for phase determination of complex interferograms", *Applied Optics*, Vol. 50, No. 16, 2425–2430 (2011).

[35] T. R. Judge, P. J. Bryanston-Cross," A Review of Phase Unwrapping Techniques in Fringe Analysis", *Optics and Lasers in Engineering* 21, 199-239 (1994).

[36] R. M. Goldstein, H. A. Zebker, C. L. Werner, "Satellite Radar Interferometry: Two-Dimensional Phase Unwrapping", *Radio Science*, Vol.23, No.4, 713–720 (1988).

[37] K. Chen, J. Xi, Y. Yu, "Quality-guided spatial phase unwrapping algorithm for fast three-dimensional measurement", *Optics Communications*, Volume 294, 139–147 (2013).

[38] J. M. Huntley, H. O. Saldner, "Temporal phase-unwrapping algorithm for automated interferogram analysis", *Applied Optics* 32(17): 3047-3052 (1993).

[39] H. O. Saldner, J. M. Huntley, "Temporal phase unwrapping: application to surface profiling of discontinuous objects", *Applied Optics* 36(13): 2770-75 (1997).

[40] H. Guo, H. He, Y. Yu, M. Chen, "Least-squares calibration method for fringe projection profilometry", *Optical Engineering*, Vol.44, No.3, 033603 (2005).

[41] C. Yu, Q. Peng, "A unified-calibration method in FTP-based 3D data acquisition for reverse engineering", *Optics and Lasers in Engineering*, Vol.45, 396–404 (2007).

[42] E. Zappa, G. Busca, "Fourier-transform profilometry calibration based on an exhaustive geometric model of the system", *Optics and Lasers in Engineering*, Vol.47, 754–767 (2009).

[43] X. Han, P.S. Huang, "Combined stereovision and phase shifting method: a new approach for 3D shape measurement", *Proceedings of SPIE* 7389: 125, (2009).

[44] Z. Zhang, "A Flexible New Technique for Camera Calibration", *IEEE Transactions on Pattern Analysis and Machine Intelligence*, Vol.22, No.11, 1330–1334 (2000).

[45] S. Zhang, P. Huang, "Novel method for structured light system calibration", *Optical Engineering*, Vol.45, No.8, 083601, (2006).

[46] Z.H. Zhang , "Review of single-shot 3D shape measurement by phase calculation-based fringe projection techniques", *Optics and Lasers in Engineering* 50(8), 1097–1106 (2012).

[47] C. Zuo, Q. Chen, G. Gu, S. Feng, F. Feng, R. Li, G. Shen, " High-speed three-dimensional shape measurement for dynamic scenes using bi-frequency tripolar pulse-width-modulation fringe projection", *Optics and Lasers in Engineering* 51, 953–960 (2013).

[48] S. Feng, Q. Chen, C. Zuo, R. Li, G. Shen, F. Feng, "Automatic identification and removal of outliers for high-speed fringe projection profilometry", *Optical Engineering*, Vol.52, No.1, 013605 (2013).

[49] T. Bell, S. Zhang, "Toward superfast three-dimensional optical metrology with digital micromirror device platforms", *Optical Engineering* 53(11), 112206 (2014).

[50] S. Heist, A. Mann, P. Kühmstedt, P. Schreiber, G. Notni, "Array projection of aperiodic sinusoidal fringes for high-speed three-dimensional shape measurement", *Optical Engineering*, Vol.53, No.11, 112208 (2014).

[51] B. Li, P. Ou, S. Zhang, "High-speed 3D shape measurement with fiber interference", *Proc. of SPIE* Vol. 9203 920310-1 (2014).

[52] J. Kato, I. Yamaguchi, T. Nakamura, S. Kuwashima, "Video-rate fringe analyzer based on phase-shifting electronic moiré patterns", *Applied Optics*, Vol. 36, No. 32, 8403– 8412 (1997).

[53] K.M. Chae, H.H. Lee, S.Y. Yim, S.H. Park, "Simplified phase shifting moiré interferometer using a computer generated grid pattern", *Jpn J Appl Phys*; 43(1):378–84 (2004).

[54] W.J. Ryu, Y.J. Kang, S.H. Baik, S.J. Kang, "A study on the 3-D measurement by using digital projection moiré method", *Optik*; 119: 453–8 (2008).

[55] J.J.J. Dirckx, W.F. Decraemer, "Automatic calibration method for phase shift shadow moiré interferometry", *Appl Opt*; 29(10):1474–76 (1990).

[56] Y. Wang, S. Zhang, "Novel phase-coding method for absolute phase retrieval", O*pt Lett*; 37(11):2067–9 (2012).

[57] J. Hyun, S. Zhang, "Superfast 3D absolute shape measurement using five binary patterns", *Optics and Lasers in Engineering* 90, 217–224 (2017).

[58] C. Reich, R. Ritter, J. Thesing, "White light heterodyne principle for 3D-measurement", *SPIE*; 3100: 236–44 (1997).

[59] S.W Kim, J.T Oh, M.S Jung, Y.B Choi, "Two-frequency phase-shifting projection moiré topography", *SPIE Conference on Three-Dimensional lmaginq, Optical Metroloy, and Inspection IV* SPIE Vol. 3520 (1998).

[60] M.S Jeong, S.W Kim, "Phase-Shifting Projection Moiré for Out-Of-Plane Displacement Measurement", *Second International Conference on Experimental Mechanics*, SPIE Vol. 4317 (2001).

[61] Y. Wang, B. Bhattacharya, E. H. Winer, P. Kosmicki, W.H. El-Ratal, S. Zhang, "Digital micromirror transient response influence on superfast 3D shape measurement", *Optics and Lasers in Engineering* 58 19–26 (2014).

[62] X. Su,W. Chen, "Fourier transform profilometry: a review", *Optics and Lasers in Engineering* Volume 35, Issue 5, 263–284 (2001).

[63] M. Servin, J.L. Marroquin, D. Malacara, F. J. Cuevas, "Phase unwrapping with a regularized phase-tracking system", *Applied Optics* Vol. 37, Issue 10, pp. 1917-1923 (1998).

[64] L. Kai, Q. Kemao,"Improved generalized regularized phase tracker for demodulation of a single fringe pattern. *Opt Express*; 21(2):24385–97 (2013).

[65] N. Kurihara, M. Sugiyama, H. Ogawa, K. Kitagawa, K. Suzuki, "Iteratively-Reweighted Local Model Fitting Method for Adaptive and Accurate Single-Shot Surface Profiling", *Applied Optics*, vol.49, no.22, 4270–4277 (2010).

[66] S. Mori, M. Sugiyama, H. Ogawa, K. Kitagawa, K. Irie, "Automatic parameter optimization of the local model fitting method for single-shot surface profiling", *Appl Opt*; 50(21):3773-80 (2011).

[67] H. J. Chen, J. Zhang, D. J. Lv, J. Fang, "3-D shape measurement by composite pattern projection and hybrid processing", *Optics Express*, Vol.15, No.19, 12318–12330 (2007).

[68] W.H. Su, "Colour-encoded fringe projection for 3D shape measurements", *Optics Express*, Vol.15, No.20, 13167–13181 (2007).

[69] C. Guan, L. G. Hassebrook, D. L. Lau, "Composite structured light pattern for three-dimensional video", *Optics Express*, Vol. 11, No. 5, 406–417 (2003).

[70] C. Guan, L. G. Hassebrook, D. L. Lau, V. G. Yalla, C. J. Casey," Improved composite-pattern structured-light profilometry by means of post-processing", *Opt. Eng*. 47(9), 097203 (2008).

[71] M. Takeda, Q. Gu, M. Kinoshita, H. Takai, Y. Takahashi, "Frequency-multiplex Fourier-transform profilometry: a single-shot three-dimensional shape measurement of objects with large height discontinuities and/or surface isolations", *Applied Optics*, Vol.36, No.22, 5347–5354 (1997).

[72] V. I. Gushov, Y. N. Solodkin, "Automatic processing of fringe patterns in integer interferometers," *Opt. Lasers Eng*.14, 311–324 (1991).

[73] J. Millerd, N. Brock, J. Hayes, M. North-Morris, M. Novak, and J. C. Wyant, "Pixelated phase-mask dynamic interferometer," *Proc. SPIE* 5531, 304–314 (2004).

[74] B. Salahieh, Z. Chen, J. J. Rodriguez, R. Liang, "Multi-polarization fringe projection for high dynamic range objects", *Optics Express*, Vol. 22, No.8, 10064–10071 (2014).

[75] J. Pan, P.S. Huang, F.P. Chiang, "Colour phase-shifting technique for three dimensional shape measurement", *Optical Engineering*, Vol.45, No.1, 013602 (2006).

[76] Z. Zhang, D.P. Towers, C.E. Towers, "Snapshot colour fringe projection for absolute three-dimensional metrology of video sequences", *Applied Optics*, Vol.49, No.31, 5947–5953 (2010).

[77] N. Karpinsky, S. Zhang, "Composite phase-shifting algorithm for three-dimensional shape compression", *Optical Engineering*, Vol.49, No.6, 063604 (2010).

[78] S. Ma, R. Zhu, C. Quan, B. Li, C.J. Tay, L. Chen, "Blind phase error suppression for color-encoded digital fringe projection profilometry", *Opt Commun*; 285(7):1662–68 (2012).

[79] I. Ishii, K. Yamamoto, K. Doi, T. Tsuji, "High-speed 3D image acquisition using coded structured light projection," in *IEEE/RSJ International Conference on Intelligent Robots and Systems*, 925–930 (2007).

[80] K. Sato, S. Inokuchi, "Range-imaging system utilizing nematic liquid crystal mask," in Proceedings of *International Conference on Computer Vision*, IEEE Computer Society Press, 657–661 (1987).

[81] R. J. Valkenburg, A. M. McIvor, "Accurate 3D measurement using a structured light system," *Image Vision Comput*. 16(2), 99–110 (1998).

[82] J. L. Posdamer and M. D. Altschuler, "Surface measurement by space-encoded projected beam systems," *Comput. Graph. Image Processing* 18(1), 1–17 (1982).

[83] S. Inokuchi, K. Sato, F. Matsuda, "Range-imaging for 3-D object recognition," in International *Conference on Pattern Recognition, International Association for Pattern Recognition*, , pp. 806–808 (1984).

[84] W. Krattenthaler, K. J. Mayer, H. P. Duwe, "3D-surface measurement with coded light approach," in Proceedings of *the 17th Meeting of the Austrian Association for Pattern Recognition on Image Analysis and Synthesis* (R. Oldenbourg Verlag), Vol. 12, pp. 103–114, (1993).

[85] H. Cui, W. Liao, N. Dai, X. Cheng, "A flexible phase-shifting method with absolute phase marker retrieval. *Measurement*;45:101–8 (2012).

[86] S. Zhang, S.T. Yau, "High-resolution, real-time 3-d absolute coordinate measurement based on a phase-shifting method", *Opt Express*;14(7):2644–9 (2006).

[87] G. Sansoni, M. Carocci, R. Rodella, "Three-dimensional vision based on a combination of gray-code and phase-shift light projection: analysis and compensation of the systematic errors," *Appl. Opt*. 38, 6565–6573 (1999).

[88] Q. Zhang, X. Su, L. Xiang, X. Sun, "3-d shape measurement based on complementary gray-code light," *Opt. Laser Eng*. 50, 574–579 (2012).

[89] Y. Li, H. Jin, H. Wang, "Three-dimensional shape measurement using binary spatio-temporal encoded illumination," *J. Opt. A* 11, 075502 (2009).

[90] C. Zhou, T. Liu, S. Si, J. Xu, Y. Liu, Z. Lei, "Phase coding method for absolute phase retrieval with a large number of codewords," *Opt. Express* 20, 24139–24150 (2012).

[91] C. Zhou, T. Liu, S. Si, J. Xu, Y. Liu, Z. Lei, "An improved stair phase encoding method for absolute phase retrieval," *Opt. Laser Eng*. 66, 269–278 (2015).

[92] C. Zuo, L. Huang, M. Zhang, Q. Chen, A. Asundi, "Temporal phase unwrapping algorithms for fringe projection profilometry: A comparative review", *Opt Lasers Eng*;85: 84–103 (2016).

[93] J.S. Hyun, Song Zhang, "Enhanced two-frequency phase-shifting method", *Applied Optics* Vol. 55, No. 16 (2016).

[94] C.E. Towers, D.P. Towers, J.D.C. Jones, "Absolute fringe order calculation using optimised multi-frequency selection in full-field profilometry", *Opt Lasers Eng*; 43:788–800 (2005).

[95] J.M. Huntley, H. Saldner, "Temporal phase-unwrapping algorithm for automated interferogram analysis", *Appl Opt*;32:3047–52 (1993).

[96] L. Kinell, M. Sjödahl, "Robustness of reduced temporal phase unwrapping in the measurement of shape", *Appl Opt*; 40:2297–303 (2001).

[97] X. Peng, Z. Yang, H. Niu, "Multi-resolution reconstruction of 3-dimage with modified temporal unwrapping algorithm".*Opt Commun*; 224:35–44 (2003).

[98] J. Tian, X. Peng, X. Zhao, "A generalized temporal phase unwrapping algorithm for three-dimensional profilometry", *Opt Lasers Eng*; 46:336–42 (2008).

[99] A.J. Alcock, S.A. Ramsden, "Two wavelength interferometry of a laser-induced spark in air", *Appl Phys Lett*;8 (1966).

[100] C. Polhemus, "Two-wavelength interferometry", *Appl Opt*;12:2071–4 (1973).

[101] R. Dändliker, R. Thalmann, D. Prongué, "Two-wavelength laser interferometry using super heterodyne detection", *Opt Lett*; 13:339–41(1988).

[102] J. Burke, T. Bothe, W. Osten, "Reverse engineering by fringe projection", *International Symposium on Optical Science and Technology*:312–24 (2002).

[103] J. Zhong, M. Wang, "Phase unwrapping by a lookup table method: application to phase maps with singular points", *Opt Eng*;38:2075–80 (1999).

[104] C.E. Towers, D.P. Towers, J.D. Jones, "Time efficient Chinese remainder theorem algorithm for full-field fringe phase analysis in multi-wavelength interferometry", *Opt Express*; 12:1136–43 (2004).

[105] Y.Y. Cheng, J.C. Wyant, "Two-wavelength phase shifting interferometry", *Appl Opt*; 23(24): 4539–43 (1984).

[106] H. Zhang, W. Chen, Y. Tan, "Phase-unwrapping algorithm for the measurement of three-dimensional object shapes*", Appl Opt*; 33: 4497–500 (1994).

[107] Y.Y. Cheng, J. C. Wyant, "Multiple-wavelength phase-shifting interferometry", *Appl Opt* 24(8): 804–7 (1985).

[108] L. Song, X. Dong, J. Xi , Y. Yu , C. Yang, "A new phase unwrapping algorithm based on three wavelength phase shift profilometry method", *Opt Lasers Eng*; 45: 319–29 (2013).

[109] C.E. Towers, D.P. Towers, J.D.C. Jones, "Optimum frequency selection in multifrequency interferometry", *Opt Lett*; 28(11), 887-9 (2003).

[110] F. Mohammadi, K. Madanipour, A.H. Rezaie, "Application of digital phase shift moiré to reconstruction of human face", *UKSim Fourth European Modelling Symposium on Computer Modelling and Simulation*. IEEE Computer Society;, 306–9 (2010).

[111] H. Takasaki, "Moiré Topography", *Appl* Opt; 9(6): 1467–72 (1970).

[112] J.B. Allen, D.M. Meadows, "Removal of unwanted patterns from moiré contour maps by grid translation techniques", *Appl Opt*; 10(1): 210–12 (1971).

[113] A.J. Avilaq, A.H. Rezaie, "Accuracy enhancement of 3D face reconstruction using undecimated wavelet transform. *J Am Sci*; 9 (2s): 28–34 (2013).

[114] J.J.J. Dirckx , W.F. Decraemer , M.M.K. Eyckmans, "Grating noise removal in moiré topography", *Optik*; 86: 107–10 (1990).

[115] M. Halioua, R.S. Krishnamurthy, H. Liu, F.P. Chiang, "Projection moiré with moving gratings for automated 3-D topography", *Appl Opt*; 22(6): 850–55 (1983).

[116] P.S. Huang, H. Guo, "Phase shifting shadow moiré using the Carré algorithm," in *Proc. SPIE 7066, Two- and Three-Dimensional Methods for Inspection and Metrology* VI, 70660B: 70660B1–7 (2008).

[117] J.A.N. Buytaert, J.J.J. Dirckx, "Moiré profilometry using liquid crystals for projection and demodulation", *Opt Express*; 16(1): 179–93 (2008).

[118] T. Jin-Dong, P. Xiang, Z. Xiao-Bo, "A pitch-variation moiré fringes method of temporal phase unwrapping profilometry", *Optoelectron Lett*; 3 (3): 215–8 (2007).

[119] M.S. Jeong, S.W. Kim, "Color grating projection moiré with time-integral fringe capturing for high-speed 3-D imaging", *Opt Eng*; 41(8): 1912–17 (2002).

[120] J.J.J Dirckx, W.F. Decraemer, G. Dielis, "Phase shift method based on object translation for full field automatic 3-D surface reconstruction from moiré topograms", *Appl Opt*; 27(6):1164–69 (1988).

[121] F. Mohammadi, K. Madanipour, A.H. Rezaie, "Accuracy enhancement of 3D profilometric human face reconstruction using undecimated wavelet analysis", *Appl Opt*; 51(16):3120–31(2012).

[122] B. Munch, P. Trtik, F. Marone, M. Stampanoni, "Stripe and ring artifact removal with combined wavelet-Fourier filtering", *Opt Express*; 17(10): 8567–91 (2009).

[123] R.R. Coifman, D.L. Donoho, "Translation invariant de-noising", *Springer-Verlag Wavelets and Statistics*: 125–150 (1995).

[124] I. Daubechies, "Ten Lectures on Wavelets", *CBMS-NSF Regional Conference Series in Applied Mathematics* 61 (1992).

[125] D.L. Donoho, "De-noising by soft-thresholding", *IEEE Trans Inf Theory*; 41(3): 613–627 (1995).

[126] P. Hedaoo, S.S. Godbole, "Wavelet thresholding approach for image denoising", *IJNSA*; 3(4): 16–21(2011).

[127] P. Meza, C.S. Martin, E. Vera, S. Torres, "A quantitative evaluation of fixed-pattern noise reduction methods in imaging systems", *15th Iberoamerican Congress on Pattern Recognition, CIARP, Lec. Notes Comput. Sci* 6419, 285–294 (2010).